

3-10-2010

# High Power Microwave (HPM) and Ionizing Radiation Effects on CMOS Devices

Nicholas A. Estep

Follow this and additional works at: <https://scholar.afit.edu/etd>

Part of the [Digital Circuits Commons](#), and the [Electronic Devices and Semiconductor Manufacturing Commons](#)

---

## Recommended Citation

Estep, Nicholas A., "High Power Microwave (HPM) and Ionizing Radiation Effects on CMOS Devices" (2010). *Theses and Dissertations*. 2009.  
<https://scholar.afit.edu/etd/2009>

This Thesis is brought to you for free and open access by the Student Graduate Works at AFIT Scholar. It has been accepted for inclusion in Theses and Dissertations by an authorized administrator of AFIT Scholar. For more information, please contact [richard.mansfield@afit.edu](mailto:richard.mansfield@afit.edu).



**HIGH POWER MICROWAVE (HPM) AND  
IONIZING RADIATION EFFECTS ON CMOS  
DEVICES**

THESIS

Nicholas A. Estep, 1st Lt, USAF  
AFIT/GE/ENG/10-08

**DEPARTMENT OF THE AIR FORCE  
AIR UNIVERSITY**

**AIR FORCE INSTITUTE OF TECHNOLOGY**

**Wright-Patterson Air Force Base, Ohio**

APPROVED FOR PUBLIC RELEASE; DISTRIBUTION UNLIMITED.

The views expressed in this thesis are those of the author and do not reflect the official policy or position of the United States Air Force, Department of Defense, or the United States Government.

AFIT/GE/ENG/10-08

HIGH POWER MICROWAVE (HPM) AND IONIZING RADIATION EFFECTS  
ON CMOS DEVICES

THESIS

Presented to the Faculty  
Department of Electrical Engineering  
Graduate School of Engineering and Management  
Graduate School of Engineering and Management  
Air Force Institute of Technology  
Air University  
Air Education and Training Command  
in Partial Fulfillment of the Requirements for the  
Degree of Master of Science in Electrical Engineering

Nicholas A. Estep, B.S.E.E.

1st Lt, USAF

March 2010

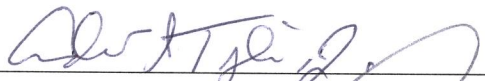
APPROVED FOR PUBLIC RELEASE; DISTRIBUTION UNLIMITED.

AFIT/GE/ENG/10-08

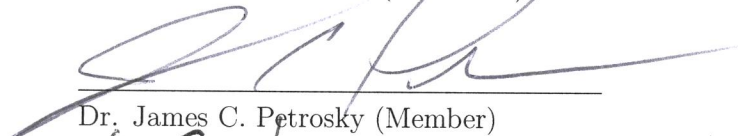
HIGH POWER MICROWAVE (HPM) AND IONIZING RADIATION EFFECTS  
ON CMOS DEVICES

Nicholas A. Estep, B.S.E.E.  
1st Lt, USAF

Approved:

  
\_\_\_\_\_  
Dr. Andrew J. Terzuoli (Chairman)

10 Mar 2010  
Date

  
\_\_\_\_\_  
Dr. James C. Petrosky (Member)

10 Mar 10  
Date

  
\_\_\_\_\_  
Dr. Yong C. Kim (Member)

11 MAR 2010  
Date

## Abstract

Integrated circuits (ICs) are inherently complicated and made worse by increasing transistor quantity and density. This trend potentially enhances concomitant effects of high energy radiation and local or impressed electromagnetic interference (EMI). The reduced margin for signal error may counter any gain in radiation hardness from smaller device dimensions. Isolated EMI and ionizing radiation studies on circuits have been conducted extensively over the past 30 years. However, little focus has been placed on the combined effects. To investigate the effect of combined EMI and ionizing radiation, two complementary metal oxide semiconductor (CMOS) inverter technologies (CD4069 and SN74AUC1G04) were analyzed for their static performance in response to EMI and up to 146 kRad(tissue) gamma radiation. The CD4069 hex inverters presented the significant vulnerability to ionizing radiation, with shifts of up to -1.9 V in voltage and current transfer characteristics (VTC and CTC). When EMI and ionizing radiation were combined, the hex inverters responded with a -1.9 V voltage shift, compounded with a 68% decrease in gain, 99% increase in maximum current, and seven orders of magnitude increase in leakage currents. The low power SN74AUC1G04 inverters are more tolerant to ionizing radiation effects due to the small inverter dimensions and gate thickness. Threshold voltages remained unchanged due to gamma irradiation, but responded with a static offset due to EMI. The threshold voltage offset due to EMI was driven by the increased asymmetric current capabilities of the NMOS and PMOS transistors. The injected EMI signals degraded the switching margins, decreasing the device gain by an average of 50%. Gamma irradiation produced at least four orders of magnitude increase in leakage currents for the low power inverters. The combined EMI and gamma radiation envi-

ronment, compared to the isolated effects, produced the most severe degradation in inverter performance for both device technologies.

## Acknowledgements

First, I would like to thank my thesis committee, Dr. James Petrosky, Dr. Andrew Terzuoli, and Dr. Yong Kim, for their guidance throughout the research. I would also like to thank Bob Kissell and Rick Moore from the 412<sup>th</sup> Electronic Warfare Group for assistance in design and manufacturing of the experimental apparatus. Tireless support from the staff at the Ohio State University Research Reactor allowed me to conduct the radiation experiments in a smooth and orderly fashion. I also want to thank the High Power Microwave division (AFRL/RDHE) for their interest and funding for this research. Additionally, Max Alexander and his team from the Nonmetallic Materials division (AFRL/RXBC) provided equipment that was crucial to the success of my research. Lastly, I would like to thank my friends and family. Without their support and constant motivation, this research would not have been possible.

Nicholas A. Estep



# Table of Contents

	Page
Abstract .....	iv
Acknowledgements .....	vi
List of Figures .....	ix
List of Tables .....	xvi
List of Symbols .....	xvii
List of Abbreviations .....	xx
I. Introduction .....	1
1.1 Problem Description .....	1
1.2 Research Objectives .....	2
1.3 Thesis Structure .....	3
II. Background .....	4
2.1 The HPM Radiation Environment .....	5
2.1.1 HPM Characteristics in Comparison to other IEMI Fields .....	6
2.1.2 HPM interaction with Electronic Systems .....	9
2.2 The Ionizing Radiation Environment .....	12
2.2.1 Radiation Dosimetry .....	12
2.2.2 Cobalt-60 Radioactive Source .....	14
2.2.3 High Energy Radiation Effects in CMOS Devices .....	16
2.2.4 Dose Rate Considerations .....	18
2.3 The CMOS Inverter .....	19
2.3.1 Static Characteristics .....	21
2.3.2 Dynamic Characteristics .....	24
2.3.3 Circuit Stability .....	25
III. Experimental Methodology .....	27
3.1 Comparison of Research to Previous Studies .....	27
3.2 Selection of the Experimental Devices .....	29
3.3 Experimental Setup .....	32
3.3.1 High Frequency Test Considerations .....	34
3.4 Experimental Procedures .....	34
3.4.1 Radiation Parameters and Signal Measurements .....	35

	Page
IV. Results .....	37
4.1 Experimental Verification .....	37
4.2 High Frequency Coupling Efficiency .....	37
4.3 Inverter Response to HPM and Ionizing Radiation .....	40
4.3.1 Radiation Effects on Device Transfer Characteristics .....	40
4.3.2 Radiation Effects on Device Parameters .....	65
V. Conclusions and Future Work .....	91
5.1 Inverter Effects Results .....	91
5.2 Inverter Effects Summary .....	92
5.3 Operational Conclusions .....	93
5.4 Future Work .....	96
A. Experimental Equipment .....	99
B. Text Fixture .....	100
C. Flow Chart for inverter control program .....	102
Bibliography .....	103

## List of Figures

Figure		Page
1.	Time and frequency domain representation for the cosine function. The cosine represents a component of an HPM pulse. $F\{ \}$ represents the fourier transform from time domain into frequency domain. ....	7
2.	Time and frequency domain representation for the impulse function. The impulse represents a component of an HPM pulse. $F\{ \}$ represents the fourier transform from time domain into frequency domain. ....	8
3.	Time and frequency domain representation of simulated HPM signal components. ....	9
4.	Time and frequency domain representation of simulated UWB signal components. ....	9
5.	IEMI disturbances for electronic systems. HPM and UWB threats pose the greatest potential for upset of electronic systems as frequency enters the microwave spectrum [32]. ....	10
6.	Illustration of charged particle equilibrium (CPE). Once a material thickness is greater than the CPE requirement, accurate comparisons in dosimetry can be made [19]. ....	13
7.	Decay scheme for $^{60}\text{Co}$ . Two gamma rays, of energies 1.17 MeV and 1.33 MeV, are produced. ....	15
8.	Schematic of two transistors, an NMOS and PMOS, connected to function as a single CMOS inverter. ....	19
9.	Cross section of a CMOS inverter. ....	20
10.	Cross section of a CMOS inverter illustrating new IC processing techniques. ....	20
11.	Ideal CMOS transfer characteristics [34]. ....	23
12.	Terminal assignments for the AUC1G04 and CD4069UB CMOS inverter devices. Schematic layout and symbolic representation of an inverter [1], [2]. ....	31

Figure	Page
13. Experimental setup.....	32
14. Device under test (DUT) design. Impedance matching techniques and striplines allowed for efficient high frequency coupling. ....	34
15. Vector network analyzer (VNA) measurements for A and B Inverters illustrating the resonant frequencies. ....	38
16. Spectrum analyzer results for a B inverter. ....	39
17. VTC effects for ionizing only low input state condition on an A inverter. The dose rate was 73 krad(tissue)/hr and was irradiated for a total dose of 109 krad(tissue).....	41
18. VTC effects for ionizing only high input state condition on an A inverter. The dose rate was 73 krad(tissue)/hr and was irradiated for a total dose of 109 krad(tissue).....	42
19. VTC effects for ionizing only irradiation on an A inverter. Both the low and high input state condition effects are shown for a dose rate of 73 krad(tissue)/hr and total dose of 109 krad(tissue). ....	43
20. VTC response due to various HPM signals on an A inverter. All HPM CW signals had 26 dBm power. ....	44
21. VTC effects for combined HPM and ionizing high input state condition on an A inverter. The dose rate was 73 krad(tissue)/hr and was irradiated for a total dose of 109 krad(tissue). A 500 kHz 26 dBm signal was injected into the inverter during each measurement.....	46
22. VTC response for all A inverter experiments during 15 minutes of irradiation. 73 krad(tissue)/hr and 36 krad(tissue)/hr (labeled as half dose rate) were selected. For the HPM and combined experiments, a 500 kHz 26 dBm was injected into the device. ....	47

Figure	Page
23.	VTC response for all A inverter experiments during 90 minutes of irradiation. 73 krad(tissue)/hr and 36 krad(tissue)/hr (labeled as half dose rate) were selected. For the HPM and combined experiments, a 500 kHz 26 dBm was injected into the device. . . . . 47
24.	VTC response for all A inverter experiments after 90 minutes of annealing. 73 krad(tissue)/hr and 36 krad(tissue)/hr (labeled as half dose rate) were selected. For the HPM and combined experiments, a 500 kHz 26 dBm was injected into the device. . . . . 48
25.	VTC response due to various HPM signals on a B inverter. All HPM CW signals had 26 dBm power. . . . . 49
26.	VTC effects for combined HPM and ionizing high input state condition on a B inverter. The dose rate was 73 krad(tissue)/hr and was irradiated for a total dose of 146 krad(tissue). A 1 GHz 26 dBm signal was injected into the inverter during each measurement. . . . . 51
27.	CTC effects for ionizing only low input state condition on an A inverter. The dose rate was 73 krad(tissue)/hr and was irradiated for a total dose of 109 krad(tissue). . . . . 52
28.	Leakage current effects for ionizing only low input state condition on an A inverter. The dose rate was 73 krad(tissue)/hr and was irradiated for a total dose of 109 krad(tissue). . . . . 53
29.	CTC effects for ionizing only high input state condition on an A inverter. The dose rate was 73 krad(tissue)/hr and was irradiated for a total dose of 109 krad(tissue). . . . . 54
30.	CTC effects for ionizing only irradiation on an A inverter. Both the low and high input state condition effects are shown for a dose rate of 73 krad(tissue)/hr and total dose of 109 krad(tissue). . . . . 55
31.	CTC response due to various HPM signals on an A inverter. All HPM CW signals had 26 dBm power. . . . . 56
32.	Leakage current response due to various HPM signals on an A inverter. All HPM CW signals had 26 dBm power. . . . . 57

Figure	Page
33.	CTC effects for combined HPM and ionizing high input state condition on an A inverter. The dose rate was 73 krad(tissue)/hr and was irradiated for a total dose of 109 krad(tissue). A 500 kHz 26 dBm signal was injected into the inverter during each measurement. . . . . 58
34.	CTC response for all A inverter experiments during 15 minutes of irradiation. 73 krad(tissue)/hr and 36 krad(tissue)/hr (labeled as half dose rate) dose rates were selected. For the HPM and combined experiments, a 500 kHz 26 dBm was injected into the device. . . . . 59
35.	CTC response for all A inverter experiments during 90 minutes of irradiation. 73 krad(tissue)/hr and 36 krad(tissue)/hr (labeled as half dose rate) dose rates were selected. For the HPM and combined experiments, a 500 kHz 26 dBm was injected into the device. . . . . 59
36.	CTC response for all A inverter experiments after 90 minutes of annealing. 73 krad(tissue)/hr and 36 krad(tissue)/hr (labeled as half dose rate) dose rates were selected. For the HPM and combined experiments, a 500 kHz 26 dBm was injected into the device. . . . . 60
37.	Leakage current effects for ionizing only low input state condition on a B inverter. The dose rate was 73 krad(tissue)/hr and was irradiated for a total dose of 146 krad(tissue). . . . . 61
38.	CTC response due to various HPM signals on a B inverter. All HPM CW signals had 26 dBm power. . . . . 62
39.	Leakage current response due to various HPM signals on a B inverter. All HPM CW signals had 26 dBm power. . . . . 64
40.	CTC effects for combined HPM and ionizing high input state condition on a B inverter. The dose rate was 73 krad(tissue)/hr and was irradiated for a total dose of 146 krad(tissue). A 1 GHz 26 dBm signal was injected into the inverter during each measurement. . . . . 64

Figure	Page
41. Leakage current effects for combined HPM and ionizing high input state condition on a B inverter. The dose rate was 73 krad(tissue)/hr and was irradiated for a total dose of 146 krad(tissue). A 1 GHz 26 dBm signal was injected into the inverter during each measurement. ....	65
42. PMOS threshold voltage response for all A inverter experiments. 73 krad(tissue)/hr and 36 krad(tissue)/hr (labeled as half dose rate) dose rates were selected. For the HPM and combined experiments, a 500 kHz 26 dBm was injected into the device. ....	67
43. NMOS threshold voltage response for all A inverter experiments. 73 krad(tissue)/hr and 36 krad(tissue)/hr (labeled as half dose rate) dose rates were selected. For the HPM and combined experiments, a 500 kHz 26 dBm was injected into the device. ....	67
44. Observed shift in $V_{Tp}$ and $V_{Tn}$ conducted by Brucker et al. using a sample of 17 CD4069 hex inverters obtained from a single wafer. Inverter sets, indicated in parentheses, are exposed to different doses, in rad $\text{SiO}_2$ . Arrows indicate end of irradiation and start of annealing [9]. ....	68
45. Switch point voltage response for all A inverter experiments. 73 krad(tissue)/hr and 36 krad(tissue)/hr (labeled as half dose rate) dose rates were selected. For the HPM and combined experiments, a 500 kHz 26 dBm was injected into the device. ....	72
46. Maximum current peak ( $I_{max}$ ) response for all A inverter experiments. 73 krad(tissue)/hr and 36 krad(tissue)/hr (labeled as half dose rate) dose rates were selected. For the HPM and combined experiments, a 500 kHz 26 dBm was injected into the device. ....	75
47. Threshold voltage gap ( $V_{gap}$ ) response for all A inverter experiments. 73 krad(tissue)/hr and 36 krad(tissue)/hr (labeled as half dose rate) dose rates were selected. For the HPM and combined experiments, a 500 kHz 26 dBm was injected into the device. ....	77

Figure	Page
48. PMOS leakage current response for all A inverter experiments. 73 krad(tissue)/hr and 36 krad(tissue)/hr (labeled as half dose rate) dose rates were selected. For the HPM and combined experiments, a 500 kHz 26 dBm was injected into the device. ....	80
49. NMOS leakage current response for all A inverter experiments. 73 krad(tissue)/hr and 36 krad(tissue)/hr (labeled as half dose rate) dose rates were selected. For the HPM and combined experiments, a 500 kHz 26 dBm was injected into the device. ....	82
50. PMOS leakage current response for all B inverter experiments. A 73 krad(tissue)/hr dose rate was selected for a total dose of 146 krad(tissue). For the HPM and combined experiments, a 1 GHz 26 dBm was injected into the device. ....	84
51. NMOS leakage current response for all B inverter experiments. A 73 krad(tissue)/hr dose rate was selected for a total dose of 146 krad(tissue). For the HPM and combined experiments, a 1 GHz 26 dBm was injected into the device. ....	85
52. Device gain response for all A inverter experiments. 73 krad(tissue)/hr and 36 krad(tissue)/hr (labeled as half dose rate) dose rates were selected. For the HPM and combined experiments, a 500 kHz 26 dBm was injected into the device. ....	88
53. Cross Section of a CMOS Inverter illustrating a single Si substrate. A n well is generated to create the n-type channel for the PMOS transistor [18]. ....	95
54. NAND and NOR logic structures. Both types of logic gate use CMOS technology to construct all levels of digital logic. ....	96



Figure	Page
55.	AutoCAD drawing of the B Inverter DUT, which is mounted on the test fixture. U1 represents the pad location for the advanced low power single gate inverters. The hex inverter, a DIP design, is located on the test fixture itself. The test fixture includes the flexibility to include load matching components and output load resistors. . . . . 100
56.	Drawing of DUT including isolated pad layout. Design is incorporated from the schematic in Figure 14. . . . . 101

## List of Tables

Table		Page
1.	Types of radiation considered in the research and their primary effect on a material . . . . .	5
2.	HPM signal components in time and frequency domain . . . . .	8
3.	Types of radiation and their primary effect on a material. . . . .	12
4.	Dose conversion parameters for photon energies around 1.2 MeV. . . . .	16
5.	Inverter truth table . . . . .	21
6.	Common HPM field characteristics in previous research . . . . .	28
7.	Controlled experimental parameters and analyzed inverter parameters. . . . .	35
8.	Comparison of normal operation and HPM effects for VTC on an A Inverter. Corresponding voltages relate to device gain. . . . .	45
9.	Comparison of normal operation and HPM effects for VTC on a B Inverter. Corresponding voltages relate to device gain. . . . .	50
10.	Comparison of normal operation and HPM effects for CTC on an A Inverter. . . . .	57
11.	Comparison of normal operation and HPM effects for CTC on an B Inverter. . . . .	63
12.	Effects metrics for inverter parameters. . . . .	91
13.	Most excessive effects on CMOS devices. HI is high input, LI is low input, and values are the most extreme during that particular experiment. An asterisk means the value is at least that large, but outside the bounds of the instruments. . . . .	92
14.	Most excessive effects on CMOS devices . . . . .	93

## List of Symbols

Symbol	Page
$E$	energy of radiation ..... 4
$\nu$	frequency of electromagnetic radiation ..... 4
$h$	Plank's constant ..... 4
$ns$	nanosecond ..... 6
$\mu s$	microsecond ..... 6
$x(t)$	time domain function ..... 6
$X(w)$	frequency domain function ..... 6
$\omega$	angular frequency ..... 7
$f$	frequency of HPM radiation ..... 7
GHz	gigahertz ..... 11
$E_D$	energy deposited ..... 13
$\Delta E_E(\gamma)$	gamma energy entering the material region ..... 13
$\Delta E_L(\gamma)$	gamma energy leaving the material region ..... 13
$D_{eq}$	absorbed dose in equilibrium ..... 13
$m$	mass ..... 14
$\frac{\mu_{en}}{\rho}$	mass energy absorption coefficient ..... 14
$\rho$	density of a material ..... 14
$\Delta x$	thickness of a material ..... 14
$mm$	millimeter ..... 15
$N(x)$	percentage of surviving gamma rays for a given material thickness ..... 15
$N_0$	initial percentage of gamma rays ..... 15

Symbol	Page
$\text{SiO}_2$	Silicon Dioxide ..... 15
$T_{\max}$	maximum kinetic energy transfer from gamma ray to electron ..... 15
eV	electron volt energy ..... 16
Si	Silicon ..... 16
$\mu_n$	mobility of an electron ..... 17
$\mu_p$	mobility of a hole ..... 17
$N_{it}$	interface traps ..... 17
$N_{ot}$	oxide traps ..... 17
$V_{DD}$	power supply voltage ..... 19
$V_{in}$	input voltage ..... 21
$V_{Tn}$	NMOS threshold voltage ..... 21
$V_{Tp}$	PMOS threshold voltage ..... 21
$r$	transistor resistance ..... 21
$k'_p$	PMOS transconductance ..... 21
$(W/L)_p$	PMOS transistor device ratio ..... 21
$V_{out}$	output voltage ..... 21
$i_{DP}$	PMOS conduction current ..... 22
$i_{DN}$	NMOS conduction current ..... 22
$V_T$	threshold voltage ..... 24
$C$	capacitance ..... 24
$t_r$	inverter rise time ..... 24
$t_f$	inverter fall time ..... 24

Symbol	Page
$V_{IH}$	minimum input voltage for proper high voltage output . . . . . 25
$V_{IL}$	maximum input voltage for proper low voltage output . . . . . 25
$NM_H$	noise margin for high input . . . . . 25
$NM_L$	noise margin for low input . . . . . 25
$V_{sp}$	inverter switch point voltage . . . . . 26
$Z_C$	impedance of a capacitor . . . . . 33
$Z_L$	impedance of an inductor . . . . . 33
$C$	capacitance . . . . . 33
$L$	inductance . . . . . 33
dB	decibels . . . . . 38
kHz	kilohertz . . . . . 38
MHz	megahertz . . . . . 38
$V_{OH}$	output voltage corresponding to $V_{IH}$ . . . . . 45
$V_{OL}$	output voltage corresponding to $V_{IL}$ . . . . . 45
1 mW	milliwatt . . . . . 49
$t_{ox}$	MOSFET oxide thickness . . . . . 70
$V_{gap}$	voltage region separating the NMOS and PMOS threshold voltages . . . . . 77
$I_{leak}$	transistor leakage current . . . . . 79

## List of Abbreviations

Abbreviation		Page
ICs	integrated circuits . . . . .	1
IEMI	intentional electromagnetic interference . . . . .	1
CMOS	complementary metal oxide semiconductor . . . . .	2
NMOS	n-channel metal oxide semiconductor field effect transistor . . . . .	2
COTS	commercial off the shelf . . . . .	2
EMI	electromagnetic interference . . . . .	5
HPM	high power microwave . . . . .	6
UWB	ultra wideband . . . . .	6
EMP	electromagnetic pulse . . . . .	6
EMC	electromagnetic compatibility . . . . .	11
IEC	International Electrotechnical Commission . . . . .	11
CPE	charged particle equilibrium . . . . .	13
MAC	mass energy absorption coefficient . . . . .	14
Co	Cobalt . . . . .	14
OSURR	Ohio State University Research Reactor . . . . .	14
Ni	Nickel . . . . .	14
EHP	electron hole pairs . . . . .	15
MOSFETs	metal oxide semiconductor field effect transistors . . . . .	16
PMOS	p-channel metal oxide semiconductor field effect transistor . . . . .	16
CTRW	continuous time random walk . . . . .	17
ELDRS	enhanced low dose rate sensitivity . . . . .	18

Abbreviation	Page
BJT	bipolar junction transistor ..... 18
TREE	transient radiation effects in electronics ..... 19
STI	shallow trench isolation ..... 20
VTC	voltage transfer characteristic ..... 24
CTC	current transfer characteristic ..... 24
DUT	device under test ..... 27
PRF	pulse repetition frequency ..... 28
TID	total ionizing dose ..... 28
MESFET	metal semiconductor field effect transistor ..... 29
TTL	transistor transistor logic ..... 29
VNA	vector network analyzer ..... 32
CW	continuous wave ..... 32
SMA	SubMiniature version A ..... 32
DC	direct current ..... 33
AC	alternating current ..... 33
LPF	low pass filter ..... 33
HPF	high pass filter ..... 33
VSWR	voltage standing wave ratio ..... 33
LI	low input ..... 40
HI	high input ..... 41
RDM	radiation design margins ..... 91
JPL	Jet Propulsion Laboratory ..... 91

# HIGH POWER MICROWAVE (HPM) AND IONIZING RADIATION EFFECTS ON CMOS DEVICES

## I. Introduction

### 1.1 Problem Description

Today's digital devices are not only advanced in performance, but their availability and low cost has driven the advanced world to depend on their functionality in most daily activities. To keep pace with the growing digital need, the dimensions of transistors are continuously scaled down. Semiconductor manufacturers continue to pack more transistors onto integrated circuits (ICs) while driving them faster in order to meet the performance demands of a technological savvy society. With each advancement, hidden vulnerabilities, whether intentional or unintentional, enhance the risk of device failure. Due to device scaling and their related noise margins, advanced electronics display vulnerabilities to electromagnetic interference far greater than previous generations.

Similarly, consideration for devices operating in the high energy radiation environment must be addressed. Whether device operation is intended for space or nuclear applications, one must inspect the effects of high energy radiation. Some research may suggest obsolete technology may present greater vulnerability to such radiation, but such a conclusion may prove premature. As with intentional electromagnetic interference (IEMI), the reduced room for signal error may overcome the natural high energy radiation hardness from smaller devices. Studies of advanced transistors or devices must verify the trend of high energy radiation hardness.



In order to study radiation effects in current technology, one must identify the prevalent technology found in ICs. Since the late 1970's, complementary metal oxide semiconductor (CMOS) technology asserted its dominance in the design of conventional digital devices [34]. The two compelling design advantages that enabled CMOS logic to surpass its predecessor, n-channel metal oxide semiconductor field effect transistor (NMOS) architecture, include transistor scaling efficiency and low static and dynamic power consumption.

With the current and future technology market focused on transistor density and power conservation, the CMOS design structure will continue to gain prevalence in electronic devices. For the reasons listed previously, commercial off the shelf (COTS) electronics are comprised mostly of CMOS technology in commercial and military applications. Full comprehension of any complex and detailed CMOS IC requires the understanding of its fundamental building block, the CMOS inverter. Accordingly, analyzing CMOS inverter device performance in both low and high energy radiation conditions is paramount to their successful deployment in any environment.

## **1.2 Research Objectives**

The main objective of the research was to establish a robust methodology to test and evaluate the effects of each radiation environment on digital devices. The CMOS inverter provides the foundation for all complex circuits. Yet, the well understood functionality of the inverter supplies an ideal device to verify the experimental methodology. Then, the developed radiation experimental methodology, validated with the inverter, may be expanded to investigate the effects on other digital devices.

Complementing the establishment of the methodology, the research aimed to identify and quantify the particular effects of each radiation environment for the selected test inverters. The results may lead to not only an established test methodology, but

a better understanding of the interaction of radiation with CMOS devices. Greater insight into each radiation environment may assist in establishing requirements to prevent device malfunction or failure.

Lastly, the research sought to determine the compound effect of the simultaneous interaction of each type of radiation with CMOS devices. Previous studies included the effects of IEMI and high energy radiation independently, but not with both interactions at the same time. The compound effect may amplify the vulnerability of a CMOS device, or counterbalance and mitigate the total radiation response. Including the two radiation environments simultaneously will help identify the need, or verify unnecessary potential testing, for further compound radiation research on digital devices.

### **1.3 Thesis Structure**

This thesis begins with background development of fundamental topics necessary to the research. Theory of IEMI, high energy radiation, and the CMOS inverter will be presented in Chapter 2. Chapter 3 includes the methodology to which the research was conducted. The research results for the thesis will be covered in Chapter 4. Chapter 5 recounts a concluding summary of the research and future considerations in radiation effects experimentation. During the course of this thesis, radiation refers to gamma electromagnetic energy and HPM refers to the intentional use of narrow band microwave electromagnetic energy as a means to disrupt or degrade electronic systems.

## II. Background

The interaction of electromagnetic radiation with matter depends on the material and the respective region of the electromagnetic spectrum. Max Plank introduced a uniform equation relating a quantum of radiation energy, a photon, as [23]

$$E = h\nu, \tag{1}$$

which states the energy of the radiation,  $E$ , of frequency,  $\nu$ , exists in multiples of  $h\nu$ , where  $h$  is Plank's constant. From Equation 1, lower frequency radiation, such as radio waves, contain very small quantum energy. At low energies, radiation is mostly transparent to materials. As the frequency increases into the microwave region, matter begins to absorb more radiation due to the increased quantum energy. Within the microwave spectrum, the quantum energy results in rotation and torsion of molecules within the material. Such reshaping of the material results in the production of heat. Metals, with their loosely bound outer electrons, prove the exception to the rule. Instead, they strongly absorb the quantum energies, e.g. microwaves, inducing electrical currents within the material.

As the electromagnetic energy continues into the X-ray and gamma spectrum, quantum energies are sufficiently greater than absorption energies, increasing radiation ionization of the material. Unlike the interaction in the microwave spectrum, the high energy electromagnetic radiation interacts with a material through photoelectric absorption, compton scattering, and pair production. With the exception of pair production, these interactions produce a free electron which classifies X-ray and gamma radiation as ionizing radiation [22]. Table 1 illustrates the two types of radiation considered in the research and their primary interaction with matter. It is clear that microwave radiation, the electromagnetic region of interest in IEMI, induces unwanted

currents on conductors. In contrast, high energy radiation primarily produces ions, thus increasing charged carriers, in a material. These two radiation environments may instigate unique effects in electronics and will be discussed throughout the research.

**Table 1. Types of radiation considered in the research and their primary effect on a material**

Radiation spectrum	Frequency range	Quantum energy	Primary interaction with matter
Microwave	$10^9 - 10^{10} Hz$	$10^{-5} - 10^{-3} eV$	Rotation and torsion of molecules (heating) Induced currents on conductors
Gamma	$10^{17} - 10^{19} Hz$	$0.5 \times 10^5 - 3 \times 10^6 eV$	Ionizing of atoms

## 2.1 The HPM Radiation Environment

Electromagnetic energy in the microwave range induces currents on conducting material, leading to IEMI vulnerabilities. The objective of IEMI is to utilize such induced currents to distort the intended signal within the electronic system. A widely accepted definition declares IEMI as an [31],

Intentional malicious generation of EM energy introducing noise or signals into electric and electronic systems, thus disrupting, confusing or damaging these systems for terrorist or criminal purposes.

The use of IEMI by criminals, disgruntled employees, or terrorists has dramatically increased in the past decade, causing concern worldwide [32]. Transportation, telecommunications, and power systems has all displayed susceptibility to IEMI upset. Alternatively, unintentional spurious emissions from external electronics may cause electromagnetic interference (EMI). Modern technologies have densely packed circuit boards, which increase the spurious external emissions that interact with a device. Compounding the EMI problem, growth in wireless transmission in the radio and microwave electromagnetic spectrum magnifies EMI vulnerabilities.

Since the research focused on the high power microwave (HPM) environment, a subset of IEMI, further definition of the signal characteristics is required.

### 2.1.1 HPM Characteristics in Comparison to other IEMI Fields.

Common IEMI subsets depend on the environment of operation and include:

- high power microwave (HPM)
- ultra wideband (UWB)
- electromagnetic pulse (EMP)

The HPM class describes transient electromagnetic environments with intense peak electric and magnetic fields. Unlike the UWB and EMP environments, HPM consists of a concise pulse while focusing a majority of the field energy on a specific frequency of interest. The narrow pulse of a HPM, usually a bandwidth of less than 1% of the center frequency, radiates power for a fixed time. Some HPM pulse lengths range from 100 *ns* to 100  $\mu$ s and may produce a single or repeated signal [31].

In order to comprehend the unique characteristics of an HPM signal, both time and frequency domain analysis is necessary. Since the signals in the IEMI environment consist mostly of semi-periodic sinusoids, repeated signals that do not last indefinitely, Fourier analysis is traditionally applied. The Fourier Transforms for functions in the time domain,  $x(t)$ , and frequency domain,  $X(\omega)$ , are defined as [29]

$$x(t) = \frac{1}{2\pi} \int_{-\infty}^{\infty} X(\omega) e^{j\omega t} d\omega, \quad (2)$$

$$X(\omega) = \int_{-\infty}^{\infty} x(t) e^{-j\omega t} dt, \quad (3)$$

and

$$\omega = 2\pi f, \quad (4)$$

where  $\omega$  is the angular frequency,  $f$  is the frequency, and  $t$  is the time. The short, sinusoidal HPM pulse incorporates a variety of mathematical functions, to include sinusoids and impulse, or  $rect(t)$ , functions. A fourier transform of these functions reveals  $sinc(f)$  and  $delta$  ( $\delta(f)$ ) frequency dependent functions. Figures 1 and 2 provide a comparison for the time and frequency response for pulse and sinusoid functions, which simulate components of an HPM signal.

In contrast, exponentials and gaussian pulse functions generally represent UWB signals. As seen in Figure 4(b), these functions appear as flat plateaus in the frequency domain, with energy spread throughout a large frequency range. Table 2 contains the related mathematical functions in time and frequency domain for functions inherent to HPM and UWB signals [29].

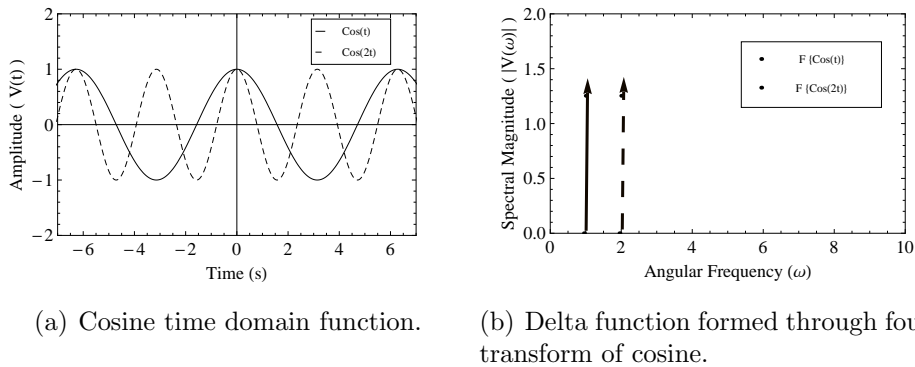
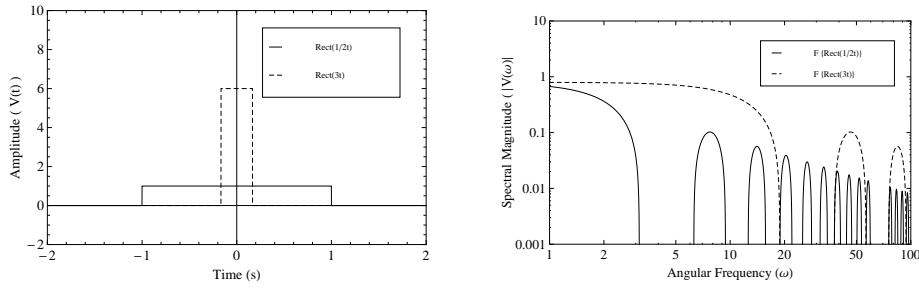


**Figure 1. Time and frequency domain representation for the cosine function. The cosine represents a component of an HPM pulse.  $F\{ \}$  represents the fourier transform from time domain into frequency domain.**

From Equation 2, one can determine how the common time domain parameters; amplitude, pulse length, and frequency, effect the frequency domain representation. The signal attributes in the above examples contribute to the following trends:

- Larger amplitude in time domain  $\implies$  Larger magnitude in frequency domain
- Shorter pulse in time domain  $\implies$  Wider spread of frequencies
- Faster oscillations in time domain  $\implies$  Shift to a higher frequency



(a) Impulse time domain function.

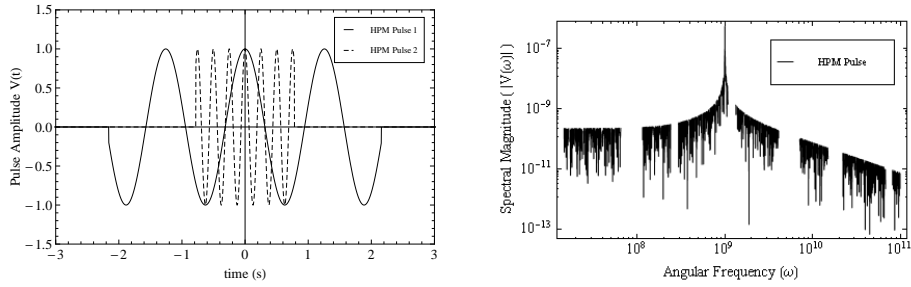
(b) Sinc function formed from fourier transform of impulse function.

**Figure 2. Time and frequency domain representation for the inpulse function. The impulse represents a component of an HPM pulse.  $F\{ \}$  represents the fourier transform from time domain into frequency domain.**

**Table 2. HPM signal components in time and frequency domain**

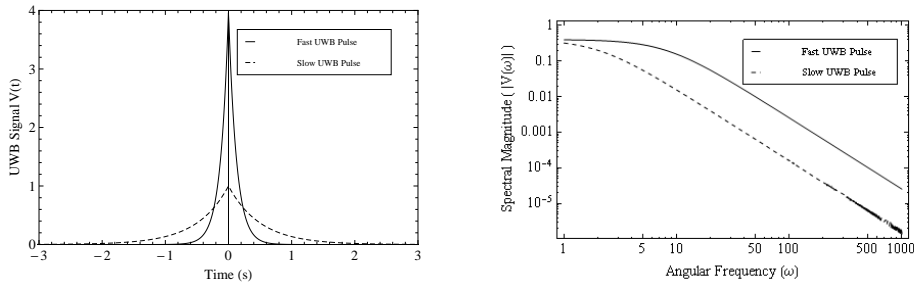
HPM Related Functions	
Time Domain $[x(t)]$	Frequency Domain $[X(f)]$
$rect(t)$	$sinc(f)$
$\cos(2\pi f_0 t)$	$\frac{1}{2}\delta(f - f_0) + \frac{1}{2}\delta(f + f_0)$
UWB Related Functions	
Time Domain $[x(t)]$	Frequency Domain $[X(f)]$
$e^{-\alpha t }$	$\frac{2\alpha}{\alpha^2 + (2\pi f)^2}$

The HPM and UWB pulses may be simulated as a combination of the functions listed in Table 2. The HPM signal, characterized by a sinusoid limited by the pulse function, now contains a distinct time interval. The UWB signal may be simply modeled as a quickly decaying exponential. Figures 3 and 4 compare the HPM and UWB time and frequency domain responses. Here, the 1 GHz signal with a 0.5 second pulse generated a strong frequency response centered at 1 GHz. These unique characteristics lead to transient non linear effects which are outside the realm of other IEMI interferences. The HPM signals focus the energy at a specific frequency whereas an UWB pulse covers a wide spectral response.



(a) Pulsed cosine wave in time domain. (b) Pulsed cosine wave converted into frequency spectrum by fourier transform.

**Figure 3. Time and frequency domain representation of simulated HPM signal components.**



(a) Exponential pulse in time domain (b) Exponential pulse converted into frequency spectrum by fourier transform.

**Figure 4. Time and frequency domain representation of simulated UWB signal components.**

### 2.1.2 HPM interaction with Electronic Systems.

The intense HPM fields focused at precise frequencies, as indicated in Figure 5, increase the potential upset in an electronic system [32]. Delivery of the HPM electromagnetic energy includes free space radiation and conduction environments. In the conduction domain, the HPM energy requires direct injection of the signal into wires, cables, or any conductor. Direct conduction of the HPM signal may be more efficient than coupled radiation fields, but potential IEMI exploitations are limited to direct physical interaction with the structure.

On the other hand, radiated electromagnetic energy expands the realm of possible entry points for IEMI. The radiated environments may be separated by their coupling



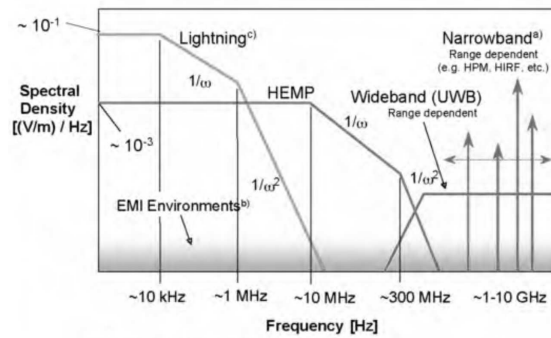


**Figure 5. IEMI disturbances for electronic systems. HPM and UWB threats pose the greatest potential for upset of electronic systems as frequency enters the microwave spectrum [32].**

methods, to include:

1. Front door: An intended coupling path for electromagnetic energy
2. Back door: An unintended coupling path for electromagnetic energy

Cables and antenna structures are front door coupling paths which provide an efficient coupling method for frequencies close to the intended use. Unintended entry points, or back door coupling, increase the vulnerability of an electronic system to IEMI. Apertures, such as windows or improperly shielded enclosures, allow HPM electromagnetic energy to couple into the system. Similarly, poorly or unshielded cables provide a means for radiated fields to couple into conductors. The efficiency of coupling into an aperture or conductor depends on numerous factors, including but not limited to, the incident field and target characteristics, as listed below.

- Angle of incident field
- Polarization of incident field
- Electric field amplitude
- Frequency of radiated fields

- Waveform of field  $[x(t)$  or  $X(f)]$

Previous studies provide strong evidence suggesting 0.5 - 5 GHz interference frequencies result in the most susceptibility for electronic systems [20], [21], [13], [15], [3], [17], [28], [25], [24]. Baum's Law states that frequencies corresponding to the physical dimensions of common electronic objects produce high resonance, thus enabling high coupling efficiency within the frequency range [6]. Microwave wavelengths, in particular 0.5 m to 30 mm, are similar in size to common electronics. When the applied HPM frequency is close to the device resonant frequency, efficient power transfer leads to greater electronic susceptibility. The undesired fields induce instability in devices, leading to increased current leakage, distorted signals, decreased noise margins, and possible state change. In the end, complex electronic systems require more analysis than just the applied frequency.

Currently, electromagnetic compatibility (EMC) standards are required for nearly all COTS electronic devices, found in the IEC 61000 series. Standardized qualification experiments include emission experiments to observe the fields radiated from the system and impressed IEMI to observe possible capability degradation. The thresholds for HPM interference on electrical enclosures, as dictated by EMC standard International Electrotechnical Commission (IEC) 61000-2-13.

The immunity levels indicated in 61000-2-13 are for the enclosure port, which is a physical boundary of the apparatus which electromagnetic fields may radiate through or impinge on [30]. Therefore, EMC standards do not include back door coupling into unintended apertures, such as signal or power ports. When performing EMC immunity experiments, it is unusual to apply a narrowband radiated field, such as an HPM signal, at sufficient field amplitudes for frequencies above 80 MHz [31].

Previous research has identified susceptibility of commercial electronics to HPM threats, even with EMC certification [27],[28]. It is clear that HPM IEMI requires

additional EMC standards, which begin with HPM susceptibility experiments.

## 2.2 The Ionizing Radiation Environment

High energy electromagnetic radiation primarily produces ionization due to the energy imparted on the electrons orbiting the nucleus. Alternatively, heavy ion particles, neutrons, and some extremely energetic gamma rays produce atomic displacement. Table 3 presents common high energy radiation and particles and their primary effect on materials.

**Table 3. Types of radiation and their primary effect on a material**

Radiation	Primary Effect
Gamma	Ionization
X-rays	Ionization
Neutrons	Displacement Damage
High Energy Electrons	Displacement Damage

The energy deposited depends on the type of material, energy and type of radiation, and the physical dimensions of the material.

### 2.2.1 Radiation Dosimetry.

When comparing ionizing radiation effects between different materials, one must consider the process of energy deposition in a material, or dosimetry. An equivalent radiation source may produce an equivalent fluence ( $\frac{1}{\text{cm}^2}$ ), but the material response, determines the end effect. Dosimetry, the deciphering of the absorbed dose in a material, includes tracking human tissue exposure to harmful radiation and estimating dose absorption in electronics. Accurate dosimetry involves a two step process: [19]

1. Measurement of dose deposited in a reference material in a measurement device

(dosimeter).

2. Deduction of dose in the material when compared to reference material dose.

Proper dosimetry for ionizing radiation must consider the concept of charged particle equilibrium (CPE). CPE identifies the amount of material necessary so that the total energy exiting the mass by electrons equals the total energy entering the mass by electrons. Since photons do not transfer their energy directly to a material, but rather to electrons, the CPE condition must be met in both the material and dosimeter for accurate dosimetry. Fig. 6 presents an example of the CPE condition in a material. With the CPE condition met, the deposited energy is due to the ionizing radiation as shown by [19]

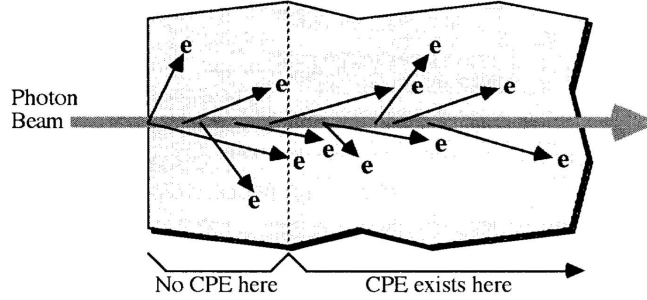


**Figure 6.** Illustration of charged particle equilibrium (CPE). Once a material thickness is greater than the CPE requirement, accurate comparisons in dosimetry can be made [19].

$$\Delta E_D = \Delta E_E(\gamma) - \Delta E_L(\gamma), \quad (5)$$

where  $E_D$  is the deposited energy,  $\Delta E_E(\gamma)$  is the gamma energy entering the material region, and  $\Delta E_L(\gamma)$  is the gamma energy leaving the material region. Under the CPE condition, the equilibrium absorbed dose,  $D_{eq}$ , a relation of the transfer of energy from the ionizing radiation to a material, is found by [19]

$$D_{eq} = \frac{\Delta E_D}{\Delta m} = \frac{\Delta E_E(\gamma) - \Delta E_L(\gamma)}{\Delta m}, \quad (6)$$

where  $m$  is the mass element of interest.

The gamma energies leaving and entering a material region are related by [19]

$$\Delta E_L(\gamma) = \Delta E_E(\gamma)e^{-\left(\frac{\mu_{en}}{\rho}\right)\rho\Delta x}, \quad (7)$$

where  $\frac{\mu_{en}}{\rho}$  is the mass energy absorption coefficient (MAC) of the material,  $\rho$  is the density of the material, and  $\Delta x$  is the thickness. Two doses for different materials are then related by a ratio of their MACs, as shown in Equation 8.

$$\frac{D_{eq}(1)}{D_{eq}(2)} = \frac{(\mu_{en}/\rho)(1)}{(\mu_{en}/\rho)(2)} \quad (8)$$

Equation 8, only valid if both materials are measured in CPE, states that if one takes measurements in a reference material (2), then one may calculate the dose of the material of interest (1) in the same radiation field.

### 2.2.2 Cobalt-60 Radioactive Source.

Gamma irradiation was conducted with the 1212 Ci Cobalt-60 ( $^{60}\text{Co}$ ) source at The Ohio State University Research Reactor (OSURR). The gamma irradiation source, with a maximum dose rate of 73 krad(tissue)/hr, permitted in situ measurements of the device during irradiation, as well as the concurrent injection of the HPM signal.

The  $^{60}\text{Co}$  decay scheme, shown in Figure 7, illustrates the resulting gamma energy peaks of 1.17 MeV and 1.33 MeV.  $^{60}\text{Co}$  initially beta decays into an unstable  $^{60}\text{Ni}$ . The unstable Ni isotope then stabilizes by emitting two gamma rays, 1.17 MeV and 1.33 MeV, as shown in Equation 9.





At these energies, the gammas interact with electronic material primarily via compton scattering, resulting in the creation of electron-hole-pairs (EHP). Conversely, some non-ionizing events may be generated by the two  ${}^{60}\text{Co}$  gammas. Some electrons released by the gamma irradiation may displace an atom in a semiconductor material from its lattice site, given sufficient energy.

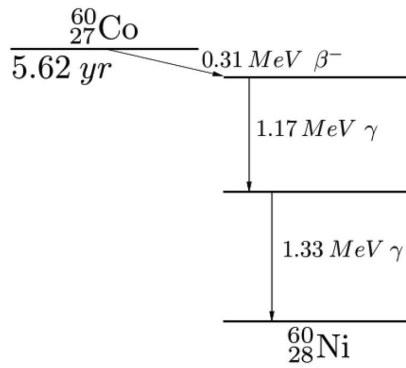


**Figure 7. Decay scheme for  ${}^{60}\text{Co}$ . Two gamma rays, of energies 1.17 MeV and 1.33 MeV, are produced.**

A calculation was performed to determine the degree to which ionization and displacement played a role in the radiation interaction with the inverters. Since the inverters contain a maximum thickness of 1 *mm* ceramic shielding, the percentage of gammas that interact with the inverter,  $N(x)$ , can be found by [38]

$$N(x) = N_0 e^{-(\mu_{\text{en}}/\rho)\rho x}, \quad (10)$$

where  $N_0$  is the initial gamma flux,  $(\mu_{\text{en}}/\rho)$  is the MAC of  $\text{SiO}_2$ ,  $\rho$  is the density of  $\text{SiO}_2$ , and  $x$  is the depth of the ceramic cover. Utilizing the material parameters in Table 4,  $\approx 99\%$  of the gammas reach the inverter. After reaching the inverter, the maximum kinetic energy the gammas may impart on an electron,  $T_{\text{max}}$ , is [38]

$$T_{\max} = \frac{2h\nu}{2 + \frac{mc^2}{h\nu}}, \quad (11)$$

where  $h\nu$  is the energy of the gamma peak and  $mc^2$  is the rest mass of an electron at 0.511 MeV. Equation 11 suggests both gammas from the  $^{60}\text{Co}$  source produce a maximum kinetic energy transfer of 0.96 MeV.  $\text{SiO}_2$  requires 35 eV energy transfer for atomic displacement. Alternatively, only 18 eV are needed for ionizing effects through generation of EHPs in  $\text{SiO}_2$  [14]. Therefore, the majority of the gammas that penetrate the inverter maintain sufficient energy to induce both EHPs and atomic displacement.

**Table 4. Dose conversion parameters for photon energies around 1.2 MeV.**

Material	$(\mu_{\text{en}}/\rho)$ in $\text{cm}^2\text{-g}^{-1}$	Density $\text{-cm}^{-3}$	$CF_{\text{tissue}}$	Maximum Dose Rate
<i>Tissue</i>	$2.938 * 10^{-2}$	1.06	1	73 krad(tissue)-hr $^{-1}$
<i>Si</i>	$2.652 * 10^{-2}$	2.33	0.9	65.7 krad(Si)-hr $^{-1}$
<i>SiO<sub>2</sub></i>	$4.417 * 10^{-2}$	2.196	1.5	109.5 krad(SiO <sub>2</sub> )-hr $^{-1}$

The energy deposition and its effect depend upon both the dose and dose rate within the material. In order to provide a common frame of reference for dosimetry, the dose is often reported for a single material associated with the experiment. For this work, radiation interacted with many materials in the devices, including metals, ceramic packaging, and the Si and  $\text{SiO}_2$  of the inverters themselves. Thus, it was determined that the tissue equivalent standard dose would be used, as it could be accurately traced to the dosimetry system for the  $^{60}\text{Co}$  source. Conversion parameters for the photon energies used in this work are in Table 4.

### 2.2.3 High Energy Radiation Effects in CMOS Devices.

The CMOS inverter includes two metal oxide semiconductor field effect transistors (MOSFETs), a p-channel MOSFET (PMOS) and NMOS operating in conjunction.

Radiation effects for each transistor focuses on ionizing effects in the SiO<sub>2</sub> insulator and Si substrate. Permanent atomic displacement in the Si channel, primarily due to high energy neutrons or heavy ions, are a concern, but will not be considered in this research. Incident ionizing radiation generates EHPs in the oxide and substrate, where a percentage will immediately recombine. An electric field across a MOSFET drastically reduces the recombination of EHPs.

At room temperature, the mobility of electrons in SiO<sub>2</sub>,  $\mu_n$ , is 20 [ $\frac{cm^2}{V-s}$ ] compared to the mobility of holes,  $\mu_p$ , at  $10^{-5}$  [ $\frac{cm^2}{V-s}$ ] [25]. Ionizing radiation creates EHPs, some of which will immediately recombine. Of the surviving EHPs, the significantly more mobile electrons, under the influence of the gate bias, quickly exit the SiO<sub>2</sub>, leaving the mobile holes. The positively charged mobile holes account for a negative shift in gate threshold voltages for both the PMOS and the NMOS transistor.

The transport of the holes in the SiO<sub>2</sub> follows a continuous time random walk (CTRW) dispersive transport model [25]. The flat band voltage shift due to the holes depends on temperature, state of the transistor (voltage bias on the gate) and quality of the material. Assuming a positive applied bias, the radiation induced holes move toward the oxide-semiconductor interface where hole traps are also located. Assuming a homogeneous EHP distribution, the CTRW model suggests some holes will interact with the interface quickly, some clusters of holes will follow a short time later, and the remaining holes will make it to the interface at a much later time.

The arrival of holes at the Si/Si/SiO<sub>2</sub> interface results in another effect, the formation of interface traps ( $N_{it}$ ). Unlike the oxide traps,  $N_{ot}$ , interface traps exist only at the oxide-semiconductor interface, and have a significant effect on both recombination rates of carriers at the semiconductor surface and the mobility of the carriers [5]. After the initial transport of holes, which produces a negative threshold voltage shift for both NMOS and PMOS devices, the threshold then shifts more positive for NMOS



devices whereas the threshold continues to shift more negative for PMOS transistors. This shifting occurs on time scales on the order of seconds to hours, depending on the applied field and quality of the material.

The mechanism for the secondary threshold voltage shift in the NMOS after hole transport is attributed to the interface traps.  $N_{it}$ , which are negatively charged, may overcome the positively charged  $N_{ot}$ , leading to a voltage recovery. The time constant related to NMOS recovery depends on state condition of the device, dose rate, and material properties. Device rebound, the point at which the total negative threshold shift is overcome by a net positive shift, may occur.

Atomic displacement, primarily due to neutron and heavy ion interactions, causes more permanent damage than EHP production, and is critical in the channel region of a transistor. If a particle transfers enough energy to a Si atom, the atom may be ejected from its lattice site and a newly formed recombination center is formed. Since the channel is the path for which current is conducted, charges may become trapped due to the atomic displacement. The end result is a reduction in mobility for a transistor, leading to a reduction in device gain and increased propagation delay.

It is possible for photons to indirectly displace atoms [14]. A photon may produce Compton scattered electrons of energies up to 1.3 MeV, which in turn, may displace atoms.

#### **2.2.4 Dose Rate Considerations.**

Device response depends significantly on the dose rate. For instance, an enhanced low dose rate sensitivity (ELDRS) may amplify the degradation of MOS or bipolar junction transistors (BJT). With ELDRS, the space charge, due to the generation of EHPs, remains in the passivated dielectric material and permits the dispersion of charge. At higher dose rates, the space charge limits the further charging of the

material [14], and thus avoids the ELDRS effects.

High dose rate effects, also called transient radiation effects in electronics (TREE), defines when the flux from the radiation source produce EHP concentrations greater than the doping concentration of the device [14]. The generated charge may overwhelm the applied bias to the device, motivating current to proceed in the opposite direction as intended. This can induce sudden bit flips due to the significant photocurrents.

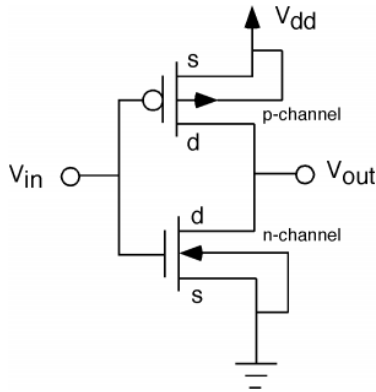


**Figure 8. Schematic of two transistors, an NMOS and PMOS, connected to function as a single CMOS inverter.**

### 2.3 The CMOS Inverter

Full comprehension of any complex and detailed IC requires the understanding of its fundamental building block. One such common block is the CMOS inverter. The CMOS inverter incorporates two MOSFETs working in conjunction. A schematic of a CMOS inverter is shown in Figure 8. In the inverter, the gates of the PMOS and NMOS are connected and serve as the input node to the inverter. The source and substrate contacts of NMOS devices are grounded, whereas those of PMOS transistors are connected to the power supply,  $V_{DD}$ . A cross sectional view of a CMOS inverter is shown in Figure 9 [36].

The CMOS design in Figure 9 portrays the functionality of a CMOS device, but

fails to identify modern IC manufacturing processes. As shown in Figure 10, modern CMOS devices include many complex layers. The surface of a CMOS device may incorporate heavy-metal layers embedded with passivated dielectric material. Additionally, buried oxide, lightly doped drain, high  $k$  dielectric, and shallow trench isolation (STI) may be included in modern devices to prevent latch up, unwanted leakage currents, or moisture and air ionization [14].

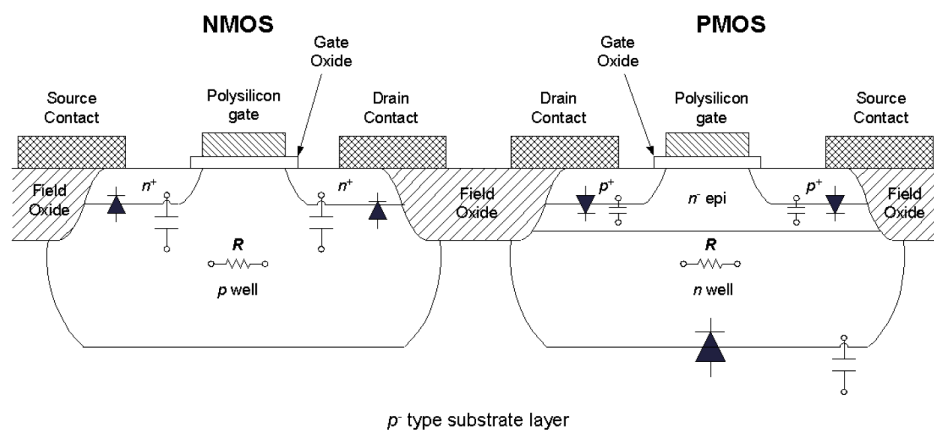


Figure 9. Cross section of a CMOS inverter.

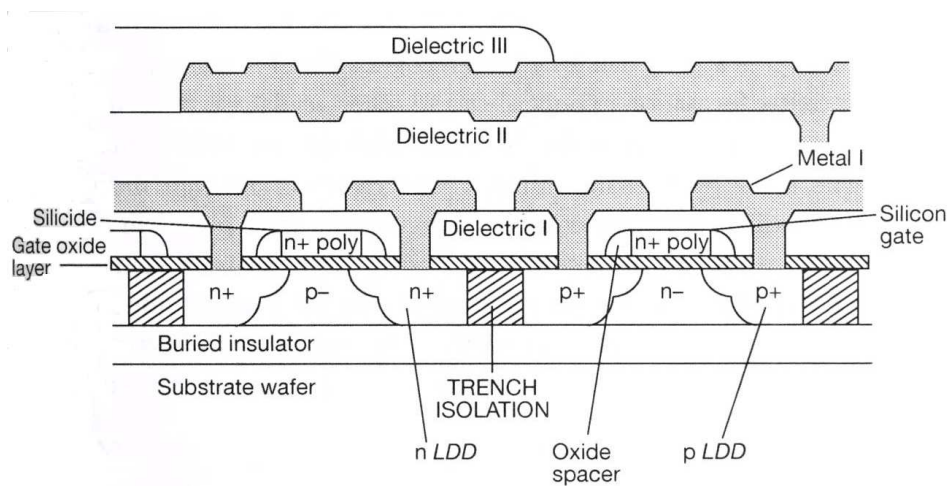


Figure 10. Cross section of a CMOS inverter illustrating new IC processing techniques.

### 2.3.1 Static Characteristics.

When the input voltage is at ideal low,  $V_{in} = 0$ , the NMOS is off because the NMOS threshold voltage,  $V_{Tn}$ , exceeds the input. While the NMOS acts as an open circuit, the PMOS is in the linear active region due to the fact that  $V_{DD}$  is greater than the threshold voltage for the PMOS ( $V_{Tp} < 0$ ). In the active triode region, the transistor operates close to a closed circuit device, with the small transistor resistance ( $r$ ) given as [34]

$$r_p = \frac{1}{k'_p \left(\frac{W}{L}\right)_p (V_{DD} - |V_{Tp}|)} \quad (12)$$

where  $k'_p$  is the transconductance and  $(W/L)_p$  is the transistor dimension ratio. Therefore, the output node,  $V_{out}$ , is charged to  $V_{DD}$  through the PMOS with only a minimal voltage drop determined by the PMOS transistor resistance,  $r_p$ . Equation (12) and all of the corresponding variables apply for the NMOS transistor as well.

When the input voltage is at ideal high ( $V_{in} = V_{DD}$ ), the NMOS is operating in the active triode region since  $V_{DD}$  is greater than the threshold voltage for the NMOS. The NMOS appears as a near closed circuit, only attenuated by the NMOS resistance,  $r_n$ , similarly illustrated in Equation (12). In this case, the PMOS is turned off and acts as an open circuit. Therefore, the output node is discharged to ground through the NMOS device [36]. The end result of the inverting operation of the CMOS inverter is the digital transfer table, commonly referred to as the truth table, shown in Table 5.

**Table 5. Inverter truth table**

Input	Output
0	1
1	0

When the output is in a steady state condition of either  $V_{out} = V_{DD}$  or  $V_{out} = 0$ ,

only one transistor is turned on. The current from the power supply to ground is therefore very low, due to the leakage current of the off device. In fact, there is significant current conduction only during the short transient period when the two devices are temporarily on. Only leakage currents exist during static operation, leading to very low power consumption compared to other types of logic circuits.

The threshold voltage of a transistor represents the point at which a sufficient number of minority mobile charges accumulate in the substrate to form a conducting channel. For a CMOS inverter, the NMOS and PMOS threshold voltages define the transition between a small leakage current and significant conduction. Digital MOSFET threshold voltages usually range between 0.45 to 1.7 V [1], [2].

When the input voltage to an inverter is within the threshold voltage bounds as  $[V_{Tp} < V_{in} < (V_{DD} - V_{Tn})]$ , both the NMOS and PMOS devices will operate simultaneously. When both transistors are conducting, significant power consumption will take place. The currents generated by the PMOS and NMOS transistors,  $i_{DP}$  and  $i_{DN}$ , are dependent upon the state of the transistor. For certain input voltages, either transistor may be in the active triode or saturation regions where  $i_{DP}$  is given by [34]

$$i_{DP} = k'_p \left( \frac{W}{L} \right)_p [(V_{DD} - V_{in} - |V_{Tp}|)(V_{DD} - V_{out}) - \frac{1}{2}(V_{DD} - V_{out})^2], \quad (13)$$

for  $V_{out} \geq V_{in} + |V_{Tp}|$  in the triode region of the PMOS, or

$$i_{DP} = \frac{1}{2} k'_p \left( \frac{W}{L} \right)_p (V_{DD} - V_{in} - |V_{Tp}|)^2, \quad (14)$$

for  $V_{out} \leq V_{in} + |V_{Tp}|$  in the saturation region of the PMOS.

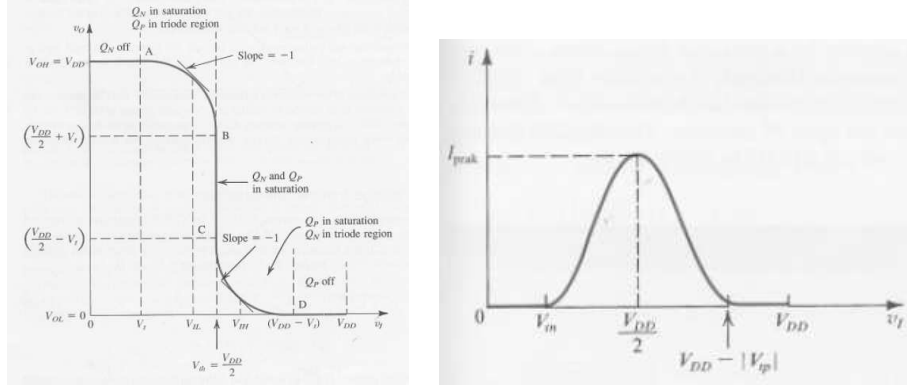
NMOS conduction currents,  $i_{DN}$ , are given similarly as

$$i_{DN} = k'_n \left( \frac{W}{L} \right)_n \left[ (V_{in} - V_{DD})V_{out} - \frac{1}{2}V_{out}^2 \right], \quad (15)$$

for  $V_{out} \leq V_{in} - |V_{Tn}|$  in the triode region of the NMOS, or

$$i_{DN} = \frac{1}{2}k'_n \left( \frac{W}{L} \right)_n (V_{in} - V_{Tn})^2, \quad (16)$$

for  $V_{out} \geq V_{in} - |V_{Tn}|$  in the saturation region of the NMOS.



(a) CMOS inverter ideal voltage transfer characteristic (VTC). An ideal inverter consists of a perfect CMOS inverter presents a symmetric current pulse, with the maximum current peak at  $V_{DD}/2$ . (b) CMOS inverter ideal current transfer characteristic (CTC). An ideal inverter presents a symmetric current pulse, with the maximum current peak at  $V_{DD}/2$ .

**Figure 11. Ideal CMOS transfer characteristics [34].**

Depending on the input bias, Equations (13) through (16) represent the current driven by each transistor where each transistor current must be equal at the output node. If an inverter is assumed to be matched, having equal ratios of transistor transconductance and equal dimensions, then the voltage transfer characteristic will be symmetrical. A CMOS inverter is said to be matched if [34]

$$k'_n \left( \frac{W}{L} \right)_n = k'_p \left( \frac{W}{L} \right)_p \quad (17)$$

for the NMOS and PMOS transistor in the inverter. For a matched inverter, the transistor threshold voltages are equal and therefore annotated as a single threshold voltage,  $V_T = V_{Tn} = V_{Tp}$ . Assuming a matched inverter, the equivalent currents at each input voltage lead to the output voltage ( $V_{out}$ ) transfer characteristic.

The CMOS inverter voltage transfer characteristic (VTC) is shown in Figure 11(a) with corresponding transistor states. The current transfer characteristic (CTC) of an inverter illustrates the output current driven by the currents in Equations (13) - (16), as shown in Figure 11(b). Figure 11(a) clearly presents an unstable region where  $V_{in} \approx V_{out}$ . Within this region, both transistors are in the saturation mode, with a maximum current dissipation. Not only does the inverter dissipate considerable current, but the output logic state is essentially unknown.

### 2.3.2 Dynamic Characteristics.

The speed of operation in a CMOS inverter, and thus any digital IC technology, relies on the propagation delay [34]. The internal NMOS and PMOS transistor's charge and discharge current, depending on the input voltage, is characterized as an inverter capacitance,  $C$ . When an ideal square pulse toggles the inverter, the inverter cannot respond immediately. Instead, the response time to produce the inverted signal, known as the rise and fall times,  $t_r$  and  $t_f$ , are given as [34]

$$t_r = \frac{1.6 C}{k'_p \left(\frac{W}{L}\right)_p V_{DD}} \quad \text{and} \quad (18)$$

$$t_f = \frac{1.6 C}{k'_n \left(\frac{W}{L}\right)_n V_{DD}}. \quad (19)$$

At an input of  $V_{DD}$ , the PMOS is turned off and the discharging of the NMOS transistor directs the fall time. Similarly, an input of ground voltage turns the NMOS

off and the active PMOS device relates to the rise time. The only power dissipated occurs when each transistor is conducting. When the inverter completes the response, such as signal inversion, only leakage current remains as shown in the static development.

### 2.3.3 Circuit Stability.

For any IC device, the maximum permitted “Logic 1”, minimum permitted “Logic 0”, and noise margins define the stability and quality of its design. The high level at the input,  $V_{IH}$ , along with  $V_{DD}$ , define the maximum permitted “Logic 1” region, which allows for proper state change for a high voltage input. Conversely, the low level at the input,  $V_{IL}$ , along with ground, define the minimum permitted “Logic 0” region, which allows proper state change for the low level. Both safe state transition regions are calculated as [34]

$$V_{IH} = \frac{1}{8}(5V_{DD} - 2V_T), \text{ and} \quad (20)$$

$$V_{IL} = \frac{1}{8}(3V_{DD} + 2V_T). \quad (21)$$

The noise margins quantify the sensitivity to external noise that may interfere with the operation of the device. The noise margin for high input,  $NM_H$  and low input,  $NM_L$  is given as [34]

$$NM_H = NM_L = \frac{1}{8}(3V_{DD} + 2V_T) \quad (22)$$

for the CMOS inverter. For a matched inverter, the symmetry of the transfer characteristics produces equal noise margins for high and low sensitivities. The activation voltage for the device is called the switching point. At this voltage, the inverter will



alter the state of the device from low to high or high to low. The switch point voltage,  $V_{sp}$  is defined as

$$V_{sp} = \frac{\sqrt{\frac{k'_n(\frac{W}{L})_n}{k'_p(\frac{W}{L})_p}} V_T + (V_{DD} - V_T)}{1 + \sqrt{\frac{k'_n(\frac{W}{L})_n}{k'_p(\frac{W}{L})_p}}} \quad (23)$$

for a matched inverter [4]. For an ideal inverter, the switching voltage should be  $\frac{V_{DD}}{2}$ , providing a symmetric, stable transition.

### **III. Experimental Methodology**

The following section develops the experimental process utilized during the research. First, previous radiation effects experiments, and their comparison to our research, are discussed. Then, details into the experimental hardware design, control software necessary to manipulate the test equipment, and the device under test (DUT) remotely are provided. Finally, the process established to gather the experimental results will be developed.

#### **3.1 Comparison of Research to Previous Studies**

Due to its importance, it is no surprise that electronic susceptibility has been extensively investigated. The following thesis description aims to confirm previous conclusions as well as address uncharted territory.

The injection method was chosen for conducting EMI effects on the inverters. An injection experiment usually incorporates the coupling of an EMI signal with the input bias of the device. From an operational standpoint, most intentional HPM interference would be directed to a target by means of free field illumination. Once the EM radiation interacts with the media, in this case the digital electronic device, some of the energy will couple into the system as induced currents. As to where on the device the induced currents are present are related to the orientation of the device, geometry of the device, and the position of the incident HPM fields. Therefore, the HPM interference could very well present itself at any port of the device, not just the input.

The approach of most EMI research is to direct inject the interference into a circuit instead of illuminating it in a free field radiation experiment. Free field radiation experiments benefit from a realistic environment, considering intentional EMI would

be transmitted through free space in most cases. But, the controlled environment of a direct injection experiment allows one to perform measurements while accumulating accurate data. Additionally, proper experiments must take into account the complex coupling of the EM radiation into a device and the radiation pattern of the antenna. The additional equipment, such as an anechoic chamber and HPM source, required for free field testing solidify the injection method as the preferred technique. Lastly, the direction injection method allows for the simultaneous testing of both HPM and ionizing radiation with the facilities available.

Most research in HPM effects have focused on the signal parameters shown in Table 6. Table 6 presents components of the HPM radiation, defined by the frequency, pulse length, pulse repetition frequency (PRF), and power. The HPM frequencies of interest in this research were dictated by the inverter coupling efficiency. The HPM frequency selection is discussed in Section 4.2.

**Table 6. Common HPM field characteristics in previous research**

Parameter	Common Values
Frequency	Between 1 - 2 GHz
Pulse Length	100 ns
PRI	1 kHz
Power	0 - 24 dBm (1 - 251 mW)

Much focus has been dedicated to total ionizing dose total ionizing dose (TID) effects. The current research combined TID with HPM and explored any differences associated with dose rate effects were practicable. TID is inherently included in the research due to time varying effects of the DUT with respect to the  $^{60}\text{Co}$  source.

The two radiation effects in electronics, HPM and ionizing radiation, have been extensively studied independently. No attempt has been made to identify the nature of electronic upsets to both forms of radiation concurrently. The proposed research

aspires to conduct both HPM and ionizing radiation experiments simultaneously, while extracting data from the device.

Previous research in electronic effects have tested numerous devices. The experiments have ranged from individual logic devices, such as 4 bit adders, to large structures containing electrical equipment, such as cars [3], [12], [25], [24]. In this research, modern and mature CMOS digital inverters were examined. The CMOS inverters represent the latest technology available in common electronics. Results from the experiments performed in this research allow for a relationship to be identified between advanced and older CMOS inverters, thus establishing a radiation effects trend with obsolete devices. Similarly, understanding radiation effects in a CMOS inverter allows for a connection between the driving mechanisms behind the degradation to a prediction capability of more complex devices.

### **3.2 Selection of the Experimental Devices**

Radiation effects on electronics is critical to technology-driven societies. There are many types of transistor-based ICs that form the foundations of electronic devices. This research focused on a prevalent technology found in everyday ICs. The inverter provides the added benefit of a simplistic characteristic model yet contains both NMOS and PMOS transistors. It therefore contains the elementary characteristics of all ICs and will allow for more universal failure analysis.

Other types of inverting structures were considered for the radiation effects experiments. Gallium arsenide based devices, such as metal semiconductor field effect transistors (MESFET) and transistor transistor logic (TTL) devices were considered. Since the trend for electronic design has drifted toward CMOS technology, their response due to ionizing radiation and HPM proved most relevant.

After contemplating the plethora of CMOS inverters available, an obsolete hex

inverter as well as an advanced low power single gate inverter were chosen. Since the hex inverter's specification and performance has been well established, the device provided a means to verify the experimental approach. Additionally, the comparison of results between obsolete and modern inverters bridged generations of CMOS technologies, thus generating a trend for the relative susceptibility to ionizing radiation and HPM.

Low power inverters were tested for the following four reasons:

- Current manufacturing processes are driving toward smaller size and faster operation.
- To ascertain maximum performance, each transistor requires lower power requirements. Future COTS equipment will contain lower power circuit design to meet reduced power consumption requirements.
- The electronics effects research on CMOS devices has focused on older transistor technology, including devices with normal power consumption and manufacturing at the 1 to 4  $\mu\text{m}$  level. Advanced transistors are fabricated at the sub micron level. Experimentation on low power inverters would confirm the hypothesis of an increased susceptibility to intentional radiation with smaller devices.
- Modern IC manufacturing processes include additional device features, to include multilayer dielectric shielding, buried oxide layers, and trench isolation, to name a few. Such new features may prompt alternate responses to radiation when compared to older technology.

The Texas Instruments SN74AUC1G04 single inverter gate was designed to operate at lower voltage thresholds, optimized for the power and input voltage range of 0 to 3 V. The single gate inverter consists of a PMOS-NMOS transistor pair, with a

total of four terminals. Two of the terminals function as the input and output port to the CMOS inverter, while power and ground ports complete the remainder [2].

Similarly, the Texas Instruments CD4069UB Hex Inverter consists of 6 pairs of PMOS-NMOS transistor pairs, for a total of 12 transistors. Of the total 14 pins, 12 correspond to inputs and outputs for the PMOS-NMOS pairs, while the remaining 2 pins are for power input and ground [1].

The design of the hex inverter allows for an input and power operation range of 5 to 20 V. The experiments in this research focused on 5 V input and power voltage operation in order to maintain a similar operation to the advanced inverter. Figure 12 shows the pin diagram for the TI inverters tested during the experiments and the symbolic diagram of an inverter.

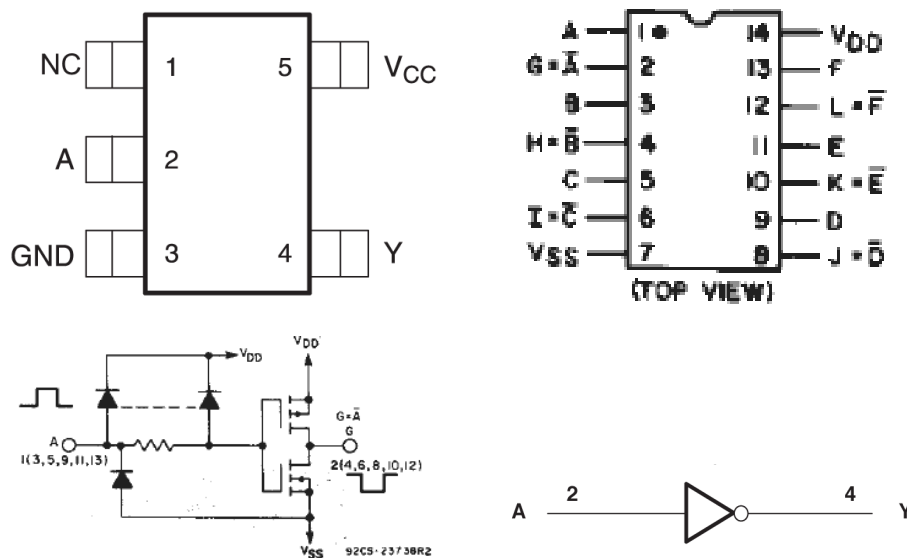


**Figure 12. Terminal assignments for the AUC1G04 and CD4069UB CMOS inverter devices. Schematic layout and symbolic representation of an inverter [1], [2].**

A naming convention for the inverters was developed to maintain clarity and structure. All advanced single gate inverters tested, TI SN74AUC1G04 chips, are identified as B inverters. All TI CD4069UB Hex Inverters are referred to as A inverters.

### 3.3 Experimental Setup

The experimental setup, as shown in Figure 13, allowed for HPM and ionizing radiation measurements concurrently. Input and power biases ( $V_{in}$  and  $V_{DD}$ ) were applied to the device with a semiconductor analyzer. Output signals ( $V_{out}$  and  $I_{out}$ ) were also measured with the semiconductor analyzer. A spectrum analyzer and vector network analyzer VNA were used to confirm high frequency coupling in the setup, as discussed in Section 4.2. The IEMI HPM signal, supplied by a signal generator, provided continuous wave (CW) fields within the frequencies of interest. Since higher frequencies result in higher inductance, and thus cannot easily be transmitted to the device, SubMiniature version A (SMA) cables connected all signals with AC components. The lower inductance minimized distortion of the circuit signals. Further details, including part list, is shown in Appendix A.

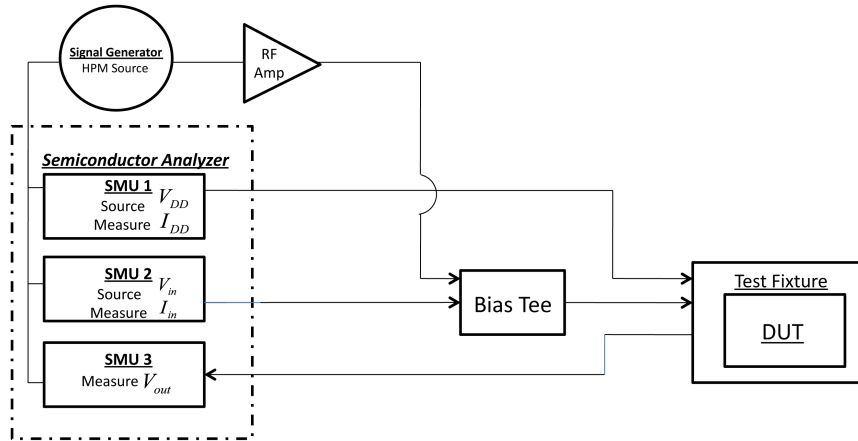


Figure 13. Experimental setup.

The experimental setup included a bias tee to couple the HPM signal with the

static input bias. The output of the bias tee, a signal incorporating the direct current (DC) input bias and the alternating current (AC) HPM signal, provided the injected signal into the device input. The bias tee included a blocking capacitor for the AC signal and inductor connected to the DC line.

The bias tee produced a low and high pass filter (LPF and HPF), where the impedance of the capacitor  $Z_C$  and inductor  $Z_L$  is determined by the operating frequency, capacitance ( $C$ ), and inductance ( $L$ ) as shown in Equations 24 and 25 [16].

$$Z_C = \frac{1}{j\omega C} \quad (24)$$

$$Z_L = j\omega L \quad (25)$$

The inductor stage, the LPF, maintained the static input bias as long as the frequency components of the signal remain lower than the cutoff point in the LPF. The experimental setup considered only static input biases, so the DC coupled signal line worked properly. If a dynamic signal with frequency components higher than the cutoff point were coupled in, the signal injected into the device would be distorted and cause inaccuracies in the measurements. The capacitor component, the HPF, only allowed frequencies above the cutoff point to proceed to the device input. As long as the frequency components of the HPM signal were greater than the cutoff point, then the signal passed through as an approximate matched load. The voltage standing wave ratio (VSWR), which quantifies the reflections for the DC and AC signals, measured a maximum reflection ratio of 1.2 at 1.8 GHz. All other frequencies between 0.8 to 12 GHz maintained a small VSWR. Therefore, reflection of injected HPM signals was kept to a minimum.



### 3.3.1 High Frequency Test Considerations.

To ensure maximum energy transfer from the source to the inverter, the output impedance of the bias tee was matched to the input impedance of the device. When the operation frequency was increased, the impedance matching condition became more vital [16]. This unmatched load increased signal reflections and unwanted signal error.

The test fixture, shown in Figure 14, incorporated a capacitor connected with a  $50\ \Omega$  resistor in a parallel arrangement across the device input whenever possible. Therefore, the input to the device closely matched the incoming transmission impedance, maximizing the energy transfer while minimizing signal distortion (lower VSWR). Appendix B contains additional diagrams and details concerning the test fixture design.

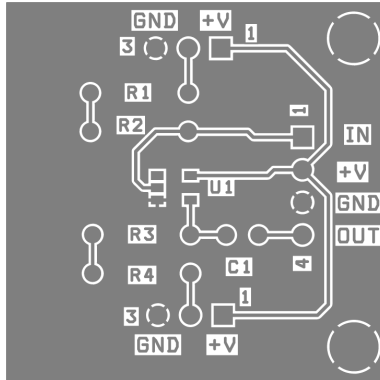


Figure 14. Device under test (DUT) design. Impedance matching techniques and striplines allowed for efficient high frequency coupling.

## 3.4 Experimental Procedures

The experimental processes described below allowed for the measuring and verification of HPM and ionizing radiation effects on CMOS inverters.

### 3.4.1 Radiation Parameters and Signal Measurements.

To characterize the effects of radiation and HPM on the devices, inverter VTC and CTC plots were produced and analyzed. Device parameters, including threshold voltages, device gain, leakage currents, and maximum current peak, were calculated and derived from the VTC and CTC graphs, as described in Section 2.3. The VTC and CTC measurements were obtained by applying an input bias sweep to the DC port of the bias tee while holding a constant power voltage, as described in Section 3.3. A Visual Basic program was written to control the experimental hardware, manage the experimental parameters, perform the sweep functions, and store the necessary variables. Appendix C contains a flow chart illustrating the procedures for all experiments.

Device and radiation parameters were adjusted to identify key factors in device performance. Table 7 contains the modified parameters in the research. Input and supply biases were adjusted with the SMUs while the HPM frequency and power adjustments were controlled by the signal generator. The exposure time of the device within the  $^{60}\text{Co}$  source allowed for the control of the dose. Similarly, the dose rate was altered by adjusting the position of the inverters relative to the  $^{60}\text{Co}$  source.

**Table 7. Controlled experimental parameters and analyzed inverter parameters.**

Research Controlled Parameters	Analyzed Parameters
$V_{DD}$	VTC
$V_{in}$	CTC
Inverter model	$V_{th}$
HPM frequency	$V_{sp}$
HPM power	Device gain
$\gamma$ total dose	$I_{max}$
$\gamma$ dose rate	$I_{leak}$

The steps for incorporating the HPM and ionizing radiation effects proceeded as follows:

1. Pre-characterize devices to include VTC, CTC, input impedance and device parameters.
2. HPM radiation effects to include VTC, CTC, and device parameters.
3. Ionizing radiation effects to include VTC, CTC, and device parameters.
4. Simultaneous ionizing and HPM radiation effects to include VTC, CTC, and device parameters.

The first two steps were completed at the AFIT nuclear science laboratory, while the final two steps required the OSURR.

## IV. Results

This chapter provides the analysis of the experimental measurements, presents trends in the data and develops conclusions for the research. The experimental setup was verified by comparing inverter performance to design specifications. Various experiments were conducted to analyze the functionality of the inverter with and without HPM and ionizing radiation.

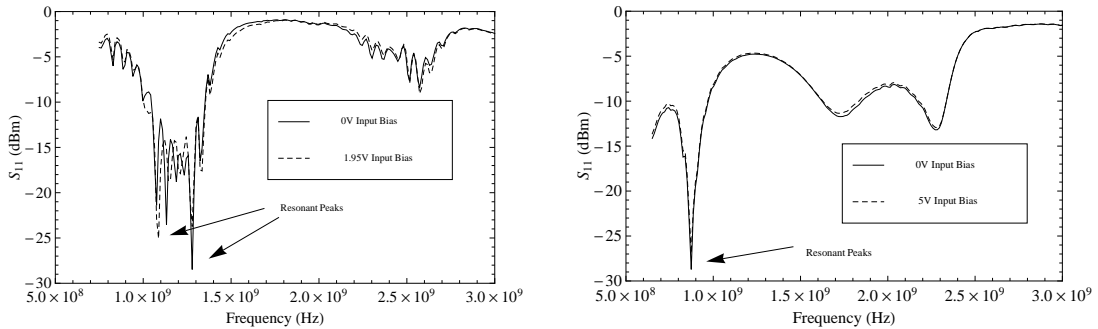
### 4.1 Experimental Verification

Each inverter was characterized, with VTC and CTC plots, and compared to data specifications provided by the manufacturer. Each measurement was within tolerance, verifying the experimental setup process described in Section 3.3. Multiple iterations of device characterization were performed to insure repeatability of results.

### 4.2 High Frequency Coupling Efficiency

In order to validate results from EMI experiments, one must first confirm the EM energy couples into the device. Otherwise one could conclude EMI immunity for a device at a specific frequency range, when in reality the experimental setup may have filtered the EMI energy.

Two experiments were conducted in order to quantify the inverter response to EMI. In the first experiment, an Agilent 8720ES VNA measured the signal reflected from the inverter apparatus. A Maury 8050C 3.5 mm calibration kit allowed for the compensation for losses and delays in the SMA cables between the VNA and test fixture. During the experiment, a DC coupled bias was connected to the VNA. In essence, the VNA setup mirrored the VTC and CTC experiments discussed in Subsection 4.3.1, but the return signal, not the device output response, was measured.



(a)  $S_{11}$  measurement for a B Inverter. Different DC biasing conditions shifted the resonant frequency by 200 MHz. (b)  $S_{11}$  measurements for an A Inverter. Even with different biasing conditions, the resonant frequency remained approximately 850 MHz.

**Figure 15. Vector network analyzer (VNA) measurements for A and B Inverters illustrating the resonant frequencies.**

Once the calibration signal (set at 0 dB power) was transmitted to the device, the reflection coefficients ( $S_{11}$ ) was measured from 750 kHz to 3 GHz, with a 3 kHz bandwidth. The  $S_{11}$  calculations, essentially the complement of the energy transferred into the inverter, produced the frequency dependent energy reflected from the device. Figure 15 presents the  $S_{11}$  reflection coefficient frequency dependent measurements for both A and B inverters. Both devices have a resonant peak, at 850 MHz for A inverters and 1.3 GHz for B inverters. Within the peak, the reflected power was reduced by 20 to 25 dB. Therefore, there is a higher efficiency for power transmission within the resonant region.

Depending on the input bias, both the A and B resonant peak responded with a shift of 20 MHz. This is likely due to a change in the MOSFET channel, in which the internal capacitances and inductances were responsible for the shifting resonant peak. Previous research identified a similar shift in resonance due to input conditions [13]. The higher order harmonics that produced the rough curve for the B inverters, shown in Figure 15(a), likely attributed to the PCB stripline DUT design.

The A inverters have a lower switching time compared to the B inverters. The 4069UB inverters have switching times of 75 ns where the AUC class switch is 2 ns, or

nearly 38 times slower [1], [2]. With faster switching speeds, the B inverters respond more efficiently to higher frequency HPM signals. The VNA measurements verify this.

Another high frequency coupling efficiency experiment included the signal generator and an Agilent E4407B Spectrum Analyzer. Similar to the VNA experiment, the experiment aimed to identify the frequency dependent coupling efficiency of the inverter. Here, the signal generator used in later experiments provided the injected HPM signal while the output of the inverter was connected to the spectrum analyzer. No power or bias was applied to the inverters. Instead of measuring the return energy of the EMI, the experiment measured the transmitted RF energy through the device.

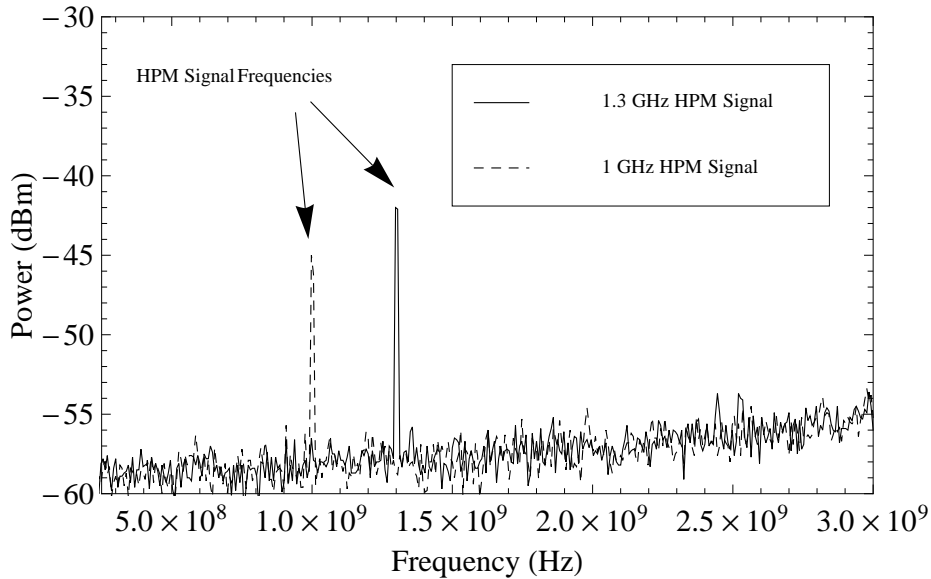


**Figure 16. Spectrum analyzer results for a B inverter.**

The transmitted energy for a B inverter is shown in Figure 16. Figure 16 results in one of two conclusions; the energy from the signal generator may disrupt the device functionality or the energy propagates through the device unimpeded, leaving the device in proper operation. In either case, the measurement confirmed that the maximum transmitted energy was at the same frequency as the applied HPM signal.

### 4.3 Inverter Response to HPM and Ionizing Radiation

The following section presents the effects on inverter transfer characteristics, such as VTCs and CTCs, and more specific parameters, such as effects on threshold voltages, switching points, maximum current dissipation, leakage currents, and device gain. Each subsection includes analyses from isolated effects from HPM and ionizing radiation as well as the combined effects. Each section presents results and analyses for old (A) and new (B) CMOS inverters.

#### 4.3.1 Radiation Effects on Device Transfer Characteristics.

##### 4.3.1.1 Radiation Effects on VTC.

##### 4.3.1.2 A Inverters and the VTC Response.

The VTC defines the susceptibility of an inverter to signal noise. Additionally, the VTC illustrates the symmetry of the logical switching region. For an ideal logic VTC, the state change occurs half way between the input voltage range, or at  $V_{DD}/2$ .

The radiation and HPM effects on the VTC depends on multiple factors, including radiation source, inverter state, and inverter technology. VTC response to ionizing radiation only will be presented first.

Figure 17 presents the dose dependent VTC shift for a low input LI ( $V_{in} = 0$  V) ionizing radiation test only. The image illustrates the time varying VTC results for an A inverter. The normal operating VTC immediately shifted to a lower voltage when irradiated. After 109 krad(tissue) dose, the VTC translated approximately 0.55 V. Post irradiation, the VTC shifted toward a higher voltage, falling short of the pre radiation VTC position. 120 minutes following irradiation, the VTC translated positive by 0.15 V. The shifting pattern of the VTC from ionizing radiation, due to creation and transport of holes, is further described in Subsubsection 4.3.2.1.

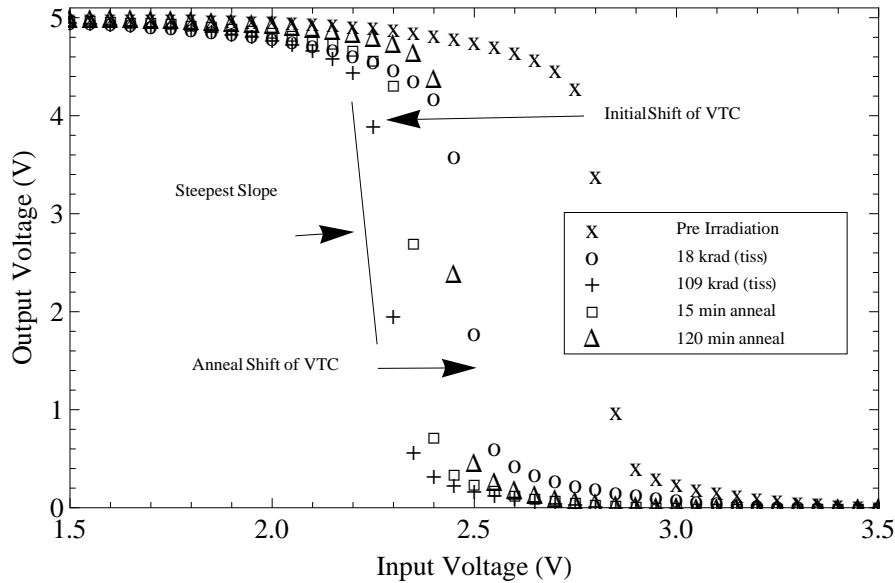


**Figure 17. VTC effects for ionizing only low input state condition on an A inverter. The dose rate was 73 krad(tissue)/hr and was irradiated for a total dose of 109 krad(tissue).**

The steepness of the VTC transfer curve, which is related to the device gain, was also changed during the irradiation. At 18 krad(tissue) total dose, the VTC curve flattened, resulting in a reduced gain. After 109 krad(tissue) dose, the VTC curve reversed its trend, producing an increased slope. VTC slope behavior is covered in Subsubsection 4.3.2.5.

An identical experiment was performed, but with only adjusting the input voltage condition in order to isolate effects dependent on device state. Image 18 shows the VTC response when the inverter was maintained with a logical high input HI ( $V_{in} = V_{DD}$ ). The A inverter VTC shifted to a lower voltage during the test, further than the low bias experiment. For the same dose, the VTC shifted by more than 1.9 V, or nearly 3 1/2 times the low input experiment. Input condition dependency is further discussed in Subsection 4.3.2.

Similar to the low input test, the VTC began to recover to its original value of 2.9 V after irradiation. The final measurement revealed a higher voltage of 0.25 V, indicating a more aggressive recovery compared to the low input experiment. The



VTC effects are discussed in Subsubsection 4.3.2.2.

The input state of the inverter not only effected the shifting of the VTC, but also the slope of the transfer curve. The VTC transfer curve slope gradually decreased with increasing total dose, thereby reducing the maximum output voltage. After a total dose of 109 krad(tissue), the maximum output voltage was reduced from 4.999 V to 4.406 V, or a drop of nearly 12%. Figure 19 demonstrates the VTC response for low and high input state measurements. Further discussion concerning the VTC slope is covered in Subsubsection 4.3.2.5.

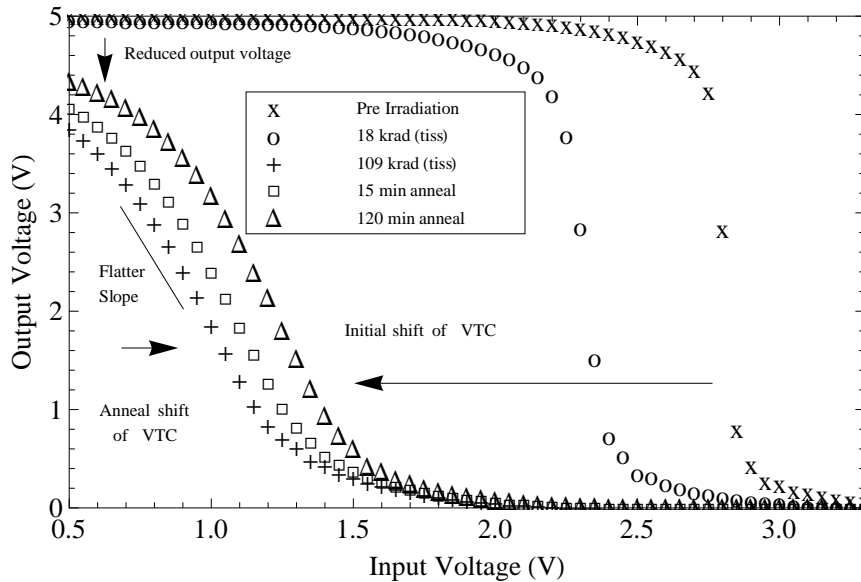


**Figure 18.** VTC effects for ionizing only high input state condition on an A inverter. The dose rate was 73 krad(tissue)/hr and was irradiated for a total dose of 109 krad(tissue).

Dose rate dependencies, such as ELDRs and TREE were investigated. Identical experiments were performed for the low input inverter state, with a low dose rate of 36.5 krad(tissue)/hr. During and after irradiation, the low dose rate VTC time response resembled the maximum dose rate case described previously. The VTC plots indicated an initial negative voltage shift of the VTC during irradiation, then a positive voltage shift after irradiation. Also, the slope behaved similar to the VTC

response to the maximum dose rate. Only small changes in parameters were observed, attributed to dose dependent leakage currents, as described in Subsection 4.3.2.

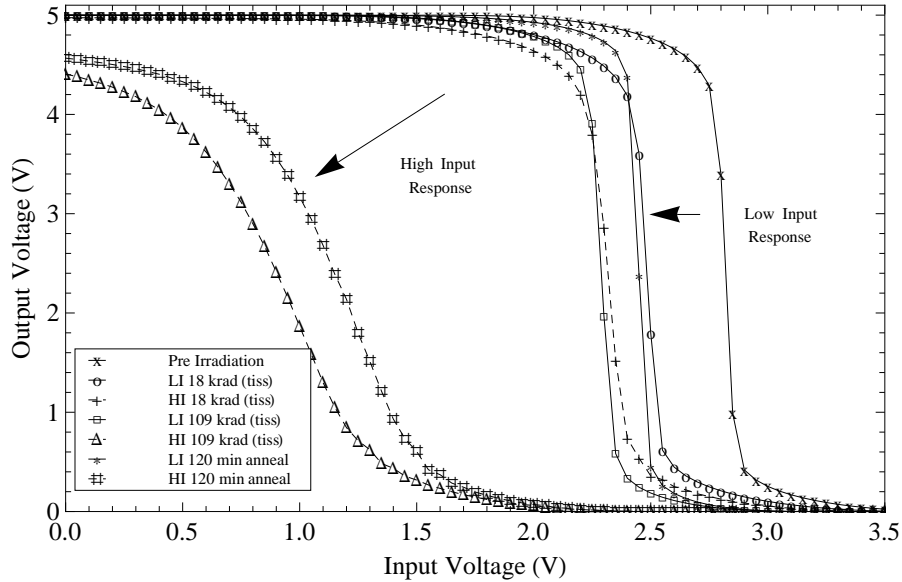


**Figure 19. VTC effects for ionizing only irradiation on an A inverter. Both the low and high input state condition effects are shown for a dose rate of 73 krad(tissue)/hr and total dose of 109 krad(tissue).**

Isolated HPM effects experiments were also conducted. For HPM only effects, time dependent response as well as inverter state were not applicable. Instead, time invariant VTC plots were generated for each HPM signal injected into the CMOS inverters. The frequency dependent VTC effects for the A inverters are presented in Figure 20. All other factors were the same and the frequency was only adjusted for the injected HPM signals. The HPM signals injected into the A inverters had the following parameters.

- HPM 1  $\Rightarrow$  250 kHz 26 dBm CW signal
- HPM 2  $\Rightarrow$  500 kHz 26 dBm CW signal
- HPM 3  $\Rightarrow$  10 MHz 26 dBm CW signal
- HPM 4  $\Rightarrow$  250 MHz 26 dBm CW signal

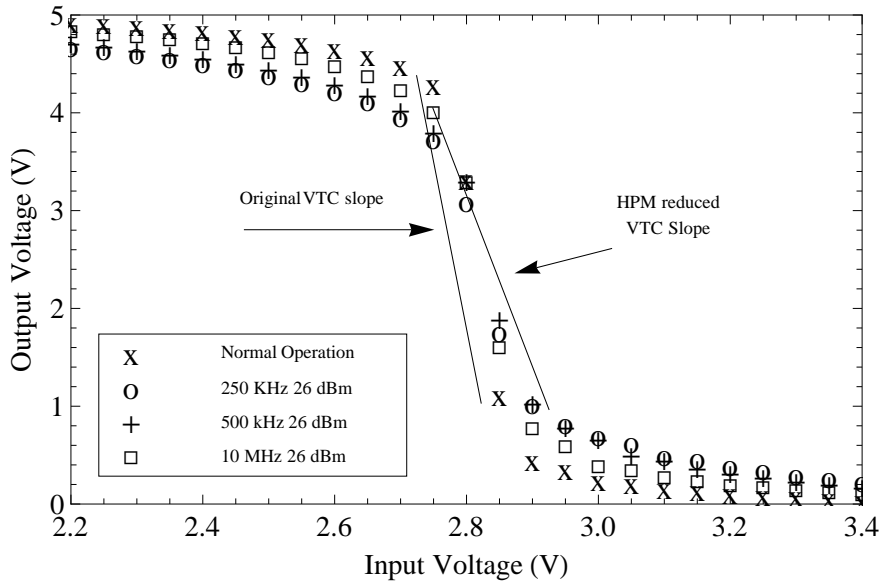


**Figure 20.** VTC response due to various HPM signals on an A inverter. All HPM CW signals had 26 dBm power.

For the A inverter experiments, all HPM signals were injected with 26 dBm power, the maximum power provided by the RF amplifier. Unfortunately, the test fixture for the A inverters limited the HPM frequencies to the kHz range. Unlike the B inverter fixture, high frequency coupling for the A inverter fixture was inefficient in the GHz range, severely attenuating the HPM signal. From Section 4.2, VNA experiments suggested a resonant peak at 850 MHz. When an 850 MHz HPM signal was coupled into the A fixture, no measurable effects were identified. It is believed the experimental apparatus for the A inverters does not reflect the injected HPM signal, but attenuated the HPM signal sufficiently to prevent device effects. It is anticipated that a PCB design (similar to the B inverter design) would increase the higher frequency power delivered to the inverter. Therefore, all HPM related effects for the A inverters focused on the kHz range due to experimental fixture limitations.

As shown in Figure 20, the lower HPM signal frequency produced more degradation to the VTC. The maximum permitted “Logic 1”,  $V_{IH}$ , and minimum permitted “Logic 0”,  $V_{IL}$ , as shown in Subsection 2.3.3, diverged outward with an injected HPM

signal, increasing the width of the transition region. The  $V_{IH}$  and  $V_{IL}$  corresponding output voltages,  $V_{OH}$  and  $V_{OL}$ , characterize the device gain. The gain of the inverter, a calculation which defines the performance of an inverter, reduced with an injected HPM signal. In the worst case, the 250 kHz HPM signal reduced the gain from 8.3 to 4.7, or a 43% drop. Conversely, the switch point voltage of 2.9 V for the A inverter remained constant independent of an injected HPM signal. Therefore, early interpretation of the data suggested that the ionizing radiation caused the shifting of the VTC curve.

The change in VTC gain for the hex inverters is shown in Table 8. The 250 kHz 26 dBm (HPM 1) signal generated the most significant VTC distortion, leading to the greatest reduction in gain.

**Table 8. Comparison of normal operation and HPM effects for VTC on an A Inverter. Corresponding voltages relate to device gain.**

HPM Conditions	$V_{IL}$ (V)	$V_{IH}$ (V)	$V_{OL}$ (V)	$V_{OH}$ (V)	Gain
Normal Operations	2.5	3.05	0.2160	4.769	8.3
HPM 1	2.35	3.25	0.3569	4.567	4.7
HPM 2	2.4	3.15	0.3713	4.567	5.6
HPM 3	2.45	3.0	0.4006	4.683	7.8
HPM 4	2.5	3.05	0.2219	4.767	8.3

After isolated HPM and radiation effects on the VTC were analyzed, combinatory effects on the device VTC were studied. The inverter state, dose rate, and frequency of the HPM signal all factored into the VTC response. Figure 21 illustrates the time varying VTC response to combined radiation and HPM for a high input, at the maximum dose rate (73 krad(tissue)/hr).

The VTC response appears to be a superposition of the isolated HPM and ionizing radiation effects. The gamma radiation shifts the VTC and reduces the max output for HI case, while the HPM flattens the VTC curve. Time varying response

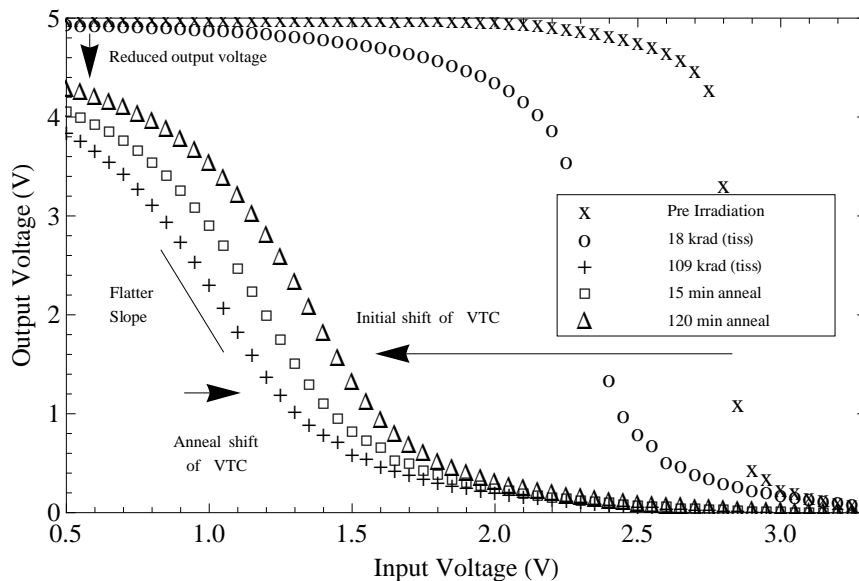


**Figure 21. VTC effects for combined HPM and ionizing high input state condition on an A inverter. The dose rate was 73 krad(tissue)/hr and was irradiated for a total dose of 109 krad(tissue). A 500 kHz 26 dBm signal was injected into the inverter during each measurement.**

for the VTC shifting matches the previous ionizing radiation experiments. Clearly, the combined effects distort the VTC more than the HPM and gamma radiation independently.

Figures 22, 23, and 24 present all A inverter experiments after 18 krad(tissue), 109 krad(tissue), and 90 minutes recovery. All experiments described in Subsubsection 4.3.1.2 are presented in the chronological order. Further details regarding the cause of the VTC distortion are covered in Subsubsections 4.3.2.1 through 4.3.2.5.

#### **4.3.1.3 B Inverters and the VTC Response.**

The B inverters were also examined for isolated HPM, gamma, and combined effects. In an effort to incite additional ionizing effects, irradiation was extended from 90 minutes to 120 minutes, thereby increasing the total dose from 109 krad(tissue) to 146 krad(tissue). Even with the extended irradiation, the results were negligible. There was no significant shift identified during any B inverter experiment during or

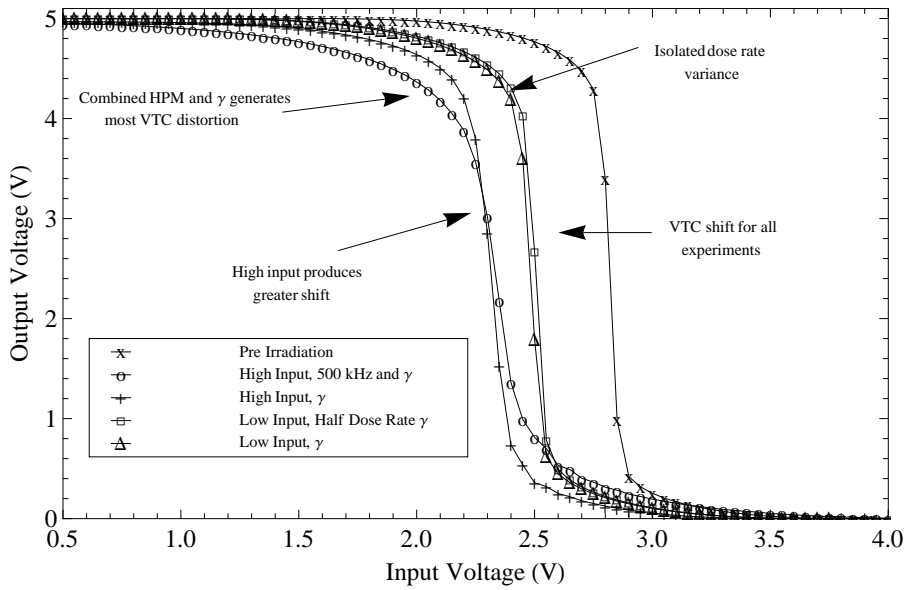


Figure 22. VTC response for all A inverter experiments during 15 minutes of irradiation. 73 krad(tissue)/hr and 36 krad(tissue)/hr (labeled as half dose rate) were selected. For the HPM and combined experiments, a 500 kHz 26 dBm was injected into the device.

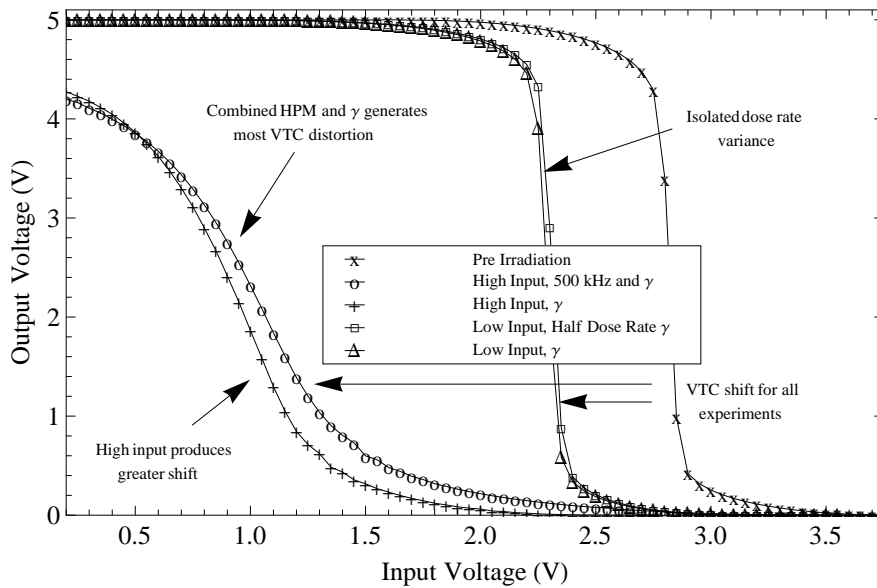
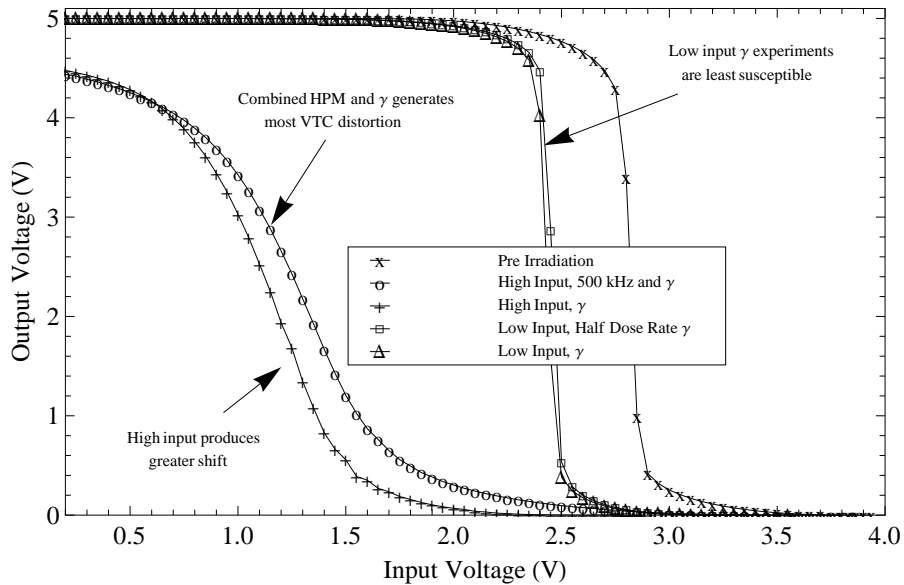


Figure 23. VTC response for all A inverter experiments during 90 minutes of irradiation. 73 krad(tissue)/hr and 36 krad(tissue)/hr (labeled as half dose rate) were selected. For the HPM and combined experiments, a 500 kHz 26 dBm was injected into the device.



**Figure 24.** VTC response for all A inverter experiments after 90 minutes of annealing. 73 krad(tissue)/hr and 36 krad(tissue)/hr (labeled as half dose rate) were selected. For the HPM and combined experiments, a 500 kHz 26 dBm was injected into the device.

after irradiation. The state of the inverter, either low or high input, produced no additional effects to the VTC.

The natural VTC radiation hardness for the B inverters is attributed to the device dimensions. Compared to the A inverters, the device interaction volume is orders of magnitude smaller for the low power inverters. The reduction in device size decreases the energy deposition from the gamma radiation, thus producing fewer EHPs. Further details about the VTC natural hardness of the B inverters is covered in Subsection 4.3.2.

HPM only effects for the B inverters were investigated before proceeding to the combined effects on the VTC. In the case of the advanced low power CMOS inverters, the experimental fixture allowed for efficient propagation of high frequency HPM signals. Frequency was the only parameter adjusted for the injected HPM signals. The selected HPM signals for B inverters had the following signal parameters.

- HPM 1  $\Rightarrow$  1 GHz 26 dBm CW signal

- HPM 2  $\Rightarrow$  850 MHz 26 dBm CW signal
- HPM 3  $\Rightarrow$  1.3 GHz 26 dBm CW signal

All signals were at a power level of 26 dBm (24 dBm is 251.2 mW). At power levels lower than 1 mW, the HPM signals failed to produce any effects on the VTC.

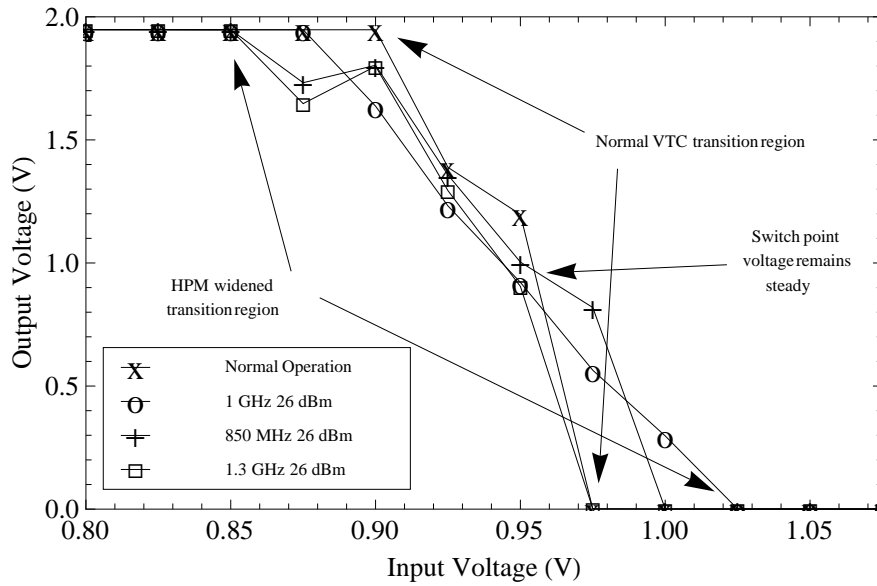


**Figure 25.** VTC response due to various HPM signals on a B inverter. All HPM CW signals had 26 dBm power.

Figure 25 displays the VTC data for the low power CMOS inverters. Similar to the hex inverters, the switching region widened with the addition of the HPM signal. The effects on the maximum and minimum input and output voltages ( $V_{IH}$ ,  $V_{IL}$ ,  $V_{OH}$ , and  $V_{OL}$ ) for the inverter degraded the device gain. Each HPM signal significantly disrupted the inverter. However, the 1 GHz signal produced the greatest effect on the VTC plot. For the 1 GHz HPM injection, the gain dropped from 26.0 to 13.0, or nearly half its original value. The strong response of the inverter to the 1 GHz signal, the device resonant frequency, matched the results found during the VNA measurements discussed in Section 4.2.



Unlike the distorted noise margins, the B inverter switching voltage remained steady at 0.95 V, regardless of HPM injection. Once again, the stagnant  $V_{sp}$  in the presence of an HPM upset suggested the shifting of the VTC depended on ionizing radiation. The VTC effects, based on frequency dependent HPM signals, are shown in Table 9.

**Table 9. Comparison of normal operation and HPM effects for VTC on a B Inverter. Corresponding voltages relate to device gain.**

HPM Conditions	$V_{IL}$ (V)	$V_{IH}$ (V)	$V_{OL}$ (V)	$V_{OH}$ (V)	Gain
Normal Operations	0.900	0.975	0.742	1.947	26.0
HPM 1	0.875	1.025	0.751	1.947	13.0
HPM 2	0.850	1.000	0.879	1.947	13.0
HPM 3	0.850	0.975	1.66	1.947	15.6

When HPM coupling and gamma irradiation were combined, results once again demonstrated a superposition of the isolated effects on the VTC. The time varying VTC in Figure 26 presented a B inverter at high input state with a maximum ionizing dose rate (73 krad(tissue)/hr), coupled with a 1 GHz 26 dBm HPM signal. As presented in Figure 26, the normal VTC behavior deteriorated further with the addition of the HPM signal. The VTC, with the coupled HPM, maintained its shape and position throughout the radiation process. The lack of change demonstrates that the HPM distortion, not the gamma radiation, affected the VTC for the B inverter. The VTC responded similarly, regardless of inverter state condition, dose rate, or HPM characteristics. Further details covering device parameters, which play a role in VTC production, is covered in Subsection 4.3.2.

#### 4.3.1.4 Radiation Effects on CTC.

CTC characteristics relate to the VTC, but illustrate the current and power capabilities of the CMOS inverter. Section 2.3 described the formulation of the CTC,

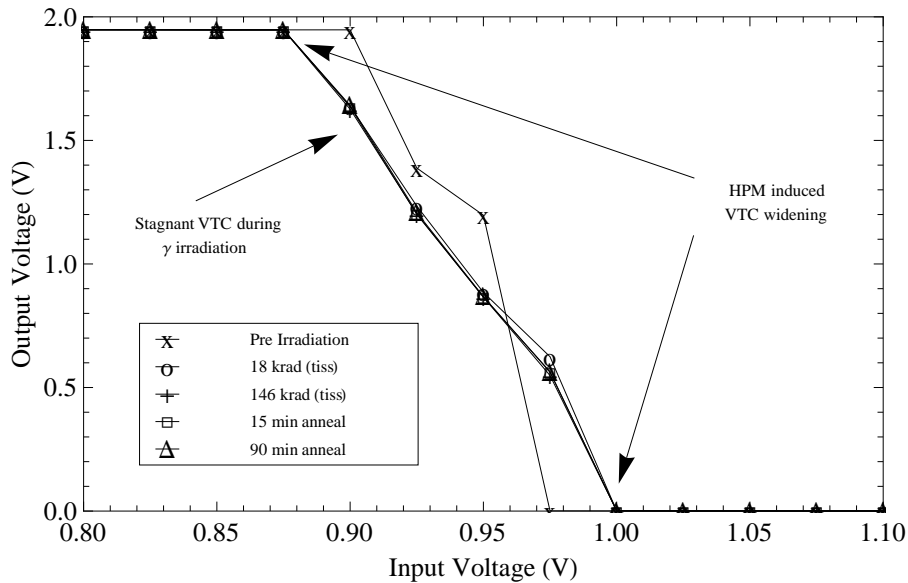


**Figure 26.** VTC effects for combined HPM and ionizing high input state condition on a B inverter. The dose rate was 73 krad(tissue)/hr and was irradiated for a total dose of 146 krad(tissue). A 1 GHz 26 dBm signal was injected into the inverter during each measurement.

emphasizing the benefit of low power consumption of the CMOS design. Different radiation sources, inverter states, and dose rates impact the CTC shape and magnitude at various times during the experiments.

#### 4.3.1.5 A Inverters and the CTC Response.

CTC effects due to HPM and ionizing radiation were studied for A inverters. The time varying CTC plot in Figure 27 displays the effects due to a low input inverter state with the gamma radiation at the maximum dose rate (73 krad(tissue)/hr). After a total dose of 18 krad(tissue), the CTC not only shifted to a lower voltage on the input voltage scale, but increased in peak magnitude. The center of the CTC plot continued to shift until the device was removed from the gamma source. After approximately dose of 19 krad(tissue), the maximum CTC peak began to reduce substantially, and continued after irradiation. By the end of the measurement, the width of the CTC region reduced by 20% while the maximum current value transitioned from 397  $\mu$ A,

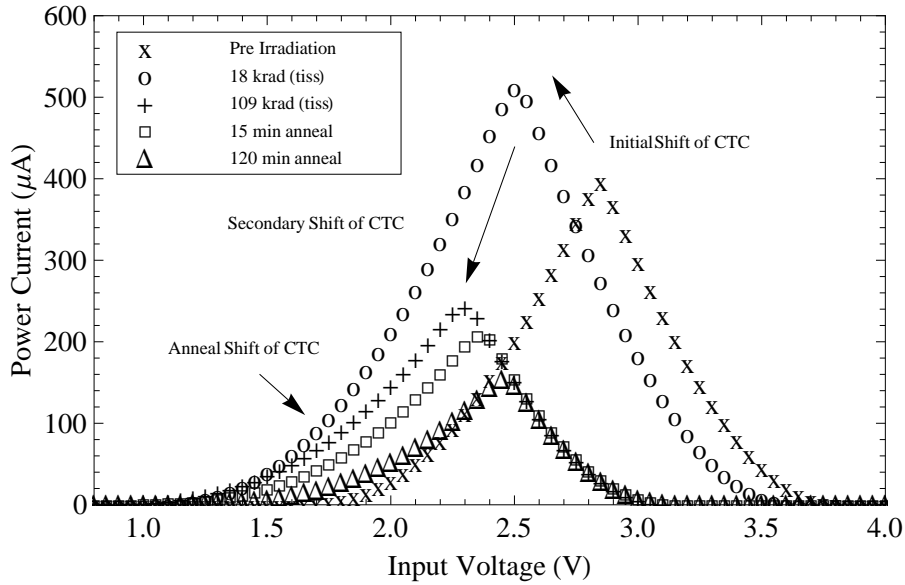


**Figure 27.** CTC effects for ionizing only low input state condition on an A inverter. The dose rate was 73 krad(tissue)/hr and was irradiated for a total dose of 109 krad(tissue).

to 511  $\mu\text{A}$  at 19 krad(tissue) (29% increase), to 153  $\mu\text{A}$  after two hours of room temperature annealing (70% decrease).

Additional CTC effects were identified when attention was focused on the leakage current region. As seen in Figure 28, the leakage current rose remarkably during ionizing radiation. The normal operation leakage current for an A inverter is in the  $n\text{A}$  range. The leakage current rose continuously as the total dose increased. At the end of irradiation, the leakage current increased two orders of magnitude. Furthermore, the CTC also transitioned from the saturation to conduction current region at lower input voltages. The time dependent shift of the current transition region correlates with the shifting of the VTC described in Subsubsection 4.3.1.2. Additional leakage current effects are described in Subsubsection 4.3.2.4.

The following experiment, shown in Figure 29, maintained all experimental parameters, with the exception of changing the input state condition to a high input ( $V_{DD}$ ). The difference in CTC response as shown in Figure 29 proves the sensitivity to the inverter state during gamma irradiation. After a total dose of 18 krad(tissue),

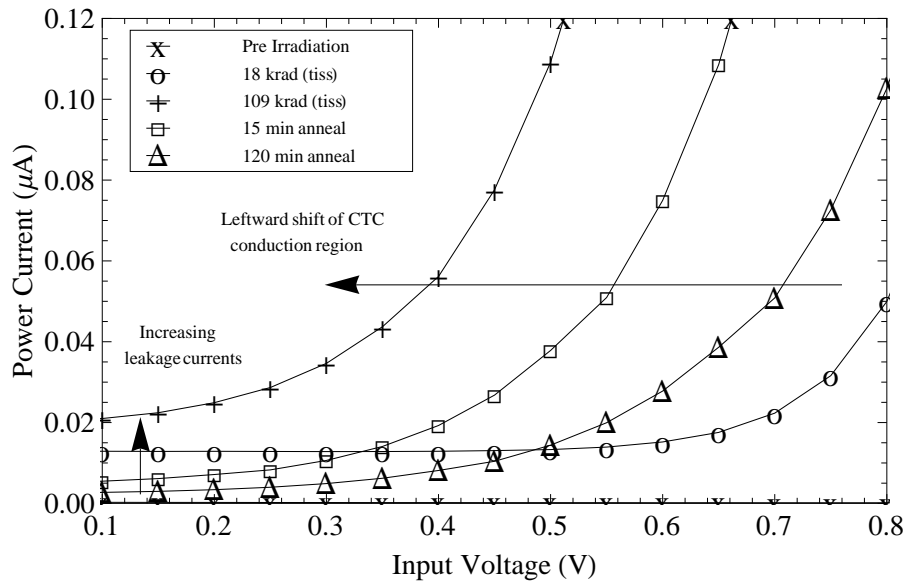


**Figure 28.** Leakage current effects for ionizing only low input state condition on an A inverter. The dose rate was 73 krad(tissue)/hr and was irradiated for a total dose of 109 krad(tissue).

the CTC center point shifted negative and increased in  $I_{max}$ . In fact, at this dose both low and high input conditions provided the same result. The high input CTC center point was only 0.2 V more negative than the low input experiment and had only 20% variance in maximum current.

The CTC response for the high input condition continued to shift and increase in current. By the end of the irradiation, half of the CTC conduction region was beyond the range of the experimental apparatus. The maximum current peak reached 650  $\mu A$ , or a 64% increase.

A closer investigation revealed a distortion of the normally symmetric shape of the CTC during irradiation. With increased dose, the boundaries of the CTC plot, which represented the leakage current, began to increase significantly. The distinct bell shape of the CTC plot flattened out with increased dose. After irradiation, the now flat CTC peak region began to subside. By the end of the experiment, an input of 0 V generated a current of 450  $\mu A$ , 14% increase from the normal maximum

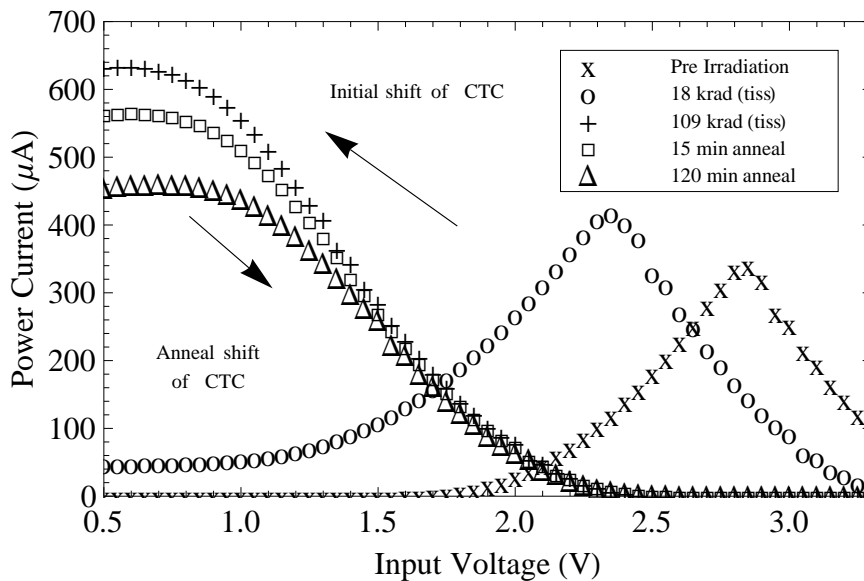


**Figure 29.** CTC effects for ionizing only high input state condition on an A inverter. The dose rate was 73 krad(tissue)/hr and was irradiated for a total dose of 109 krad(tissue).

current peak. The change in inverter state not only shifted the CTC more severely, but distorted the shape of the CTC and maximum peak. Figure 30 illustrates the differences between the CTC response for low and high input inverter states.

Two separate experiments were conducted in which the dose rates were different; 73 krad(tissue)/hr and 37 krad(tissue)/hr. The CTC response for each experiment appeared congruent in their magnitudes and time varying responses. The two experiments, an ionizing radiation only with low input inverter state, measured approximately the same input voltages that correspond to the transition regions between leakage to conduction currents. Only one parameter, the leakage current magnitude, showed sufficient change during the two experiments. With the lower dose rate, the leakage current increased, to the extent observed with a 73 krad(tissue)/hr dose rate. Otherwise, the dose rate difference produced little difference in CTC responses.

HPM only experiments were conducted on the A inverters. Only time invariant tests were completed for isolated HPM effects. Four HPM frequencies were chosen

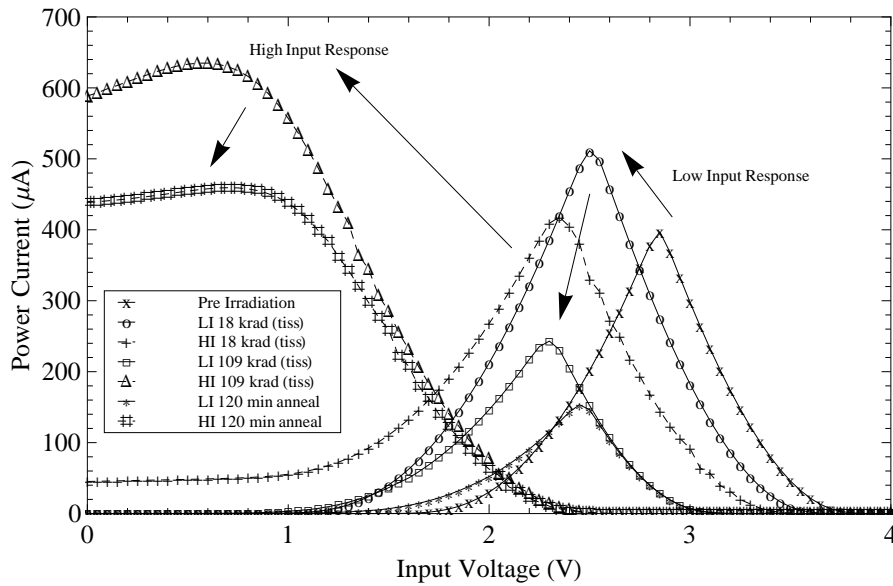


**Figure 30. CTC effects for ionizing only irradiation on an A inverter. Both the low and high input state condition effects are shown for a dose rate of 73 krad(tissue)/hr and total dose of 109 krad(tissue).**

based on the VNA measurements. All HPM signals were characterized with a power level of 26 dBm. To reiterate, the frequencies involved in the A inverter HPM experiments were as follows.

- HPM 1  $\Rightarrow$  250 kHz 26 dBm CW signal
- HPM 2  $\Rightarrow$  500 kHz 26 dBm CW signal
- HPM 3  $\Rightarrow$  10 MHz 26 dBm CW signal
- HPM 4  $\Rightarrow$  250 MHz 26 dBm CW signal

Similar to the VTC effects described in Subsubsection 4.3.1.2, the HPM affected the CTC. As shown in Figure 31, the current conduction of the inverter increased at the apex, correlating to an increased maximum current peak. Additionally, the width and leakage region of the CTC increased substantially. Significant current conduction occurs only when both the NMOS and PMOS devices are within the saturation region.

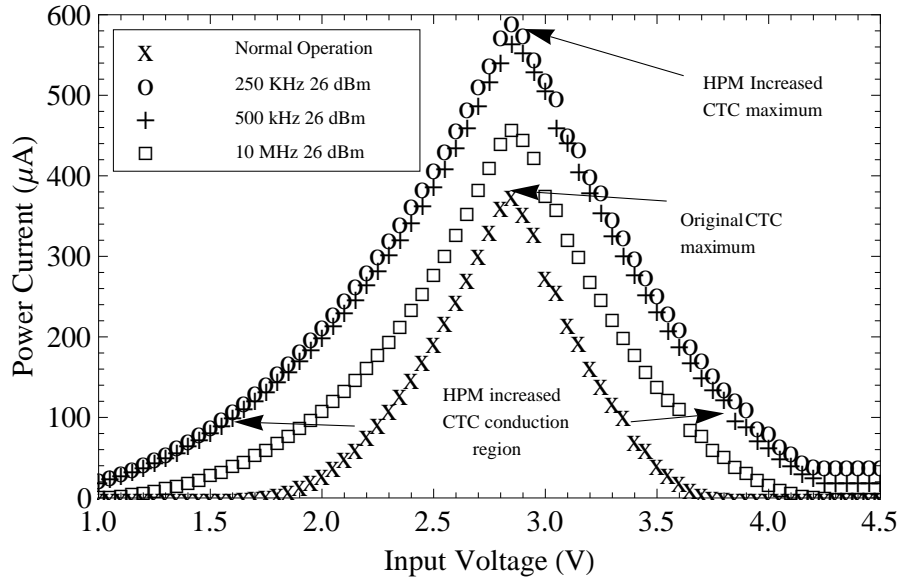


**Figure 31.** CTC response due to various HPM signals on an A inverter. All HPM CW signals had 26 dBm power.

In essence, the HPM produced signal distortions on the transistor gates, forcing each device to transition more frequently in the triode or saturation current regions (shown in Equations 13 through 16).

At the ideal operating voltages, 0 or  $V_{DD}$ , only leakage currents should exist. Under normal operating conditions, the leakage current was in the  $nA$  range. But with the addition of an HPM signal, the leakage current rose about an order of magnitude for frequencies in the  $kHz$  range. A magnified view of the effects on CTC leakage region is provided in Figure 32.

Further investigation revealed a relationship between frequency and magnitude of distortion in the CTC. As the frequency of the HPM signal decreased, the current leakage increased. The inverse relationship between HPM frequency and CTC change was attributed to the time spent in the dual saturation region, when current conduction was at a maximum. In the worst case, the coupled 250 kHz HPM signal amplified the maximum current peak from  $376 \mu A$  to  $592 \mu A$  (57% increase) and leakage current by more than three orders of magnitude. The maximum peak and

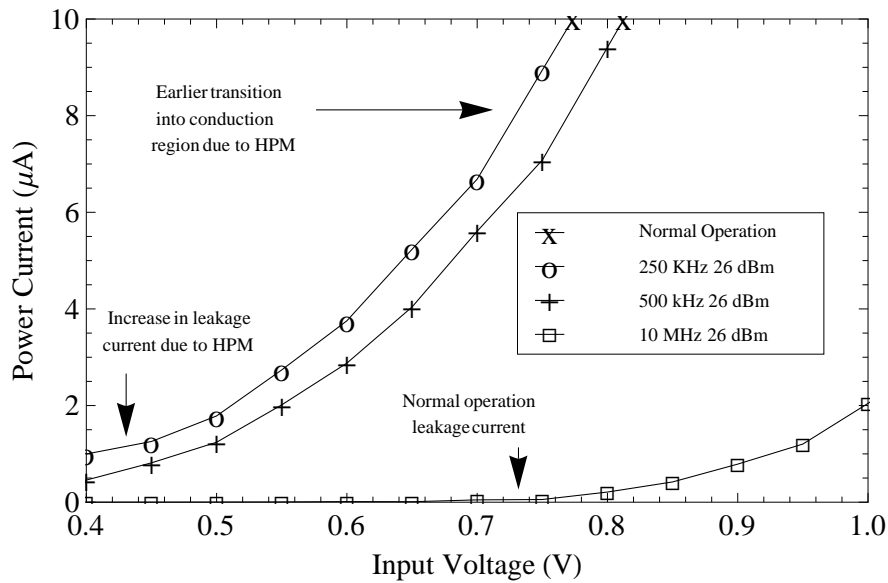


**Figure 32.** Leakage current response due to various HPM signals on an A inverter. All HPM CW signals had 26 dBm power.

leakage current levels for corresponding HPM conditions are presented in Table 10.

**Table 10.** Comparison of normal operation and HPM effects for CTC on an A Inverter.

HPM Conditions	$I_{max}$ ( $\mu A$ )	$I_{leakage}$ ( $nA$ )
Normal Operations	376.9	0.9
HPM 1	591.9	1500
HPM 2	566.2	1000
HPM 3	458.2	83
HPM 4	380.8	0.7

After the isolated radiation environments were investigated, combined HPM and gamma radiation effects experiments were conducted. Various experiments examined the change in CTC effects for various critical parameters, to include HPM frequency, dose rate, and inverter state conditions. For instance, Figure 33 demonstrates the time varying effects on the CTC due to a combined radiation environment. An HPM signal of 500 kHz 26 dBm signal was coupled into the inverter during gamma irradiation at the maximum dose rate.



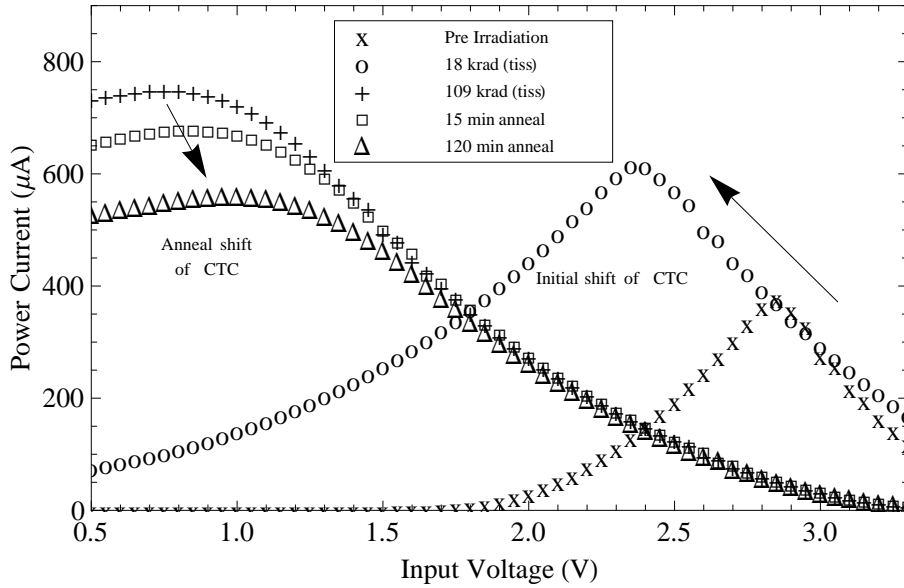


**Figure 33.** CTC effects for combined HPM and ionizing high input state condition on an A inverter. The dose rate was 73 krad(tissue)/hr and was irradiated for a total dose of 109 krad(tissue). A 500 kHz 26 dBm signal was injected into the inverter during each measurement.

The results show the CTC combined radiation response is an accumulation of the effects identified in the isolated radiation experiments. After 18 krad(tissue) total dose, the time varying shift of the CTC center point matched for the combined and ionizing only radiation experiments, to within 0.025 V. Additionally, the CTC effects were greater in maximum peak, width, and leakage current, implying compounded effects from HPM and ionizing radiation.

As total dose exceeded 18 krad(tissue), CTC integrity of the combined radiation experiment declined at an accelerated rate. The CTC shape progressively flattened out, and the excessive shifting of the center point exceeded the limits of the inverter sweep. By the end of irradiation, the maximum current raised to 750  $\mu\text{A}$  from 376  $\mu\text{A}$  (99% increase) and half the CTC bell shape extended from 0 to 3.5 V. The remaining half of the CTC was positioned outside the range of the experimental apparatus.

Similar to the VTC experiments, the combined radiation sources influenced the maximum distortion and the inverter functionality. Figures 34, 35 and 36 present the

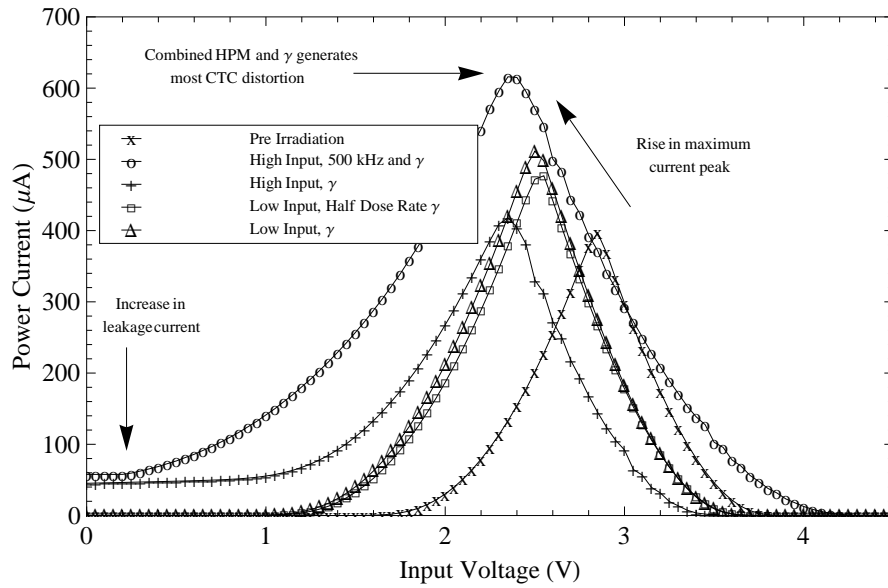


Figure 34. CTC response for all A inverter experiments during 15 minutes of irradiation. 73 krad(tissue)/hr and 36 krad(tissue)/hr (labeled as half dose rate) dose rates were selected. For the HPM and combined experiments, a 500 kHz 26 dBm was injected into the device.

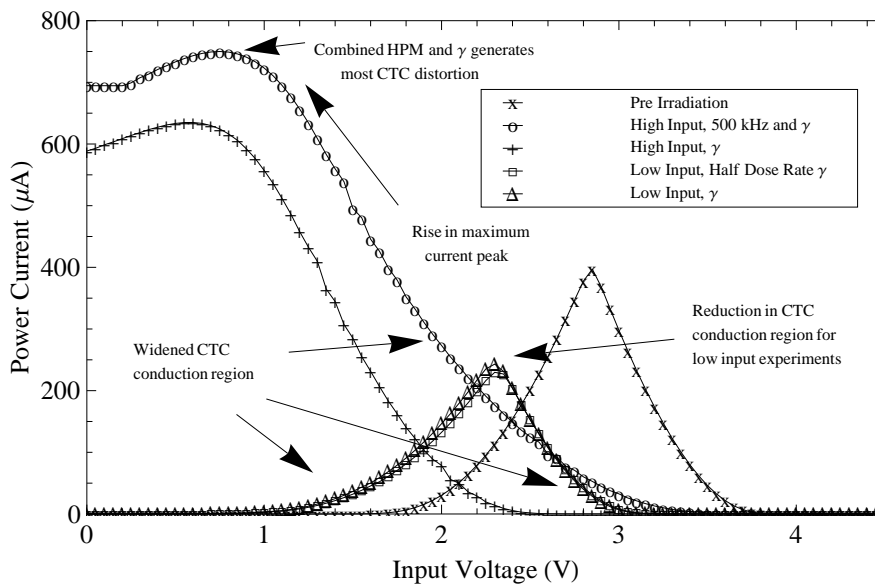
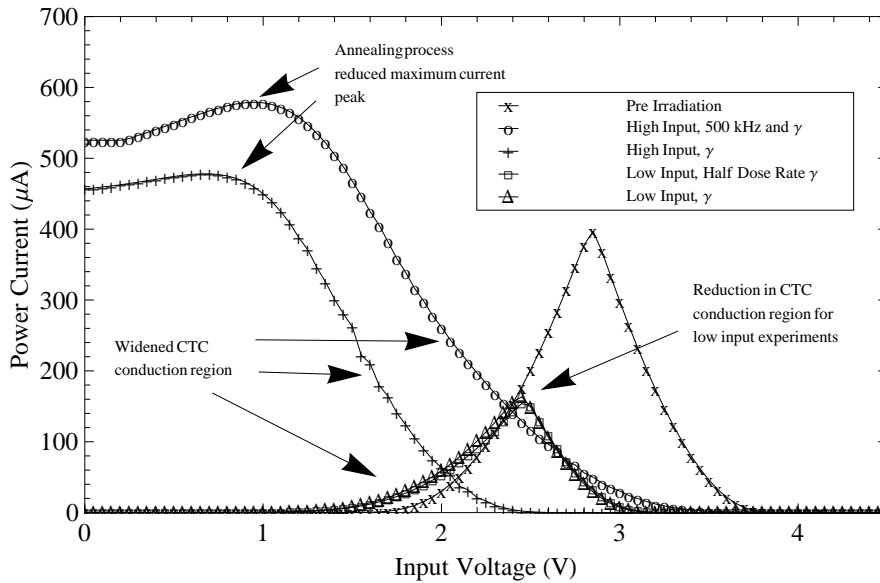


Figure 35. CTC response for all A inverter experiments during 90 minutes of irradiation. 73 krad(tissue)/hr and 36 krad(tissue)/hr (labeled as half dose rate) dose rates were selected. For the HPM and combined experiments, a 500 kHz 26 dBm was injected into the device.



**Figure 36.** CTC response for all A inverter experiments after 90 minutes of annealing. 73 krad(tissue)/hr and 36 krad(tissue)/hr (labeled as half dose rate) dose rates were selected. For the HPM and combined experiments, a 500 kHz 26 dBm was injected into the device.

time varying CTC response for all A inverter experiments. All graphs illustrate the CTC responses, in chronological order, after 18 krad(tissue), 109 krad(tissue), and 90 minutes recovery. Further discussion concerning the nature of the combined radiation environment is provided in the parameter Subsubsections 4.3.2.1 through 4.3.2.5.

#### 4.3.1.6 B Inverters and the CTC Response.

The experiments conducted for the A inverters were then used to determine the CTC effects for the B inverters. Isolated HPM, gamma, and the combination effects on the CTC were analyzed for the B inverters. As presented in the Subsubection 4.3.1.5, the irradiation was extended to a total dose of 146 krad(tissue). The experiments included 90 minutes of post irradiation annealing. During the ionizing radiation experiments, the CTC effects were minimal. The CTC apex location, maximum current output, and width of the conduction region remained stable during the full irradiation period. Like the VTC plots, the B inverters demonstrated a strong

tolerance to ionizing radiation. The size of the inverter interaction area and thickness of the oxide diminished the susceptibility to ionizing radiation.

The CTC leakage current region revealed significant change when compared to the normal operation leakage current. As seen in Figure 37, the magnitude of the leakage current rose significantly as the dose increased. By the end of irradiation, the leakage current for the low input case increased from 9 nA to over 1  $\mu$ A, or by nearly three orders of magnitude. During annealing, the leakage current dropped to 0.47  $\mu$ A. The absence of gamma radiation interrupted EHP generation, leading to the reduction in leakage current.

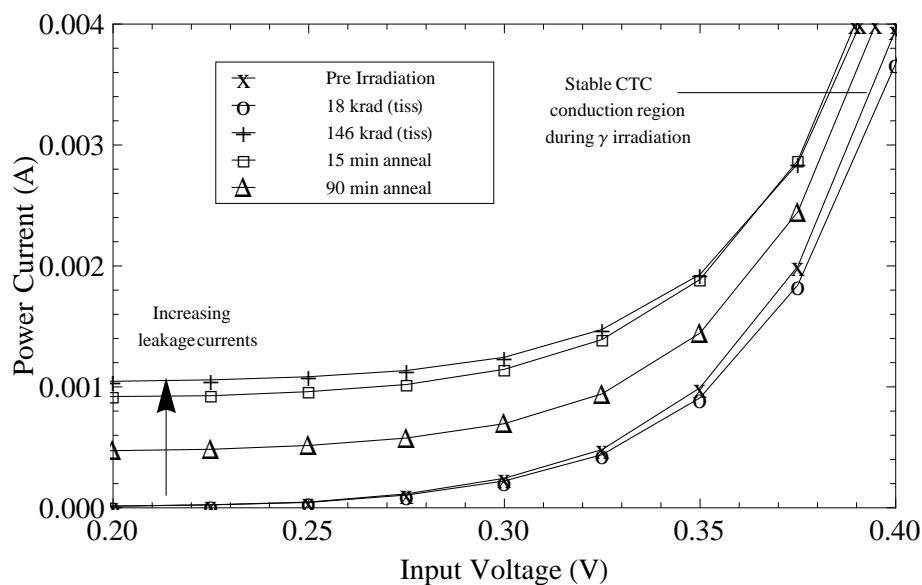


**Figure 37. Leakage current effects for ionizing only low input state condition on a B inverter. The dose rate was 73 krad(tissue)/hr and was irradiated for a total dose of 146 krad(tissue).**

The high input test case generated even more substantial leakage current. At the end of irradiation, the leakage current reached 50  $\mu$ A, or roughly a four order of magnitude increase. The electric field across the oxide dramatically decreased EHP recombination, leading to additional carriers in the substrate. Additional leakage current results are presented in Subsubsection 4.3.2.4.

After the ionizing radiation only effects were studied, isolated HPM experiments were conducted. Three HPM signals, all at 26 dBm power level, were coupled into the input port of the low power inverters. The PCB design of the experimental apparatus for the B inverters allowed for efficient transmission of high frequency signals. Therefore, the HPM frequencies were selected based on the resonant frequencies measured in the VNA experiments. The three frequencies for the B inverter tests were as follows.

- HPM 1  $\Rightarrow$  1 GHz 26 dBm CW signal
- HPM 2  $\Rightarrow$  850 MHz 26 dBm CW signal
- HPM 3  $\Rightarrow$  1.3 GHz 26 dBm CW signal

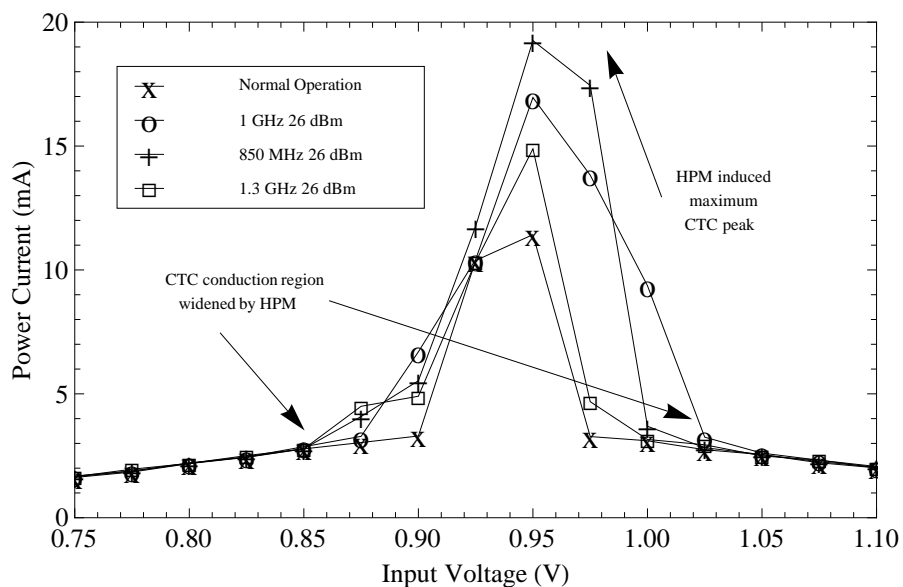


**Figure 38.** CTC response due to various HPM signals on a B inverter. All HPM CW signals had 26 dBm power.

The CTC inverter response to various HPM signals is displayed in Figure 38. As shown, the addition of the HPM signals increased the current peaks. The 850 MHz HPM signal elicited the most extreme response, raising  $I_{max}$  from 11.4 mA to 19.2 mA,

or an increase of 68%. The B inverters, similar to the A inverters, established a relationship between HPM frequency and inverter effects.

**Table 11. Comparison of normal operation and HPM effects for CTC on an B Inverter.**

HPM Conditions	$I_{max}$ (mA)	$I_{leakage}$ (nA)
Normal Operations	11.4	3.6
HPM 1	16.9	9.2
HPM 2	19.3	4.1
HPM 3	14.9	5.2

The leakage current effects of the B inverters were not as pronounced as the A inverters, showing only a 157% rise in leakage. However, the coupled HPM distortion accelerated the transition rate from leakage to the active region in the transistors. The coupled HPM caused a premature entry into the active transistor state. The addition of HPM interference prompted a shift in voltage at which the transistors transformed from an open (leakage current only) to closed (strong current conduction) state. From figure 39, it was apparent that the threshold voltage, which controlled the current transition region, shifted 0.05 V, leading to a untimely current rise. The CTC shift ties directly to the stagnant offset shift discussed in Subsubsection 4.3.1.3. The CTC effects due to various HPM signals are presented in Table 11.

Figure 40 displays the CTC time varying response for a high input state condition under a combined radiation exposure. Compared to the normal environmental conditions, the CTC widened and increased in maximum current. The width of the current conduction region expanded from 0.07 V to 0.18 V, or a 157% magnification. Also, the CTC was constant during irradiation, meaning there were no time varying effects.

The isolated HPM experiments produced the same qualitative effects on the CTC conduction region.  $I_{max}$  initially increased from 11.42 mA to 13.7 mA during the first measurement. As the experiment continued, the maximum current peak centered at

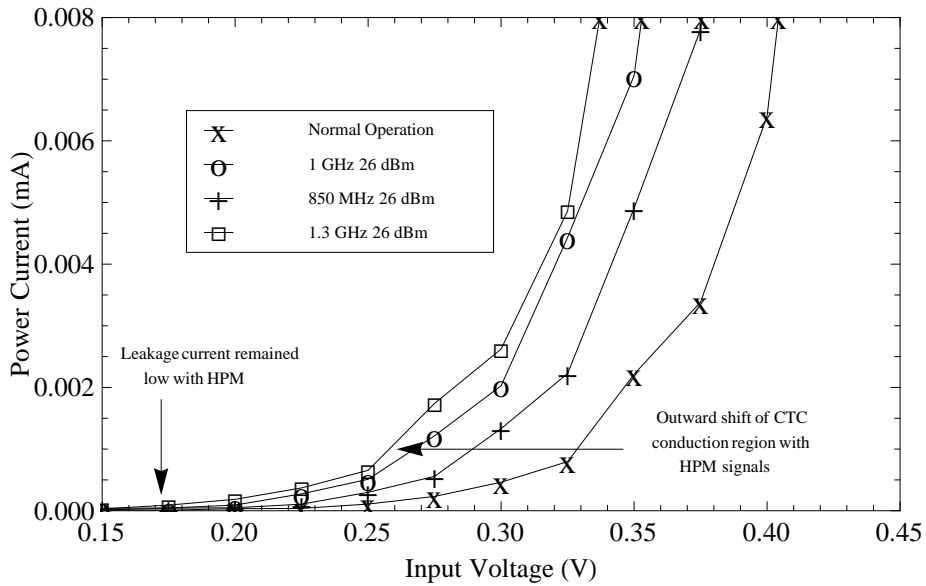


Figure 39. Leakage current response due to various HPM signals on a B inverter. All HPM CW signals had 26 dBm power.

13.6 mA, with a 0.4 mA maximum offset. Due to the time invariance for the CTC width and  $I_{max}$ , the HPM radiation is the dominant factor in CTC distortion.

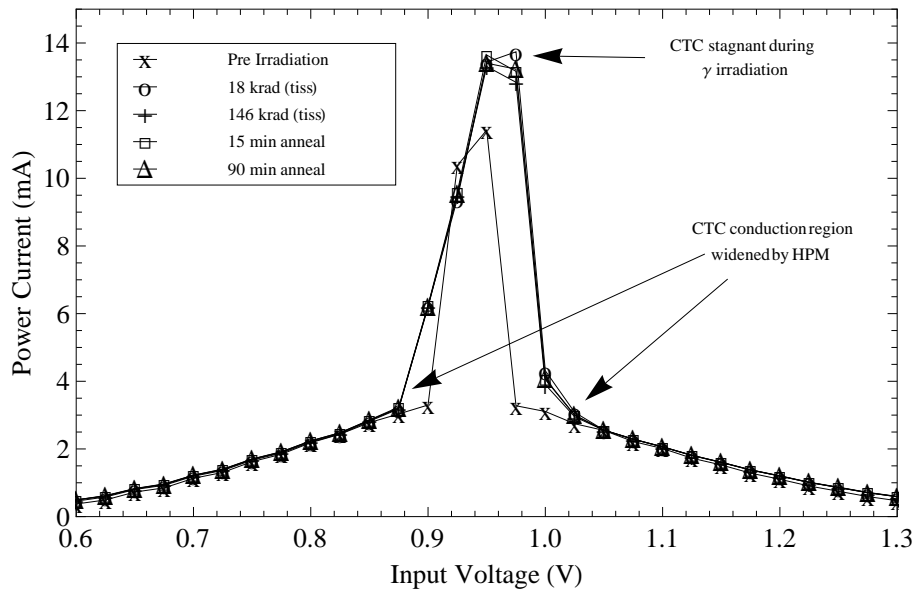
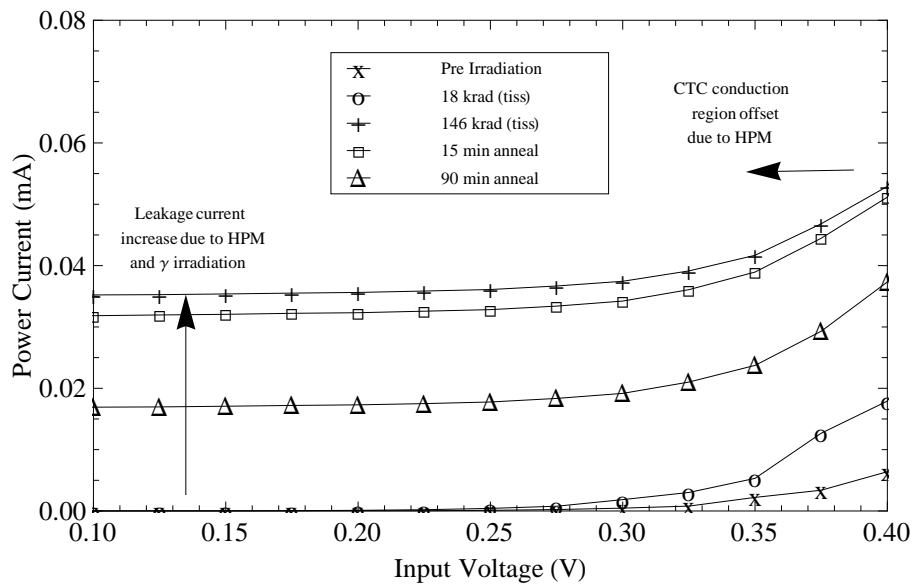


Figure 40. CTC effects for combined HPM and ionizing high input state condition on a B inverter. The dose rate was 73 krad(tissue)/hr and was irradiated for a total dose of 146 krad(tissue). A 1 GHz 26 dBm signal was injected into the inverter during each measurement.

The leakage current response validated a contributing effect by the ionizing radiation source. As the dose increased, the leakage current increased. After 146 krad(tissue), the leakage current rose by more than four orders of magnitude, expanding from 3 nA to 34  $\mu$ A. During 90 minutes of annealing, the leakage current dropped to 16  $\mu$ A.



**Figure 41. Leakage current effects for combined HPM and ionizing high input state condition on a B inverter. The dose rate was 73 krad(tissue)/hr and was irradiated for a total dose of 146 krad(tissue). A 1 GHz 26 dBm signal was injected into the inverter during each measurement.**

The measured CTC effects were an addition of the independent radiation source effects. It was clear that a simultaneous radiation environment influenced the most extreme inverter CTC change. Details into the parameters driving the CTC effects are covered in Subsections 4.3.2.1 through 4.3.2.5.

### 4.3.2 Radiation Effects on Device Parameters.

Subsubsections 4.3.1.1 and 4.3.1.4 discuss inverter parameter effects due to HPM and gamma radiation. Combined HPM and ionizing effects are studied for each inverter parameter. The device parameters, all of which contribute to the VTC and



CTC solutions, are presented below.

#### 4.3.2.1 Radiation Effects on Threshold Voltages.

Due to the proprietary information, threshold voltages were not provided in the product specification. Instead, threshold voltages were measured based on basic transistor definitions. The threshold voltage represents the point at which sufficient mobile charges accumulate in the substrate to form a conduction channel. The point at which the current exponentially rises from a steady leakage current identifies the threshold voltage. For a CMOS inverter, there is a threshold voltage for the NMOS and PMOS transistors.

The threshold voltage was determined by calculating the derivative of the current at each increment of the input voltage sweep. Then, the input voltage which corresponds to the predetermined current slope represents the threshold voltages for each time interval measurement. The systematic approach for isolating the  $V_{th}$  ensured an accurate account of the relative change due to HPM and ionizing radiation. Threshold voltages for both A and B inverters were identified in the method presented above.

Figures 42 and 43 illustrate the time dependent threshold voltage shift for the A inverter NMOS and PMOS transistors. Each graph includes various radiation conditions, dose rates, and inverter state conditions.

In all but one case, the threshold voltages for the NMOS and PMOS shifted in the negative direction. A negative shift translates to a reduction in  $V_{th}$ . The more mobile electrons are quickly dispersed after the generation of EHPs, abandoning the positively charged mobile holes. The newly formed positive charges in the oxide, abiding by the CTRW dispersion model, correspond to the relative negative shift in the threshold voltages for both NMOS and PMOS devices. For the PMOS transistor, the negative shifting continued until the inverter was removed from the  $^{60}\text{Co}$  source.

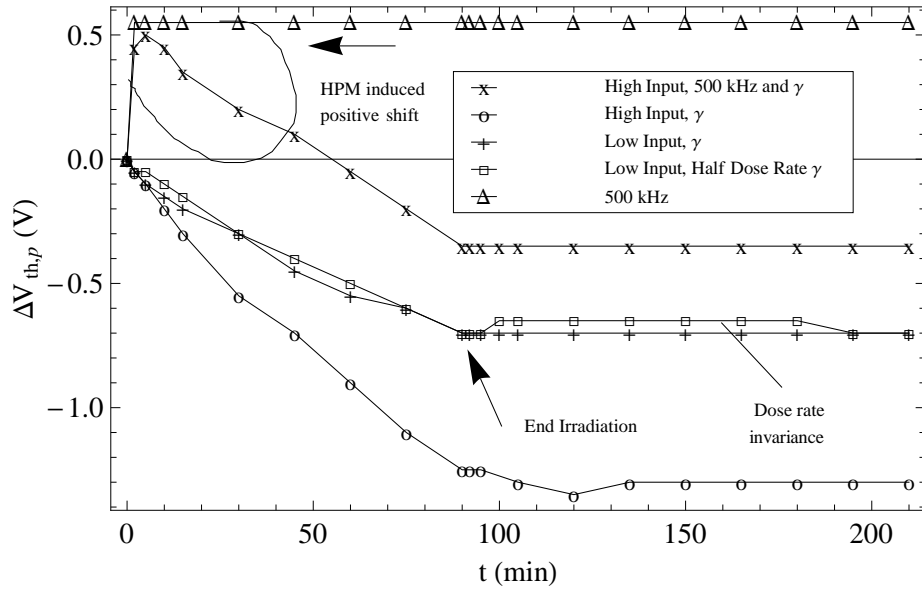


Figure 42. PMOS threshold voltage response for all A inverter experiments. 73 krad(tissue)/hr and 36 krad(tissue)/hr (labeled as half dose rate) dose rates were selected. For the HPM and combined experiments, a 500 kHz 26 dBm was injected into the device.

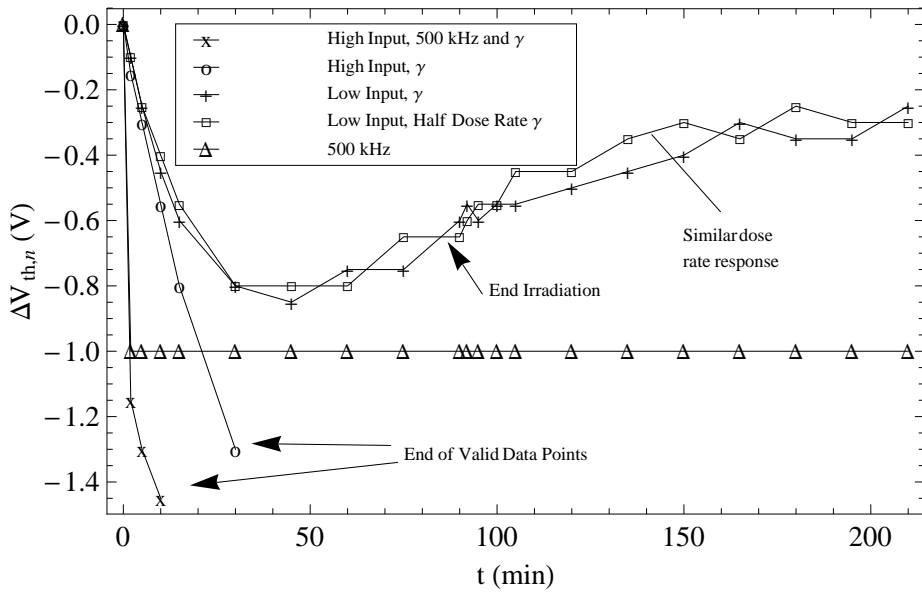
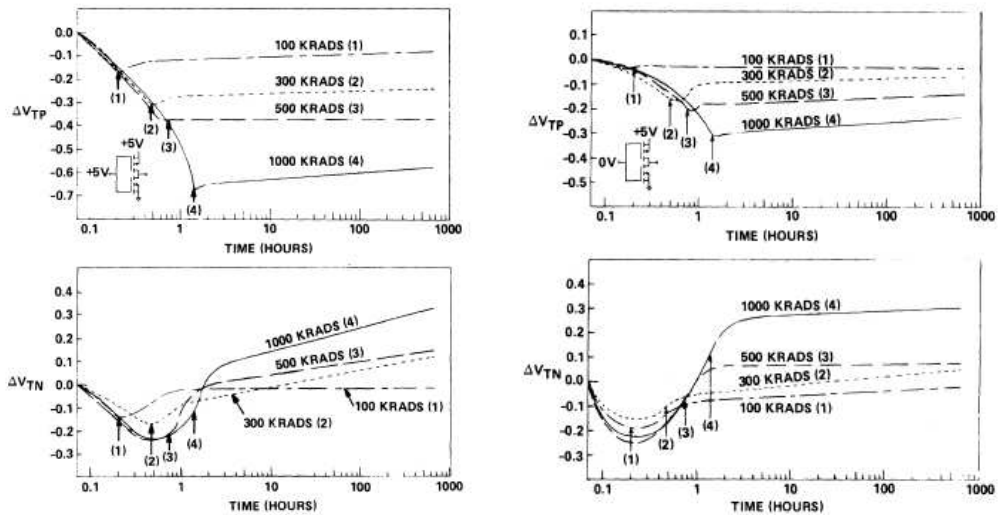


Figure 43. NMOS threshold voltage response for all A inverter experiments. 73 krad(tissue)/hr and 36 krad(tissue)/hr (labeled as half dose rate) dose rates were selected. For the HPM and combined experiments, a 500 kHz 26 dBm was injected into the device.

Once removed, the negative shift ended and remained in a stable position.

The threshold shift for the NMOS responded in a different fashion. After a period of 50 minutes, two test cases began to shift back in the positive direction, similar to previous work by Brucker, shown in Figure 44 [9]. Unlike the PMOS device, the negatively charged interface states,  $N_{it}$ , begin to overcome the positively charged oxide traps,  $N_{ot}$ , thereby shifting the NMOS threshold voltage more positive. The measurement process ended after three hours, but the positive shift is expected and may lead to an overall positive threshold shift. The positive shift after the initial negative drop signifies the rebound effect identified in previous work, as discussed in Subsection 2.2.3 [9], [8].



(a) High Input Threshold Voltage shift. (b) Low Input Threshold Voltage shift.

**Figure 44.** Observed shift in  $V_{Tp}$  and  $V_{Tn}$  conducted by Brucker et al. using a sample of 17 CD4069 hex inverters obtained from a single wafer. Inverter sets, indicated in parentheses, are exposed to different doses, in rad  $\text{SiO}_2$ . Arrows indicate end of irradiation and start of annealing [9].

The input state of the inverter significantly altered the magnitude of the threshold voltage shift. With an input high ( $V_{DD}$ ), the initial negative shifting due to the interface states more than doubled for both transistors. As seen in Figure 42, the high input test decreased approximately 1.4 V, compared to the 0.7 V drop for the

low input measurement.

The effects on the NMOS device were even more dramatic. With a high input, the threshold voltage shift exceeded the limits of the voltage sweep for the inverter. Within 45 minutes of irradiation, the high input test case shifted the NMOS threshold voltage by at least 1.7 V. Due to the test constraints, the extent of the threshold shift and verification of possible rebound was unobtainable.

The presence of an electric field diminish the EHP recombination, leading to a larger number of mobile holes. Then, the positive holes drift toward the interface region at a faster rate, once again due to the applied field ( $V_{in} = V_{DD}$ ). Thus, under bias, larger decreases in threshold voltage at lower doses are observed for both transistors.

When the dose rate was reduced in half (36.5 krad(tissue)/hr), a similar pattern emerged with only minor differences. A slower time constant for the hole dispersion, owing to the slower build up of interface traps in the NMOS oxide, emerged as the only discrepancy when compared to the maximum dose rate. Otherwise, the magnitudes of the  $V_{th}$  shifts for both transistors were similar to within 0.05 V.

When a HPM signal was injected into the A inverter, threshold voltage response was altered for the NMOS and PMOS devices. The combination of ionizing and HPM radiation prompted a two stage reaction. First, the HPM signal created a stagnant offset for the NMOS and PMOS transistors. For the PMOS device, the HPM generated an offset of 0.7 V. A negative offset of approximately 1.0 V displaced the NMOS threshold voltage due to HPM effects.

The injected HPM radiation, essentially a distorted signal modulated to the steady input voltage, provided an additional bias which transitioned each device from a leakage state to full conduction. The shifting of the current transition voltage manifested itself as a stagnant threshold voltage shift. The HPM induced threshold voltage shift

related to the widening of the CTC plot, described in Subsubsection 4.3.1.4.

The second stage of the combined radiation test incorporated isolated ionizing effects described at the beginning of Subsubsection 4.3.2.1. The positively charged mobile holes, providing the initial negative shift for NMOS and PMOS devices, dispersed by the CTRW model. As expected, the PMOS threshold shifting remained steady with the removal of the  $^{60}\text{Co}$  source. It is suggested the NMOS will begin to show signs of annealing and rebound during the irradiation period. Unfortunately, the limitations of the inverter sweep once again failed to bound the magnitude of the threshold shift.

With the two stages combined, the result implied a superposition of HPM and ionizing effects on each device. The PMOS transistor  $V_{th}$  shifted positive, then dropped below the relative origin, and converged at a position after irradiation. The final threshold voltage shift was less excessive when compared to an ionizing only test, due to the positive offset of the HPM signal. The NMOS threshold voltage, with the HPM and ionizing effects working in conjunction, amplified the negative shift. Within the first two minutes of irradiation, the NMOS threshold voltage shifted by more than 1.1 V, whereas the shift for ionizing only experiment was 0.15 V.

Isolated HPM injection effects do not include time varying threshold shifts. Instead, the static  $V_{th}$  offset measured from the isolated HPM experiments is shown in Figures 42 and 43.

The low power CMOS inverter threshold voltage response to radiation varied significantly from the 4069 hex inverters. While the A inverters presented clear voltage shifts for the NMOS and PMOS transistors, ionizing radiation prompted no significant response to any B inverter threshold voltages. The largest shift recorded during any isolated ionizing experiment was 0.02 V, which was attributed to uncertainty of ambient noise. The thickness of the oxide ( $t_{ox}$ ) in the B inverters, which is orders of

magnitude smaller than the A inverters, provided the natural high energy radiation hardness for threshold shifting. The energy transfer for the gamma radiation decreases as the thickness decreases, as shown in Equation 7. The direct relationship between  $t_{ox}$  and radiation tolerance allowed the B inverter threshold voltages to remain stable [14].

The combination of HPM and gamma radiation prompted a steady shift of the threshold voltage. For the NMOS transistors, a time invariant negative voltage shift occurred, with an average magnitude of 0.05 V. Similarly, combined experiments shifted the PMOS threshold voltage positive an additional 0.05 V on average. The offset threshold voltage followed the same pattern as the A inverters. Therefore, the only threshold voltage effects identified for the B inverters were attributed to HPM effects.

Lastly, the threshold shifting analysis validated the experimental setup constructed for the CMOS inverter research. Given the approximate total dose range of 82 - 205 krad(SiO<sub>2</sub>) (depending on the experiment), the measured results agree, qualitatively, with those of Bruckner et al as shown in Figures 44(b) and 44(a). The curves for  $\Delta V_{Tp}$  and  $\Delta V_{Tn}$  at the above mentioned dose have the same general shape as those observed by the Bruckner group [9]. Differences likely arise from uncertainty in dose approximations, as well as differences between the devices used by each set of research.

#### **4.3.2.2 Radiation Effects on Switching Point.**

The switch point voltage ( $V_{sp}$ ) for a CMOS inverter, from Subsection 2.3.3, depends on transistor dimensions, transconductance, and threshold voltages. For a matched inverter, the switch point lies halfway between the device power voltage. To maintain robust operation and integrity, the switching voltage must remain relatively stagnant during device operation. Figure 45 displays the results for switch point

shifting for A inverters.

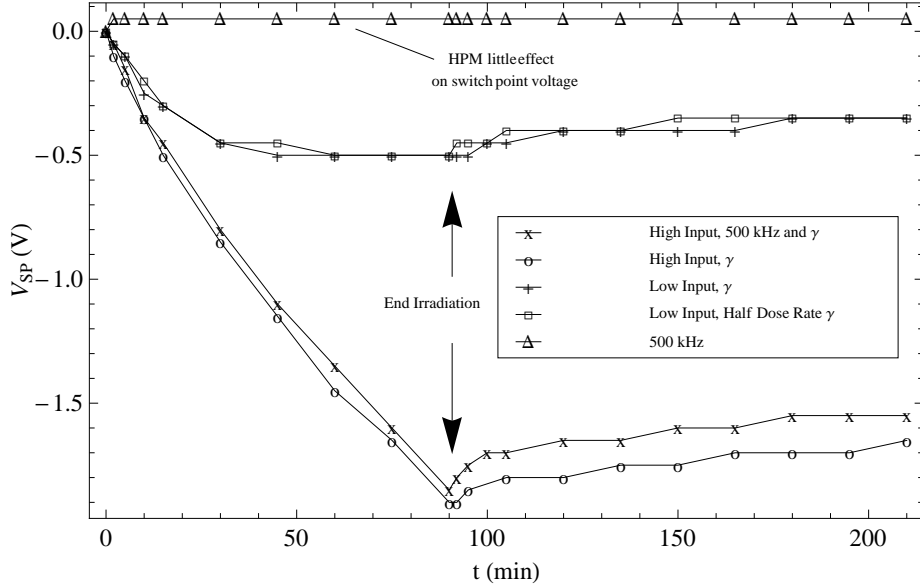


**Figure 45. Switch point voltage response for all A inverter experiments. 73 krad(tissue)/hr and 36 krad(tissue)/hr (labeled as half dose rate) dose rates were selected. For the HPM and combined experiments, a 500 kHz 26 dBm was injected into the device.**

The switching voltage was measured by corresponding an input voltage to half the output voltage ( $V_{out} = V_{DD}/2$ ). At this input voltage, the inverter produces unknown logical states and maximum current dissipation, neither which is indicative of an effective CMOS inverter. The relative shift in  $V_{sp}$  from normal operation was measured at each time interval.

For all tests conducted on A inverters, the switch point shifted negatively by at least 0.5 V. The negative switch point shift relates to the corresponding threshold shifts for the NMOS and PMOS devices, as described in Subsubsection 4.3.2.1. Since both PMOS and NMOS initially respond to ionizing radiation with a negative shift, the switching point followed suit. As a first order approximation, the switch point shift mirrored the response of the threshold voltage shift. A negative shift in  $V_{sp}$  related to the leftward shift of the VTC shown in Subsubsection 4.3.1.1.

Additional experiments were performed to isolate dose rate dependent responses

on the switching voltage. As seen in Figure 45, experiments with a maximum dose rate and half dose rate produced similar responses within measurement error. The shape and magnitude of the  $V_{sp}$  response validated equal reactions for 73 krad(tissue)/hr and 36.5 krad(tissue)/hr dose rates.

The state of the inverter dictated drastic differences in switching voltage response. In the ionizing radiation only cases, a high input state for the inverter shifted the  $V_{sp}$  negatively by 1.9 V, compared to 0.5 V for the low input case. The severity of the high case derives from the presence of an electric field across the oxide. The applied bias not only reduces the number of recombinations from the total EHPs generated, but and provides additional motivation for mobile holes to journey toward the interface traps.

Additionally, the inverter recovery after irradiation depended on the input bias. Without the electric field across the oxide, the inverter annealed more slowly, resulting in a positive shift of 0.15 V within two hours after irradiation. With an applied bias, the annealing process was accelerated, producing a recovery of 0.25 V for the switching voltage. The reversal of the  $V_{sp}$  negative shift during the anneal period coincided with the rightward shift of the VTC, as described in Subsubsection 4.3.1.1. All inverters were expected to continue to anneal over time, slowly shifting more positive toward the original  $V_{sp}$ .

With the addition of the HPM signal, the switching voltage shift behaved similarly to the ionizing radiation only experiments. The shape and time constant of the combined effects illustrated congruent responses, as shown in Figure 45. The only discrepancy in the combined and ionizing only experiments appeared to be the magnitude of the  $V_{sp}$  shift after gamma irradiation. The slight offset, approximately 0.1 V, resulted from augmented annealing from the HPM signal. The HPM signal provided a varying electric field across the oxide, resulting in an increase in  $N_{it}$  detrap-



ping. Thus, the additional HPM signal enhanced the static electric field, increasing the annealing process. Even with the injected HPM signal, the switch point voltage response was primarily an ionizing radiation reaction.

Of the B inverter experiments, only a single measurement presented a  $V_{sp}$  shift of 0.025 V. All other data points signified no change in switching voltage, regardless of radiation conditions. The B inverter natural hardness to voltage shifting of the B inverters confirms two proclamations:

1. The switch point voltage shifting of CMOS inverters is dominated by ionizing radiation
2. The B inverters maintained VTC stability while being irradiated

The  $V_{sp}$  constancy, similar to the threshold voltage, originates from the device dimensions. The thickness of the B inverters, in the low  $nm$  range, restricts the energy transfer for the gamma radiation. Therefore, minimal EHPs are generated to initiate the ionizing radiation effects process.

#### **4.3.2.3 Radiation Effects on Maximum Current.**

The maximum current peak ( $I_{max}$ ), a parameter determined by the strength of conduction by both transistors, provide insight into the device performance under radiation effects. From a CTC plot, the maximum current peak was determined by a current slope of approximately zero. Then, the position and magnitude of  $I_{max}$  was compared to its normal operational value.

The major distinction in the  $I_{max}$  change for the A inverters depended on the input state of the device. The initial response of the inverters resulted in an increase in maximum current. Within the first 15 to 25 minutes of irradiation, as shown in Figure 46, all experiments followed a similar increased response. After a dose of

approximately 19 krad(tissue), all ionizing only experiments were within 23 to 29% increase in maximum current. Then, the inverter reaction diverged based on the device state.

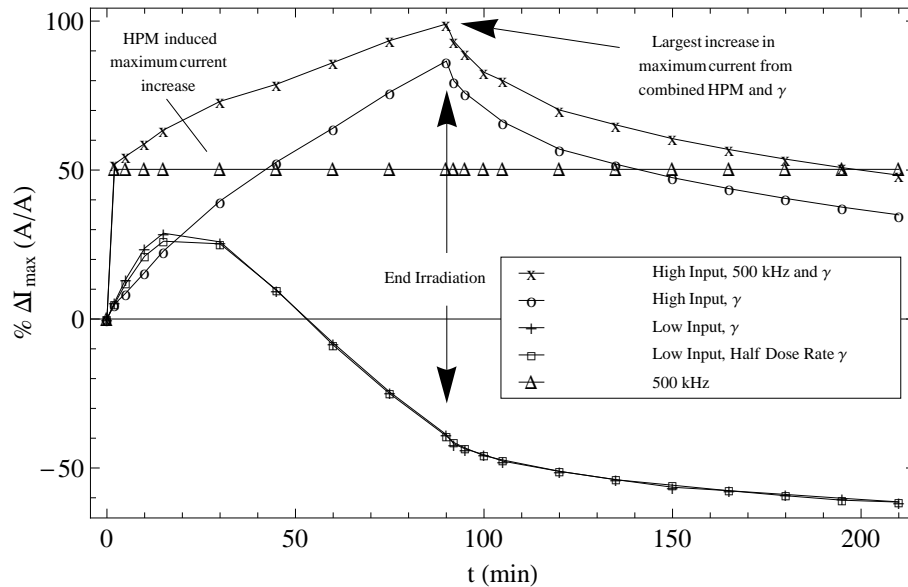


**Figure 46.** Maximum current peak ( $I_{max}$ ) response for all A inverter experiments. 73 krad(tissue)/hr and 36 krad(tissue)/hr (labeled as half dose rate) dose rates were selected. For the HPM and combined experiments, a 500 kHz 26 dBm was injected into the device.

When the device maintained a low input during the measurement, the maximum current peak began to decrease after an approximate dose of 31 krad(tissue).  $I_{max}$  for the low input experiments continued to diminish, eventually reducing by more than 60% of the original peak. Alternatively, a high input state produced a continuous rise with increasing dose. The maximum current peak began to decline during post irradiation annealing.

The low input experiment illustrated an initial accelerated rise, followed by a slower, steady decline in  $I_{max}$ . Conversely, with a high input state, the time constant demonstrated a steady increase during irradiation. Regardless of inverter state,  $I_{max}$  declined at the same rate during 90 minutes of annealing. Both the maximum and half dose rate experiments generated nearly identical time constant responses for

maximum current peak, during and after irradiation. It was clear the two different dose rates, as shown in the two low input tests, produced little variance in the inverter maximum current peak.

With a HPM signal injected into the device during irradiation, the maximum current peak further increased. For the combined radiation high input A inverter experiment, a 500 kHz 26 dBm signal was coupled into the A inverter. The time constant for  $I_{max}$  was similar to the high input ionizing only experiment, but with an additional magnitude shift. Within two minutes of irradiation, the maximum current peak increased by more than 52%. As shown in Figure 46, the rate of  $I_{max}$  increase matched the high input ionizing only experiment. After gamma irradiation, the rate of decrease in  $I_{max}$  mirrored the ionizing only experiments.

To understand the rationale for the device  $I_{max}$  response, one must first identify the factors determining the maximum current peak. Two intertwined factors led to the formation of the maximum current peak:

1. The threshold voltage for the PMOS and NMOS transistors, and
2. The time varying position of the two threshold voltages.

The input bias,  $V_{in}$ , established the gate voltage on each transistor. As seen in Equations 14 - 16, an increase in  $V_{in}$  enhances the conduction capability within saturation. But the current capabilities for an inverter requires not only a threshold voltage to permit saturation, but a similar mode for the other corresponding transistor. If one transistor was well within saturation and the other off, then the inverter provided very little current conduction.

If both transistors were in saturation mode, then the inverter produces significant current (region of  $I_{max}$ ). If both devices are in the saturation mode, and the gate bias relative to the threshold voltage increased, then the already high current would

increase even more. Conversely, a reduced voltage gap between the two threshold voltages decreases the device current. Therefore, the voltage gap between the two threshold voltages ( $V_{gap}$ ) determines not only the switching region, but the magnitude of current ( $I_{max}$ ). Figure 47 illustrates the relative change in the gap between the two threshold voltages for inverters under irradiation.

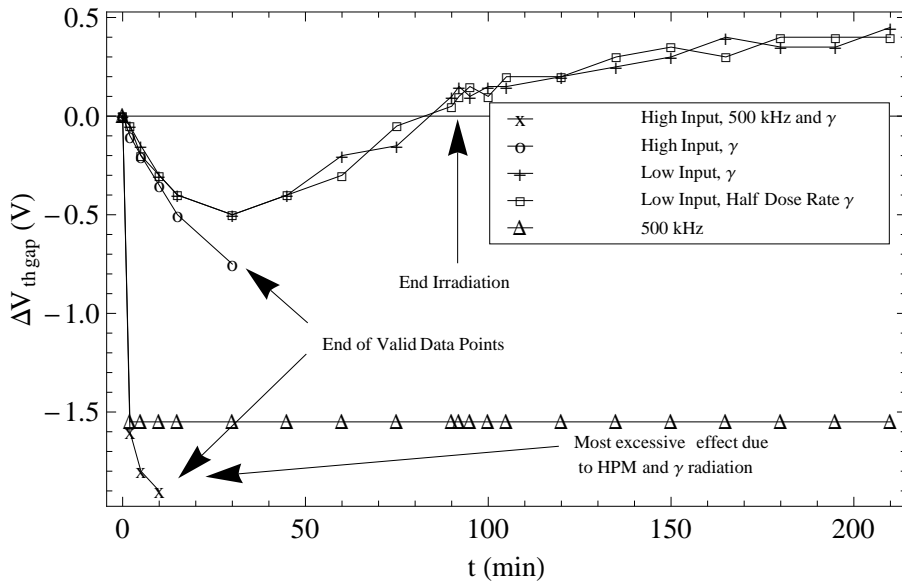


**Figure 47. Threshold voltage gap ( $V_{gap}$ ) response for all A inverter experiments. 73 krad(tissue)/hr and 36 krad(tissue)/hr (labeled as half dose rate) dose rates were selected. For the HPM and combined experiments, a 500 kHz 26 dBm was injected into the device.**

As seen in Figure 47, all experiments initially led to a negative shift in  $V_{gap}$ . The negative shift corresponds to a widening of the threshold voltage gap. For the ionizing only experiments, the positively charged mobile holes generated from the  $^{60}\text{Co}$  source shifted both threshold voltages negative. But, the shifting of the NMOS threshold voltage was more severe than the PMOS (shown in Figures 42 and 43), leading to a negative shift in  $V_{gap}$ . The resulting negative shift in  $V_{gap}$  for all of the ionizing only experiments limited the maximum peak in the CTC ( $I_{max}$ ), verified in Figure 46.

But as the irradiation continued, the low input experiments demonstrated a reversal in the  $V_{gap}$  shift. Between the 30 to 60 minute period, the threshold voltage gap

not only reversed its trend, but eventually surpassed the original  $V_{gap}$  position. Due to the lack of an electric field across the oxide, in the case of the low input experiments, the NMOS  $V_{th}$  presented a greater radiation tolerance compared to the high input experiments. When recovery effects ensued midway through irradiation, the NMOS threshold voltage progressed past its original voltage. By the end of irradiation, the threshold voltage for the NMOS was closer to the PMOS threshold voltage, compared to pre-irradiation. The resulting tapered  $V_{gap}$  in the low input experiments restricted the maximum current peak, as seen in Figure 46.

Results for the high input experiments proved incomplete. Due to the applied field across the gate, the extreme threshold shifting of the NMOS transistor soon exceeded the input sweep range. Similar to the threshold shifting from Subsubsection 4.3.2.1, one could not account for the  $V_{gap}$  change after 30 minutes of irradiation. Valid data points collected during the first 10 to 15 minutes of irradiation supported the connection between the  $V_{gap}$  and the corresponding  $I_{max}$  magnitude. The applied electric field, for high input cases, not only reduced recombination of the EHPs, but accelerated the transport to the oxide region. This prompted a faster threshold shift for the NMOS, and therefore, accelerated widening of the  $V_{gap}$ . The continuous increase in maximum current peak for the high input tests, from Figure 46, resulted from a further negative shift in  $V_{gap}$ .

The combined HPM and ionizing radiation generated disturbance in the  $V_{gap}$ . As described in Subsubsection 4.3.2.1, the additional HPM signal distorted the input voltage, prompting early transition into the current conduction region. The widening of the CTC region due to HPM equated to a steady, negative shift in  $V_{gap}$ . When exposed to HPM and ionizing radiation, the  $V_{gap}$  response was a static offset of the effects seen in the ionizing only experiments.

The two stage effect on the threshold voltages instigated significant shifting in

the PMOS and NMOS inverters. The combined shift, described in Subsubsection 4.3.2.1, prompted a sudden and extreme negative shift in  $V_{gap}$ . Within 10 minutes, the shifting of the threshold voltages were significant enough to extend beyond the inverter sweep. Again, it was suggested from the  $I_{max}$  response that the  $V_{gap}$  continued to widen (shift more negative) until the gamma source was removed. Then, a time dependent narrowing of the  $V_{gap}$  (positive shift) due to device recovery accounted for the decreased maximum current peak after irradiation.

#### 4.3.2.4 Radiation Effects on Leakage Current.

Leakage current response to HPM and gamma radiation was investigated for A and B inverters. When a transistor fails to accumulate sufficient majority charges to generate a channel region, a very small current is present. The few minority carriers that bypass the substrate without a conduction channel account for the leakage current ( $I_{leak}$ ).  $I_{leak}$  defines the off state for a transistor and is determined by the input voltage relative to the threshold voltage. Subsubsection 4.3.1.4 introduced the influence of the leakage current on the CTC plot. The researcher measured  $I_{leak}$  by measuring the power current ( $I_{pwr}$ ) at the ideal high ( $V_{in} = V_{DD}$ ) and low ( $V_{in} = 0$  V) input voltages.

At an input voltage of  $V_{DD}$  (ideal high), the NMOS transistor is in the active region, generating significant current conduction. The PMOS transistor does not produce a conduction channel, allowing only leakage current to pass through. Therefore, the PMOS is OFF while the NMOS is ON, allowing the output voltage discharge to ground. Any significant change in leakage current at an ideal low measurement may be attributed to the PMOS transistor.

Conversely, an input voltage of 0 V (ideal low), the PMOS produces an efficient current channel. The NMOS device, without a conduction channel, maintains only a

small leakage current. Therefore, the PMOS is ON while the NMOS is OFF, allowing a path to charge the output voltage to  $V_{DD}$ . Any significant change in leakage current at an ideal high measurement may be attributed to the NMOS transistor.

It is important to identify that the leakage path through the substrates of the NMOS and PMOS transistors were not the only leakage paths for current dissipation. In fact, there are many corridors, a number which increased with ionizing radiation, available to induced charge carriers. The passivated layer encompassing semiconductor devices, usually an  $\text{SiO}_2$  insulator, may be ionized to form EHPs. The energy required to create an EHP for  $\text{SiO}_2$  is 18 eV, a mere fraction compared to the gamma energies from the  $^{60}\text{Co}$  source [14]. Therefore, numerous paths all around the device may be created, allowing for an increase in unwanted currents. But, the relative comparison to leakage current change between the ideal low (NMOS) and ideal high (PMOS) provide sufficient evidence of radiation susceptibility due to each transistor.

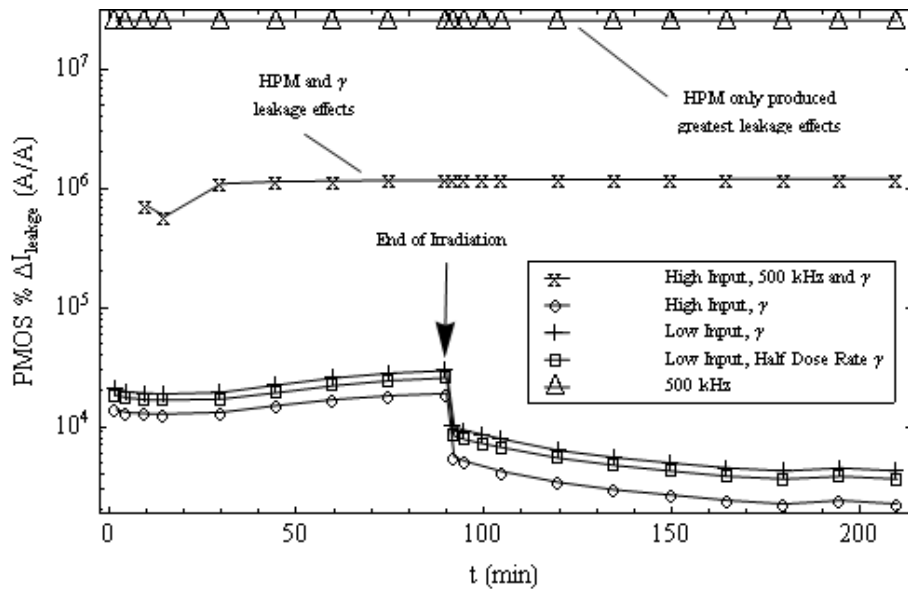


Figure 48. PMOS leakage current response for all A inverter experiments. 73 krad(tissue)/hr and 36 krad(tissue)/hr (labeled as half dose rate) dose rates were selected. For the HPM and combined experiments, a 500 kHz 26 dBm was injected into the device.

Figure 48 presents the relative change in PMOS  $I_{leak}$  for A inverters. It is apparent that any radiation experiment produced a large increase in leakage current. All experiments for the PMOS transistor generated four orders of magnitude rise in  $I_{leak}$ . For the most part, the state of the inverter, whether the input voltage condition was high or low, influenced very little difference in  $I_{leak}$ . The increased leakage current for the ionizing only experiments ranged from 19k% to 29k% during the irradiation. A steady rise in  $I_{leak}$  continued until the  $^{60}\text{Co}$  source was removed. Then, an immediate drop in leakage current was measured post irradiation. The decrease progressed until the conclusion of the experiment, at which  $I_{leak}$  demonstrated a net gain of only 2k% to 4k% for the ionizing only experiments. The least effective experiment resulted from a high input condition at maximum dose rate.

With the coupled HPM signal,  $I_{leak}$  increase was even more dramatic. A near instantaneous jump, above six orders of magnitude, occurred for the combined radiation experiment. Unlike the ionizing only experiment, the leakage increase remained constant throughout most of the experiment, during and after gamma radiation. The invariance during  $^{60}\text{Co}$  irradiation suggested a more severe HPM effect trounced the underlying ionizing effects.

Analyzing the NMOS current leakage response in Figure 49 proved more complicated.  $I_{leak}$  depended not only on the radiation, but the input state condition. The low input ionizing only experiment produced the least effect on the leakage current. The low input experiment for the NMOS produced an increase in  $I_{leak}$  similar to the ionizing tests for the PMOS. The leakage time response was similar too, but with an increased magnitude of 8k% to 5.5k% at the height of irradiation and 2k% to 750% increase after 90 minutes of annealing.

A high input state condition led to an increase in leakage current. The high input ionizing only experiment produced similar results as the ionizing only experiments.



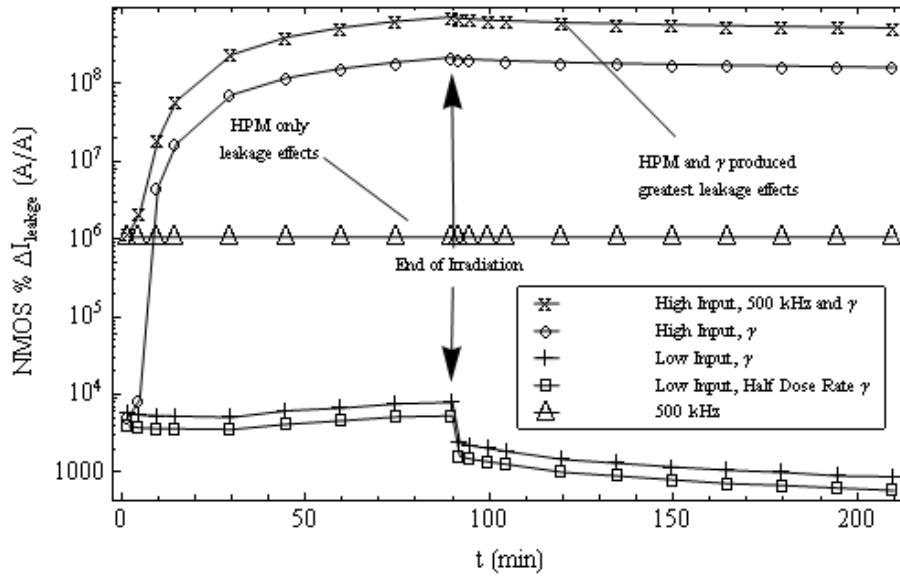


Figure 49. NMOS leakage current response for all A inverter experiments. 73 krad(tissue)/hr and 36 krad(tissue)/hr (labeled as half dose rate) dose rates were selected. For the HPM and combined experiments, a 500 kHz 26 dBm was injected into the device.

At the 10 minute mark, or 12 krad(tissue) total dose,  $I_{leak}$  increased about six orders of magnitude and peaked above  $2 \times 10^8\%$ . After gamma irradiation,  $I_{leak}$  reduced to  $1.6 \times 10^8\%$  as with the other ionizing radiation experiments.

The most significant effects on the leakage current resulted from a combined radiation high input experiment.  $I_{leak}$  immediately increased by  $10^8\%$ . In comparison, all other ionizing only experiments increased by only  $4 \times 10^3\%$  after 2.4 krad(tissue). The high input combined leakage current increase continued, reaching a peak of  $7 \times 10^8\%$ . Unlike the PMOS combined experiment,  $I_{leak}$  reduced to  $5.22 \times 10^8\%$  instead of remaining stagnant.

The PMOS transistor contains an n-type substrate, which requires a negative potential on the oxide to develop the p-type minority channel. Conversely, the NMOS transistor consists of a p-type substrate, in which a positive potential attracts negative minority carriers to establish a minority channel. When the inverters were irradiated, positive charged holes collected in the  $\text{SiO}_2$  region. The result was differed based

upon the transistor and bias condition.

In the case of the PMOS transistor, the positive charge in the oxide attracted more majority negative charges near the Si/SiO<sub>2</sub> interface, generating a more n-type channel. Therefore, the leakage current was not further enhanced due to the positive charges in the oxide, no matter the inverter input conditions. The PMOS leakage plot in Figure 48 confirms this. The steady increase in leakage currents for all ionizing radiation conditions then must be due to EHP generation in other locations.

But for the NMOS transistor, the positive charge in the oxide attracted minority negative carriers to the Si/SiO<sub>2</sub> interface, producing a more p-type channel. The channel was not likely in strong inversion, which defines transition from leakage to active region, but in between the normal flat band and inversion condition. A high input test condition led to an accelerated and magnified positive charge buildup in the oxide, further enhancing the oxide induced leakage channel. With an electric field across the oxide, recombination of the EHPs were severely reduced. Figure 49 supports the leakage response based on the input state, showing a dramatic increase in  $I_{max}$  for the high input state experiments.

The increase in leakage current of 10<sup>6</sup>% to 10<sup>8</sup>% could be tied directly to the leakage offset shown in the CTC in Figure 29. Similarly, the high input leakage current increase led to the reduced maximum output voltage, shown in Figure 18. The current dissipated through the OFF NMOS device, which provided an additional path to ground. Some of the charges dissipated to ground through the oxide induced leakage channel, permitting the output voltage from fully charging to  $V_{DD}$ .

With the added HPM signal, leakage currents increased the most. The varying potential on the gate bias, caused by the HPM, compounded the effects of the ionizing radiation. The ionizing radiation induced an increased leakage path due to the positive charge in the oxide, with the HPM fields influencing charge motion. Both

NMOS and PMOS leakages were increased dramatically for the combined radiation environment, generating a minimum increase of 10<sup>6</sup>% for all experiments. The worst case, a combined high input test for the NMOS transistor, motivated a  $I_{leak}$  increase just under 10<sup>9</sup>%. As discussed previously, the NMOS transistor responded unfavorably to high input condition tests due to the attraction of minority charges to the surface of the substrate. With the addition of a varying field across the oxide and substrate, the oxide induced channel magnified, leading to the greatest leakage currents measured. The 10<sup>9</sup>% increase in  $I_{leak}$  produced the reduction of VTC gain in Figure 21 and the CTC leakage offset, as seen in Figure 33.

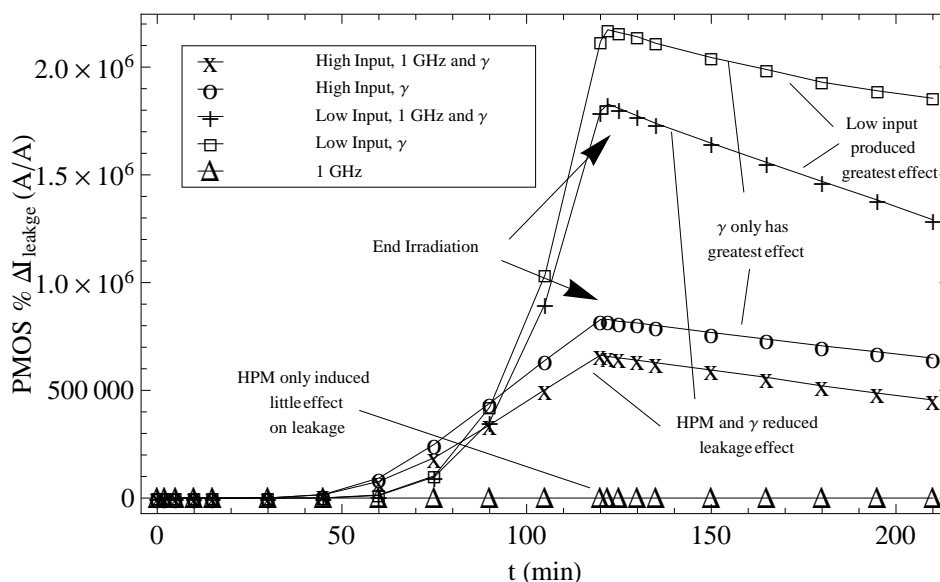


**Figure 50.** PMOS leakage current response for all B inverter experiments. A 73 krad(tissue)/hr dose rate was selected for a total dose of 146 krad(tissue). For the HPM and combined experiments, a 1 GHz 26 dBm was injected into the device.

For the low power inverters, the same process was adopted to isolate relative leakage effects for the NMOS and PMOS transistors. As seen in Figure 50, the PMOS (ideal high measurement) leakage currents depended on the inverter state condition and the radiation. After 2.4 krad(tissue) of absorbed dose, all ionizing and combined radiation experiments produced very little change in  $I_{leak}$ . In fact, only minor in-

creases (less than 100% increase) were recorded after a dose of 55 krad(tissue). After 55 krad(tissue), the high input state experiments began to increase at a faster rate. But, the low input state condition experiments resulted in an approximate exponential growth of leakage current after an hour of gamma irradiation. After 109 krad(tissue), the low input experiments surpassed the high input tests and continued to rise until the end of gamma exposure.

The high input experiments caused the current to rise as well, but at a linear way with respect to time. Unexpectedly, the addition of the HPM signal reduced the impact to  $I_{leak}$ . For each ionizing high and low input experiment, the addition of the HPM signal reduced the maximum effect on PMOS leakage current by 200k% to 300k%. All experiments resulted in a decrease in  $I_{leak}$  after a dose of 146 krad(tissue). During the worst case (low input ionizing only),  $I_{leak}$  burgeoned by  $2.15 \times 10^5\%$ . The least impact to leakage current, 700k% increase, was due to combined radiation for a high inverter state.

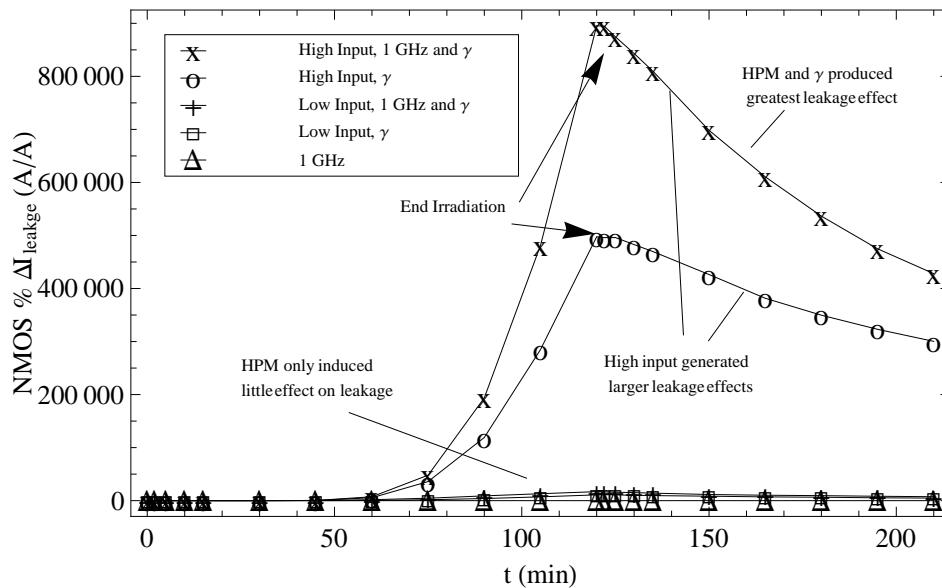


Figure 51. NMOS leakage current response for all B inverter experiments. A 73 krad(tissue)/hr dose rate was selected for a total dose of 146 krad(tissue). For the HPM and combined experiments, a 1 GHz 26 dBm was injected into the device.

NMOS leakage current effects for B inverters are shown in Figure 51. The NMOS leakage current at first responded in a similar fashion to the PMOS transistor. After 73 krad(tissue) dose, only minor increases in  $I_{leak}$  were measured. Afterward, the high input state experiments generated a sudden rise in leakage current. Additionally, the combined radiation high input experiment leakage current increased at a faster rate compared to the high input ionizing only experiment. The combined radiation high input condition experiment increased to 900k%, while the high input ionizing only experiment peaked at approximately 500k%.

The dominant factors, input state and radiation environment, for the NMOS leakage current produced opposite results from the PMOS leakage experiments. For the NMOS experiments, a high input condition increased the leakage current. Alternatively, the combination of HPM and gamma irradiation reduced the leakage current effects compared to the ionizing only experiment. The low input condition experiments produced little current change. The low input combined radiation experiment reached its maximum increase at 15k%, while the low input ionizing reached 11k%. After 146 krad(tissue) dose, both the NMOS leakage dropped to an increase of 5k to 6k%.

The NMOS and PMOS leakage current response relates to the oxide induced leakage channel, discussed earlier in Subsubsection 4.3.2.4. For the PMOS, positive charge in the oxide prompts a more n-type channel. The induced charge in the oxide attracts additional majority charges to the Si/SiO<sub>2</sub> interface, reducing leakage current, which is dominated by minority carriers. When a field is not present across the oxide (low input condition), recombination of EHPs increases substantially. The increased EHP recombination reduces the positive charge buildup in the oxide, reducing the attraction of additional majority carriers in the channel. Thus, the reduction of minority carriers present at the channel increases the NMOS leakage current.

For the NMOS leakage current in the B inverters, the same rationale is applied as for the A inverters. The positive charge buildup in the oxide produces a more n-type region in the channel. But for the NMOS device, a stronger n-type channel results in the attraction of minority carriers. Thus, an effective leakage path was produced. When an applied field was present on the gate during the irradiation (high input condition), EHP recombination was reduced, thus more positive charge buildup in the oxide. Therefore, the high input state condition further increased the leakage current in the NMOS transistors.

The stability of the leakage current for the B inverters supports results documented in the VTC and CTC Subsections. There was very little change, due to ionizing radiation after 109 krad(tissue) dose. The dimensions of the low power inverters reduced the effect of ionizing radiation since less energy is deposited in the key device regions ( $\text{SiO}_2$ ), as seen in Equation 7. Therefore, it did not generate sufficient EHPs to invert the channel. Once enough dose was accumulated, similar effects were identified in the B inverters as the A inverters.

#### **4.3.2.5 Radiation Effects on Device Gain.**

The gain is a parameter quantifying the steepness of the VTC switching region. It defines the logical stability of the inverter. For every VTC measurement, the output voltage curve was differentiated and recorded. The slopes close in proximity to  $-1$  determined two coordinate pairs. A final slope was calculated from the two coordinate pairs, establishing the device gain.

During the initial irradiation of the A inverters, all devices demonstrated a reduction in gain. Figure 52 illustrates the A inverter device gain response to all radiation experiments. Similar to other parameter effects, the inverter state condition proved to be a dominant factor. Between the 20 to 60 minute interval, the low input experi-

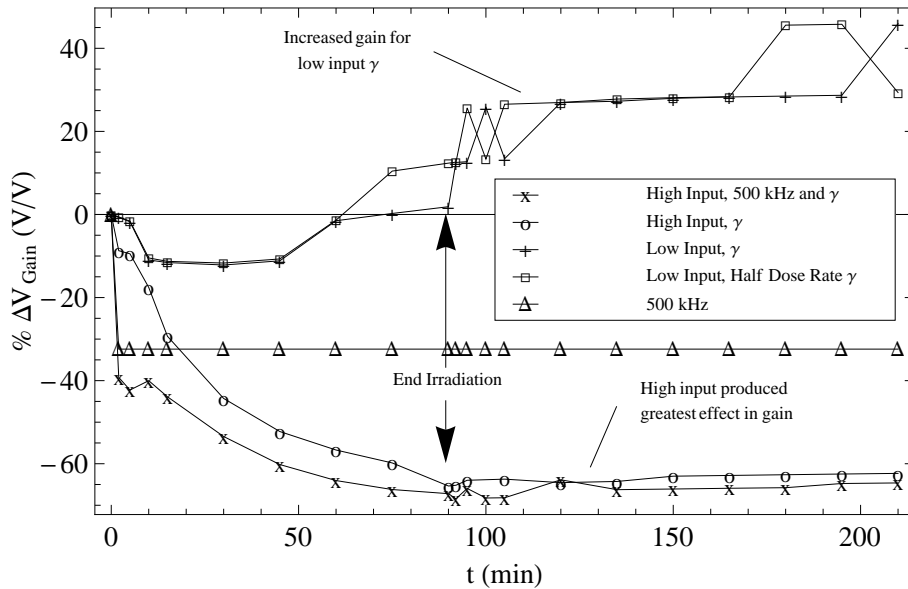


**Figure 52. Device gain response for all A inverter experiments. 73 krad(tissue)/hr and 36 krad(tissue)/hr (labeled as half dose rate) dose rates were selected. For the HPM and combined experiments, a 500 kHz 26 dBm was injected into the device.**

ments produced a gain increase. Even after a total dose of 109 krad(tissue), the gain continued to increase by an additional 15%. By the end of the experiment, the gain for the low input experiment was reduced by 10%, then increased by more than 45% of the normal operating gain.

The results suggest that the switching region for the low input experiments ultimately contracted, leading to better noise stability. Even though the device gain may have increased, the overall device performance was still degraded due to the VTC shifting.

Attempts to isolate dose rate effects on the device gain proved futile. Gain response for the maximum and half dose rates produced nearly identical effects on the gain.

The high input state experiments pursued an alternate path after the initial gain reduction. During initial irradiation, the gain reduced at a faster rate than in the low input case. During the 20 to 60 minute interval, the rate of decrease reduced and

became steady once removed from the gamma source. For the high input ionizing only experiment, the gain contracted by more than 65%. After irradiation, the high input experiments also showed signs of gain recovery. During the 90 minutes of annealing, device gain improved by approximately 3%.

The gain response was similar to the threshold shifting and  $V_{gap}$ , as described in Subsubsection 4.3.2.3. The paired coordinates whose slope matched  $-1$  resided near the transition region from leakage to full conduction current. Therefore, the location of the matched coordinates for the gain emulated the response of the threshold voltages and the corresponding region between them. When the gap between the threshold voltages increased, the corresponding gain coordinates spread, resulting in a reduced slope and gain.

Conversely, a contracted  $V_{gap}$  was paralleled by an increased gain. Both low input experiments produced an initial negative shift in  $V_{gap}$ , then it reversed. This was followed by a net reduction in the voltage between the two threshold voltages. The device gain response pictured in Figure 52 echoed the  $V_{gap}$  effect described in Subsubsection 4.3.2.3. For the high input experiments, both the  $V_{gap}$  and gain produced a decrease at an accelerated rate. The severe gain reduction is likely due to the increased number of the mobile holes in the oxide.

The transient time response for both the gain and  $V_{gap}$  supports the explanation that they are due to the same primary effect. For example, the low input ionizing radiation only maximum dose rate measurement demonstrated a net positive increase in  $V_{gap}$  between 81 to 83 minutes (from Figure 47). From Figure 52, the inverter presented a relative increase in gain between 80 to 82 minutes.

The advanced low power inverters produced different gain effects with radiation. Unlike the input state for the A inverters, an injected HPM signal proved most effective in gain degradation. The effects on device gain are associated with the effects



on threshold voltages and  $V_{gap}$ . From Subsubsection 4.3.2.1, combined effects were identified as the main source of B inverter threshold voltage shifting for the NMOS and PMOS transistors. Since the linear energy transfer for the gamma radiation depends on the material thickness, the diminutive thickness of the SiO<sub>2</sub> limits EHP generation, which led to a natural hardness against threshold voltage shifts.

The HPM signal on the other hand, provided a stagnant offset of the threshold voltages, leading to a negative shift in  $V_{gap}$ . From the gain measurements for B inverters, only combined radiation experiments produced substantial reduction in gain. In the worst case, a 1 GHz 26 dBm signal coupled into a high input state B inverter produced a gain reduction by 57%. The HPM signal increased the width of the VTC, leading to the reduction in gain. The gain response during the measurement process was stagnant, further supporting the correlation between gain, threshold voltage, and  $V_{gap}$  effects.

## V. Conclusions and Future Work

### 5.1 Inverter Effects Results

Most radiation reliability studies utilize radiation design margins (RDM) metrics as a means to quantify success or failure for a particular environment. The Jet Propulsion Laboratory (JPL) at NASA applies an RDM value of 2, a common selection for space vehicles, for the Voyager program and their following space projects [40]. With an RDM of 2, device performance must maintain designed specifications at twice the predicted radiation exposure. EMI standards define thresholds for system failure in a similar fashion. However, the RDM approach requires the particular system to which the device is integrated and the environment of system operation. The end use of the devices examined in this research were unknown, so the RDM metrics methodology was not used. Instead, effect metrics were designed based on current military standards for electronic performance [41], [39], [42]. The derating factors specified in the guidance were applied to the generated effects metric. Others were derived based on listed derating factors. The concluding effects metrics listed in Table 12 stated the levels of effects and the subsequent changes in device parameters.

**Table 12. Effects metrics for inverter parameters.**

	Failure	Severe Degradation	No to Slight Degradation
NMOS $V_{th}$	35% $\Delta$ and above	10 - 35% $\Delta$	Less than 10% $\Delta$
PMOS $V_{th}$	15% $\Delta$ and above	5 - 15% $\Delta$	Less than 5% $\Delta$
$V_{out}$	20% $\Delta$ and above	10 - 20% $\Delta$	Less than 10% $\Delta$
$V_{sp}$	20% $\Delta$ and above	10 - 20% $\Delta$	Less than 10% $\Delta$
$V_{gap}$	30% $\Delta$ and above	15 - 30% $\Delta$	Less than 15% $\Delta$
$I_{max}$	25% $\Delta$ and above	15 - 25% $\Delta$	Less than 15% $\Delta$
$I_{leak}$	10000% $\Delta$ and above	500 - 10000% $\Delta$	Less than 500% $\Delta$

All experimental conditions and parameters, to include and inverter type, input conditions, and radiation conditions, were compared to the inverter effects matrix shown in Table 12. The final results for all experiments are listed in Table 13.

**Table 13. Most excessive effects on CMOS devices. HI is high input, LI is low input, and values are the most extreme during that particular experiment. An asterisk means the value is at least that large, but outside the bounds of the instruments.**

A Inverters								
Experiment	$\Delta$ NMOS $V_{th}$	$\Delta$ PMOS $V_{th}$	$\Delta V_{sp}$	% $\Delta V_{gap}$	% $\Delta$ Gain	% $\Delta I_{max}$	% $\Delta$ NMOS $I_{leak}$	% $\Delta$ PMOS $I_{leak}$
$\gamma$ , LI	-0.85 V	-0.7 V	-0.5 V	23.2 and -20.9	-12.0	28.0 and -61.0	$\approx 10^4$	$\approx 10^4$
$\gamma$ , HI	* -1.65 V	-1.35 V	-1.9 V	* 45.2	-64.6	86.6	$\approx 10^8$	$\approx 10^4$
250 kHz	-1.1 V	0.55 V	0.0 V	69.8	-43.5	57.1	$\approx 10^6$	$\approx 10^8$
500 kHz	-1.1 V	0.45 V	0.0 V	72.1	-32.4	50.2	$\approx 10^6$	$\approx 10^7$
10 MHz	-0.65 V	0.40 V	0.0 V	48.8	-12.74	21.6	$\approx 10^5$	$\approx 10^6$
250 MHz	-0.05 V	0.10 V	0.0 V	7.14	-0.2	1.0	$\approx 10^2$	$\approx 10^1$
500 kHz and $\gamma$ , HI	* -1.65 V	0.5 and -0.35 V	-1.85 V	* 88.4	-68.4	99.0	$\approx 10^9$	$\approx 10^6$
B Inverters								
Experiment	$\Delta$ NMOS $V_{th}$	$\Delta$ PMOS $V_{th}$	$\Delta V_{sp}$	% $\Delta V_{gap}$	% $\Delta$ Gain	% $\Delta I_{max}$	% $\Delta$ NMOS $I_{leak}$	% $\Delta$ PMOS $I_{leak}$
$\gamma$ , LI	-0.025 V	-0.025 V	0.0 V	2.63	-20.0	14.2	$\approx 10^4$	$\approx 10^6$
$\gamma$ , HI	-0.05 V	0.0 V	0.0 V	2.56	-20.0	1.39	$\approx 10^5$	$\approx 10^6$
1 GHz	-0.05 V	0.1 V	0.0 V	10.81	-57.1	53.6	$\approx 10^1$	$\approx 10^2$
850 MHz	-0.025 V	0.025 V	0.025 V	5.0	-50.0	73.8	$\approx 10^0$	$\approx 10^1$
1.3 GHz	-0.025 V	0.075 V	0.025 V	8.11	-50.0	30.31	$\approx 10^1$	$\approx 10^2$
1 GHz and $\gamma$ , LI	-0.05 V	0.075 V	-0.025 V	14.3	-33.3	1.85	$\approx 10^4$	$\approx 10^6$
1 GHz and $\gamma$ , HI	-0.05 V	0.05 V	0.0 V	10.0	-57.1	40.47	$\approx 10^6$	$\approx 10^6$
850 MHz and $\gamma$ , HI	-0.025 V	0.05 V	0.0 V	8.11	-25.0	71.2	$\approx 10^5$	$\approx 10^6$
1.3 GHz and $\gamma$ , LI	-0.075 V	0.05 V	0.0 V	10.26	-20.0	4.8	$\approx 10^6$	$\approx 10^6$

## 5.2 Inverter Effects Summary

The hex and low power inverter presented some form of susceptibility to radiation, whether it be from the HPM signal or ionizing radiation. The older A inverter proved vulnerable to both EMI and extremely susceptible to ionizing radiation. NMOS and PMOS threshold voltages were unstable, even more so under a high input state condition. The VTC and CTC displayed shifting and distortion, leading to reduced noise margins and logic instability. The parameters relating to the VTC and CTC

mirrored the effects from the normal performance. The combined radiation tests proved most damaging, in which nearly all parameters presented the most extreme degradation due to a combined radiation environment as shown in Table 14.

The small dimensions of the B inverter provided a natural tolerance to ionizing radiation. Only the leakage current was sufficiently affected by ionizing radiation. The HPM signal, on the other hand, proved damaging to the performance. The VTC switching region decreased, and the corresponding CTC magnified the width and maximum magnitude. Like the A inverters, the combined radiation proved most damaging, when compared to isolated HPM and ionizing radiation experiments.

**Table 14. Most excessive effects on CMOS devices**

A Inverters								
	$\Delta$ NMOS $V_{th}$	$\Delta$ PMOS $V_{th}$	$\Delta$ $V_{sp}$	% $\Delta$ $V_{gap}$	% $\Delta$ Gain	% $\Delta$ $I_{max}$	% $\Delta$ NMOS $I_{leak}$	% $\Delta$ PMOS $I_{leak}$
Experiment	500kHz and $\gamma$ , HI	$\gamma$ , HI	500 kHz and $\gamma$ , HI	500 kHz and $\gamma$ , HI	500 kHz and $\gamma$ , HI	500kHz and $\gamma$ , HI	500kHz and $\gamma$ , HI	250 kHz
Quantity	-1.65 V	-1.35 V	-1.9 V	88.4	-68.4	99.0	$\approx 10^9$	$\approx 10^7$
B Inverters								
	$\Delta$ NMOS $V_{th}$	$\Delta$ PMOS $V_{th}$	$\Delta$ $V_{sp}$	% $\Delta$ $V_{gap}$	% $\Delta$ Gain	% $\Delta$ $I_{max}$	% $\Delta$ NMOS $I_{leak}$	% $\Delta$ PMOS $I_{leak}$
Experiment	1 GHz and $\gamma$ , LI	1 GHz and $\gamma$ , LI	1 GHz and $\gamma$ , LI	1 GHz and $\gamma$ , LI	1 GHz and $\gamma$ , HI	850 MHz	1 GHz and $\gamma$ , HI	$\gamma$ , LI
Quantity	-0.075 V	0.075 V	-0.025 V	14.3	-57.1	73.8	$\approx *10^6$	$\approx 10^6$

### 5.3 Operational Conclusions

The following section relates the experimental results to potential operational effects. The susceptibility of CMOS devices due to manufacture ring techniques is considered. System level operation in an HPM and ionizing radiation environment is discussed.

Transistor scaling plays a significant role in device tolerance to HPM and gamma radiation. The B inverters, designed with smaller transistor dimensions, were more susceptible to HPM effects. The smaller device scaling reduces the voltage range necessary to operate the device. Therefore, the diminished VTC and CTC domain produce smaller noise margins for noise immunity. Older technology has larger noise

margins, allowing for a greater tolerance to signal distortion [20].

Alternatively, the smaller device scaling decreases the vulnerability to ionizing radiation. Smaller transistors have reduced oxide thickness ( $t_{ox}$ ), leading to a diminished transfer of gamma energy to the oxide, also discussed in previous research [8], [7], [26].

Based on the results presented and previous research, digital devices are most vulnerable to HPM frequencies between 850 MHz to 1.3 GHz. A more specific frequency selection may be selected for a particular operating environment. Back door coupling efficiency shows strong dependency on frequency selection and determines the amount of power delivered to the device. Lower RF frequencies also create degradation in device performance, as seen in the HPM effects on A inverters. Use of lower frequency IEMI may require direct injection of signal, since RF coupling efficiency is reduced for enclosures, windows, and other apertures.

Effects of ionizing radiation likely lead to low output bit errors. The negative VTC and CTC shifting disturbs the logical balance of the inverter, leading to a stronger low output. The severity of the shifting relies on an applied field across the oxide. Complex digital devices normally contain steady logical switching, like the clock for a microprocessor. In the event of gamma irradiation, an electric field would most likely be present at some period of the irradiation. In that case, switching stability would be further enhanced.

Of the two CMOS transistors, the PMOS presents an increased level of susceptibility to HPM and ionizing radiation. The heightened vulnerability of a PMOS transistor may be attributed to the following:

- CMOS designs require the PMOS channel region to be 3 times the length of the NMOS (due to lower hole mobility) to balance current driving capability. The increase in physical dimensions provides a larger surface area for interaction

with ionizing radiation [18].

- To create a CMOS device on a single substrate, as seen in Figure 53, additional processes must be implemented to generate p-type regions. Si is naturally n-type, so the NMOS transistor does not require additional processing. N-wells, adding donors in the substrate, are created to produce the substrate for the PMOS transistors (additional p-wells may be designed to optimize the NMOS device as well) [18]. Addition of an n-well increases the potential paths for leakage currents.

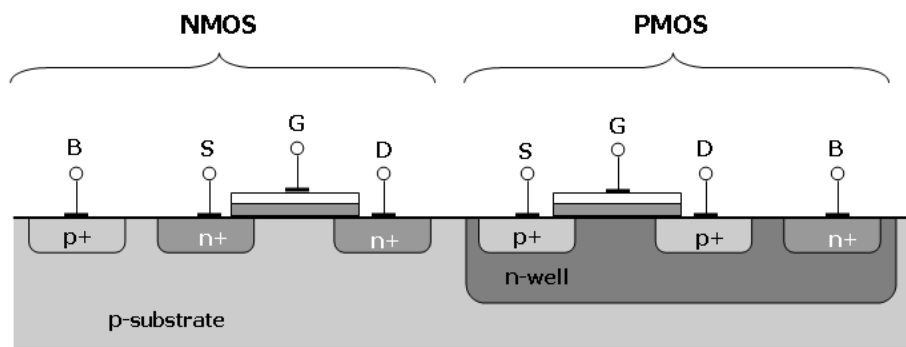


**Figure 53. Cross Section of a CMOS Inverter illustrating a single Si substrate. A n well is generated to create the n-type channel for the PMOS transistor [18].**

Complex CMOS devices cannot avoid PMOS transistors entirely, the selection of an appropriate logic structure may mitigate potential hazards PMOS transistors bring. Digital logic gates, which represent boolean logic functions, are the foundation for all digital electronics. Two types of logic structures are NAND (Not AND) and NOR (Not OR) designs. NAND and NOR logic designs, shown in Figure 54, may be realized with CMOS technology.

Since PMOS transistors appear more vulnerable to HPM and ionizing radiation, designers may select NAND gate designs over NOR logic. NAND gate logic contains two PMOS transistors in parallel, whereas NOR logic has two PMOS transistors in

series. The parallel PMOS design of the NAND logic may mitigate possible effects due to HPM and ionizing radiation.

## 5.4 Future Work

It was concluded that the A inverter experimental apparatus limited the HPM frequency selection. Even though the VNA measurements identified resonant frequencies centered about 850 MHz, injected HPM signals have little effect on the inverters. The B inverters proved most vulnerable to the VNA measured frequencies. The B inverter experimental apparatus was designed specifically for high frequency transmission, whereas the A inverter experimental apparatus was not. In order to verify A inverter vulnerability to the VNA resonant frequencies, a new experimental apparatus is necessary. A design with stripline transmission paths, device input impedance matching, and a surface mounted inverter package would allow for a complete analysis of HPM effects.

Attempts were made to isolate inverter effects due to varying dose rates. The dose rate of 36.5 krad(tissue)/hr produced similar results to the dose rate of 73

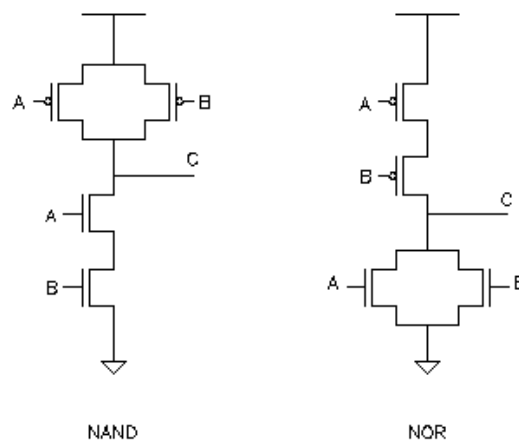


**Figure 54.** NAND and NOR logic structures. Both types of logic gate use CMOS technology to construct all levels of digital logic.

krad(tissue)/hr. Effects on threshold voltage, maximum current, and device gain were nearly identical for the two inverter types studied. Only the leakage current increase presented a substantial difference. There was no significant device response change due to varying dose rates. In most ELDRS studies, dose rates range from 0.01 krad(Si)/hr to 10 krad(Si)/hr. Within these dose rates, device degradation generally increased due to ELDRS [37], [33]. Alternatively, TREE effects are typically studied with dose rates of  $10^8$  krad(Si)/hr or greater [35]. These dose rates are outside the boundaries of this study. It is believed that extreme dose rates, at least an order of magnitude higher or lower, may lead to an alternative device response. Only then will possible ELDRS (orders of magnitude lower dose rate) or TREE (orders of magnitude higher dose rate) effects take place.

Further experiments could invoke a toggling of the input signal during irradiation. A varying input voltage would represent a more realistic operation of digital devices, since switching of gates occurs frequently. Then, the effects of input frequency may also be studied. The varying electric field on the gates may produce alternate EHP generation patterns in the oxide, leading to varying VTC and CTC effects. A modification to the experimental setup would be necessary, generating additional challenges for a clocked input parameter. The devised experimental setup, as shown in Figure 13, employs a bias tee. The bias tee only allows DC components for the input signal, thereby attenuating the AC components from a toggled signal.

Further research may include experiments to investigate temperature dependencies. The experiments in this thesis were conducted at room temperature. Space probes and satellites, which incorporate digital devices, are used in low temperature environments. Previous ionizing radiation effects studies identified changes in hole trapping and post radiation annealing at different temperatures [10], [11]. Low and high temperature experiments with combined radiation could reveal various levels of



vulnerabilities for CMOS devices.

The low power inverters contain an extremely small oxide thickness (estimated 5 *nm*), which may lead to increased susceptibility to heavy ions or other high energy particles. Heavy ions produce significant displacement damage, which may be compounded by the thin oxide. The effective damage path may penetrate to the interface region, whereas older CMOS devices (thicker oxide) may have mitigated heavy ion effects. Experiments may reveal the anticipated vulnerability to high energy particles and heavy ions.

## Appendix A. Experimental Equipment

Itemized list of equipment utilized in research.

Item	Quantity
Keithley 4200 semiconductor analyzer	1
Agilent E8247C signal generator	1
Agilent E4407B spectrum analyzer	1
Mini-Circuits ZX85-12G+ bias tee	1
CD4069UB CMOS hex inverter devices	25
SN74AUC1G04 CMOS single inverter devices	25
Experimental apparatus	2
Laptop computer	1
GPIB → laptop cable	1
GPIB → GPIB cable	2
SMA → BNC adapter	3
SMA → triax adapter	3
BNC → triax adapter	3
20' SMA cables	3
12" SMA cable	1
BNC cable clip	3
Power cables	5
Power strip	1
Extension cord	1
Thermoluminescent dosimeter	1

## Appendix B. Text Fixture

Detailed drawings and schematics for the text fixture are presented below.

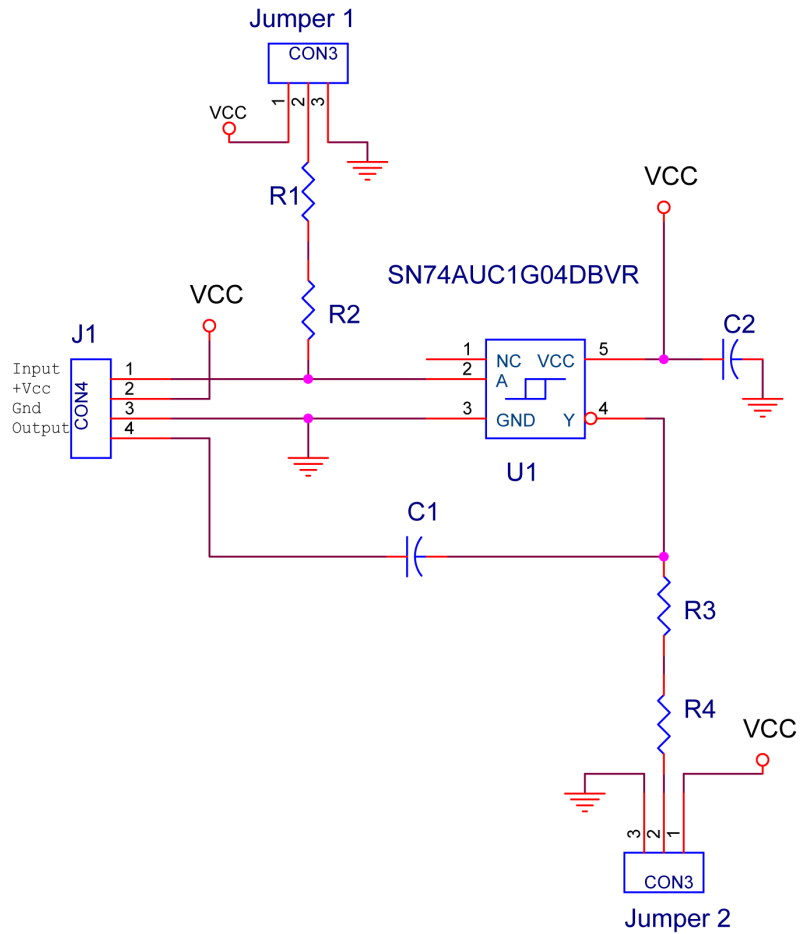


Figure 55. AutoCAD drawing of the B Inverter DUT, which is mounted on the test fixture. U1 represents the pad location for the advanced low power single gate inverters. The hex inverter, a DIP design, is located on the test fixture itself. The test fixture includes the flexibility to include load matching components and output load resistors.

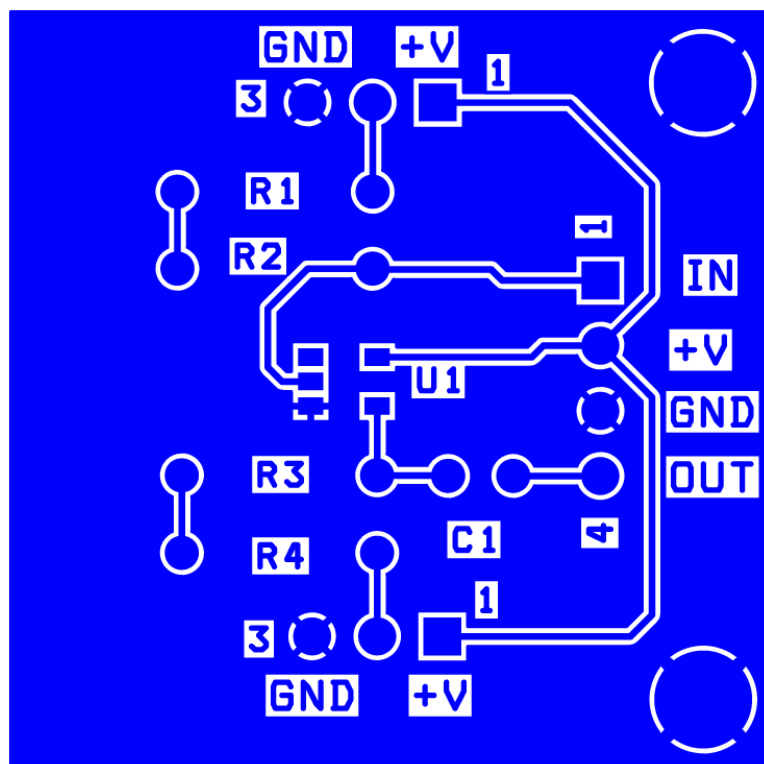
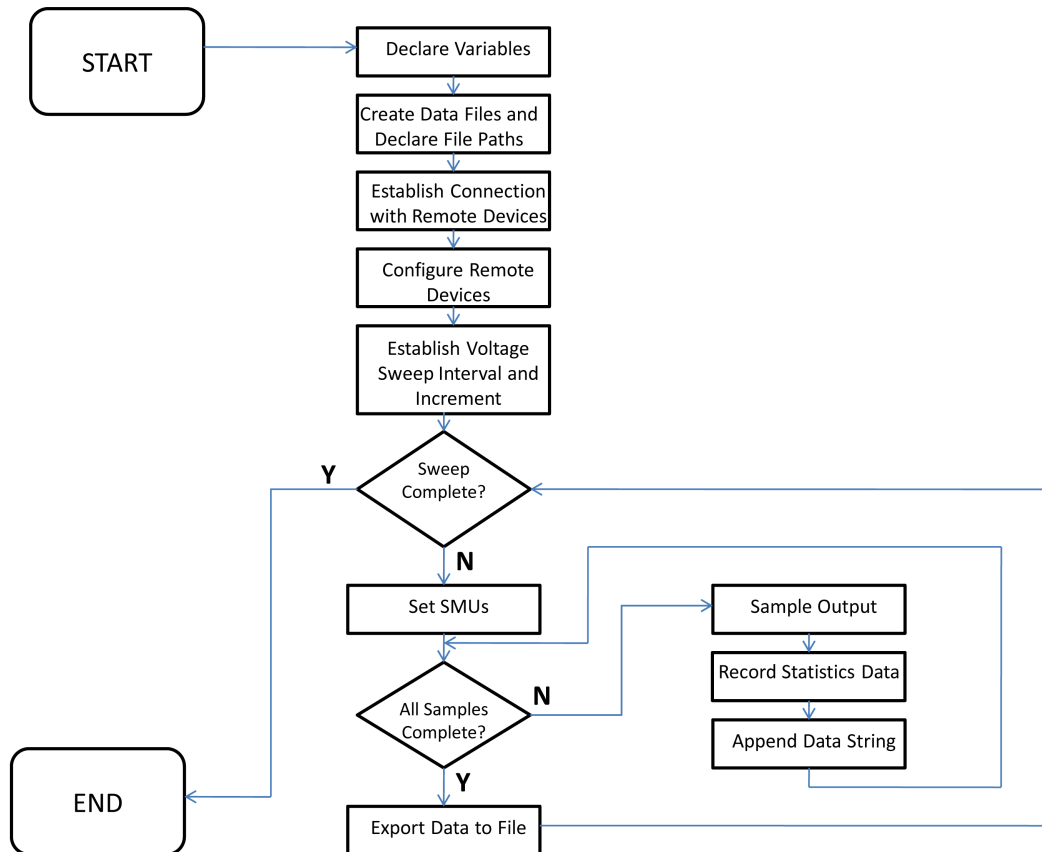


Figure 56. Drawing of DUT including isolated pad layout. Design is incorporated from the schematic in Figure 14.

## Appendix C. Flow Chart for inverter control program

This is the flow chart for the Visual Basic program. The program allows the user to input the device input and power voltage, radiation parameters, and the sample size.



## Bibliography

- [1] “Texas Instruments CD4069UB Hex Inverter Data Sheet”. Acquired from Harris Semiconductor SCHS054C, September 2003.
- [2] “Texas Instruments SN74AUC1G04 Single Inverter Gate Data Sheet”. Published as SCES370Q, April 2007.
- [3] Backstrom, M.G. and K.G. Lovstrand. “Susceptibility of electronic systems to high-power microwaves: summary of test experience”. *Electromagnetic Compatibility, IEEE Transactions on*, 46(3):396–403, Aug. 2004. ISSN 0018-9375.
- [4] Baker, R. Jacob. *CMOS Circuit Design, Layout, and Simulation, Second Edition*. Wiley-IEEE Press, 2004. ISBN 047170055X.
- [5] Barnaby, H. J. “Total-Ionizing-Dose Effects in Modern CMOS Technologies”. *Nuclear Science, IEEE Transactions on*, 53(6):3103–3121, Dec. 2006. ISSN 0018-9499.
- [6] Baum, Carl E. “A Time Domain View of Choice of Transient Excitation Waveforms for Enhanced Response of Electronic Systems”. Interaction Notes, Sponsored by the Air Force Office of Scientific Research, 2000.
- [7] Boesch, H.E. “Interface-State Generation in Thick SiO<sub>2</sub> Layers”. *Nuclear Science, IEEE Transactions on*, NS-29(6):1445–1451, December 1982.
- [8] Boesch, H.E., F.B. McLean, J.M. McGarrity, and P.S. Winokur. “Enhanced Flatband Voltage Recovery in Hardened Thin MOS Capacitors”. *Nuclear Science, IEEE Trans on*, NS-25(6), Dec. 1978.
- [9] Brucker, G., C. Bowman, and S. Seehra. “Study to Establish Data Sheets for CMOS Devices in Space and Nuclear Applications”. *IEEE Transactions*, NS-32(6):4244–4249, December 1985.
- [10] Danchenko, V., U.D. Desai, J.M. Killiany, and S.S. Brashears. “Effects of electric fields on annealing of radiation damage in MOSFET’s”. *Electron Devices, IEEE Transactions on*, 15(10):751–756, Oct 1968. ISSN 0018-9383.
- [11] Danchenko, Vitaly, P. H. Fang, and Sidney S. Brashears. “Thermal Annealing of Radiation Damage in CMOS ICs in the Temperature Range -140Å °C to +375Å °C”. *Nuclear Science, IEEE Transactions on*, 29(6):1716–1720, Dec. 1982. ISSN 0018-9499.
- [12] Esser, N. and B. Smailus. “Measuring the upset of CMOS AND TTL due to HPM-signals”. volume 1, 471–473 Vol.1. June 2003.

- [13] Firestone, T. M. *RF Induced Nonlinear Effects in High-Speed Electronics*. Master's thesis, University of Maryland, College Park, 2004.
- [14] Holmes-Siedle, A. and L. Adams. *Handbook of Radiation Effects*. Oxford University Press, 2007.
- [15] Hong, Joo-Il, Sun-Mook Hwang, Chang-Su Huh, Uk-Youl Huh, and Jin-Soo Choi. "Malfunction and Destruction Analysis of CMOS IC by Intentional High Power Microwave". 125–128. Nov. 2007.
- [16] Horowitz, P. and W. Hill. *The Art of Electronics, Second Edition*. Cambridge University Press, 1989.
- [17] Hwang, Sun-Mook, Joo-Il Hong, Seung-Moon Han, Chang-Su Huh, Uk-Youl Huh, and Jin-Soo Choi. "Delay Time and Power Supply Current Characteristics of CMOS Inverter Broken by Intentional High Power Microwave". 1–4. Dec. 2007.
- [18] Kang, Sung-Mo (Steve) and Yusuf Leblebici. *CMOS Digital Integrated Circuits Analysis & Design*. McGraw-Hill, Inc., New York, NY, USA, 2003. ISBN 0072460539, 9780072460537.
- [19] Kerris, Klaus G. *Practical Dosimetry for Radiation Hardness Testing*. Technical report, Defense Nuclear Agency, 1992.
- [20] Kim, Kye-chong and A.A. Iliadis. "Critical Upsets of CMOS Inverters in Static Operation Due to High-Power Microwave Interference". *Electromagnetic Compatibility, IEEE Transactions on*, 49(4):876–885, Nov. 2007. ISSN 0018-9375.
- [21] Kim, Kye-chong and A.A. Iliadis. "Impact of Microwave Interference on Dynamic Operation and Power Dissipation of CMOS Inverters". *Electromagnetic Compatibility, IEEE Transactions on*, 49(2):329–338, May 2007. ISSN 0018-9375.
- [22] Krane, K. *Introductory Nuclear Physics*. John Wiley and Sons, second edition, 1988.
- [23] Liboff, Richard L. *Introductory Quantum Mechanics, Fourth Edition*. Addison Wesley, 2003. ISBN 0805387145.
- [24] Ma, H. G., F. B. Meng, Y. Wang, K. Li, and W. C. Cai. "Pulsed microwave effects on electronic components". 447–450. May 2008.
- [25] Ma, T. P. and P. V. Dressendorfer. *Ionizing Radiation Effects in MOS Devices and Circuits*. John Wiley and Sons, Hoboken, NJ, 1989.
- [26] Manghisoni, M., L. Ratti, V. Re, V. Speziali, G. Traversi, and A. Candelori. "Comparison of ionizing radiation effects in 0.18 and 0.25  $\mu\text{m}$  CMOS technologies for analog applications". *Nuclear Science, IEEE Transactions on*, 50(6):1827–1833, Dec. 2003. ISSN 0018-9499.

- [27] Mansson, D., R. Thottappillil, T. Nilsson, O. Lunden, and M. Backstrom. “Susceptibility of Civilian GPS Receivers to Electromagnetic Radiation”. *Electromagnetic Compatibility, IEEE Transactions on*, 50(2):434–437, May 2008. ISSN 0018-9375.
- [28] Nitsch, D., M. Camp, F. Sabath, J.L. ter Haseborg, and H. Garbe. “Susceptibility of some electronic equipment to HPEM threats”. *Electromagnetic Compatibility, IEEE Transactions on*, 46(3):380–389, Aug. 2004. ISSN 0018-9375.
- [29] Proakis, John G. and Dimitris K. Manolakis. *Digital Signal Processing (4th Edition)*. Prentice Hall, March 2006. ISBN 0131873741.
- [30] Publication, Basic EMC. “High-power electromagnetic (HPEM) environments - Radiated and conducted”. International Electrotechnical Commission, 2005.
- [31] Radasky, W.A., C.E. Baum, and M.W. Wik. “Introduction to the special issue on high-power electromagnetics (HPEM) and intentional electromagnetic interference (IEMI)”. *Electromagnetic Compatibility, IEEE Transactions on*, 46(3):314–321, Aug. 2004. ISSN 0018-9375.
- [32] Radasky, William. “Overview of Intentional Electromagnetic Interference (IEMI) Threats”. August 2009.
- [33] Rivas, R.M., A.H. Johnston, T.F. Miyahira, B.G. Rax, and M.D. Wiedeman. “Test results of total ionizing dose conducted at the Jet Propulsion Laboratory [bipolar and CMOS ICs]”. 36 – 41. july 2004.
- [34] Sedra, Adel and Kenneth C. Smith. *Microelectronic Circuits*. Oxford University Press, New York, NY, 5 edition, 2004.
- [35] Sigfridsson, B., G. Goransson, and H. Pettersson. “Transient radiation effects in CMOS structures related to geometrical dimensions and nuclear radiation pulse forms”. *Nuclear Science, IEEE Transactions on*, 37(6), dec 1990.
- [36] Sze, S.M. *Semiconductor Devices Physics and Technology*. John Wiley and Sons, Hoboken, NJ, 2002.
- [37] Titus, J.L., D. Emily, J.F. Krieg, T. Turflinger, R.L. Pease, and A. Campbell. “Enhanced low dose rate sensitivity (ELDRS) of linear circuits in a space environment”. *Nuclear Science, IEEE Transactions on*, NS-46(6):1608–1615, Dec 1999. ISSN 0018-9499.
- [38] Turner, James E. *Atoms, Radiation, and Radiation Protection*. John Wiley & Sons, Inc., New York, NY, 1995.
- [39] Unknown. *Ionizing Dose and Neutron Hardness Assurance Guidelines for Microcircuits and Semiconductor Devices*. Technical Report MIL-HDBK-814, Department of Defense, February 1994.



- [40] Unknown. *Radiation Design Margin Requirement*. Technical Report PRACTICE NO. PD-ED-1260, National Aeronautics and Space Administration, May 1996.
- [41] Unknown. *Electronic Parts, Materials, and Processes for Space Launch Vehicles*. Technical Report MIL-HDBK-1547, Department of Defense, November 1997.
- [42] Unknown. *Test Method Standard Microcircuits*. Technical Report MIL-STD-814, Department of Defense, February 2006.

# REPORT DOCUMENTATION PAGE

*Form Approved*  
*OMB No. 0704-0188*

The public reporting burden for this collection of information is estimated to average 1 hour per response, including the time for reviewing instructions, searching existing data sources, gathering and maintaining the data needed, and completing and reviewing the collection of information. Send comments regarding this burden estimate or any other aspect of this collection of information, including suggestions for reducing this burden to Department of Defense, Washington Headquarters Services, Directorate for Information Operations and Reports (0704-0188), 1215 Jefferson Davis Highway, Suite 1204, Arlington, VA 22202-4302. Respondents should be aware that notwithstanding any other provision of law, no person shall be subject to any penalty for failing to comply with a collection of information if it does not display a currently valid OMB control number. **PLEASE DO NOT RETURN YOUR FORM TO THE ABOVE ADDRESS.**

<b>1. REPORT DATE (DD-MM-YYYY)</b> 27-03-2010		<b>2. REPORT TYPE</b> Master's Thesis		<b>3. DATES COVERED (From — To)</b> Aug 2008 — Mar 2010	
<b>4. TITLE AND SUBTITLE</b>  HIGH POWER MICROWAVE (HPM) AND IONIZING RADIATION EFFECTS ON CMOS DEVICES				<b>5a. CONTRACT NUMBER</b>	
				<b>5b. GRANT NUMBER</b>	
				<b>5c. PROGRAM ELEMENT NUMBER</b>	
				<b>5d. PROJECT NUMBER</b>  10ENP104	
<b>6. AUTHOR(S)</b>  Estep, Nicholas A., 1st Lt., USAF				<b>5e. TASK NUMBER</b>	
				<b>5f. WORK UNIT NUMBER</b>	
				<b>8. PERFORMING ORGANIZATION REPORT NUMBER</b>  AFIT/GE/ENG/10-08	
<b>7. PERFORMING ORGANIZATION NAME(S) AND ADDRESS(ES)</b> Air Force Institute of Technology Graduate School of Engineering and Management (AFIT/EN) 2950 Hobson Way WPAFB OH 45433-7765				<b>10. SPONSOR/MONITOR'S ACRONYM(S)</b>  AFRL/RD	
<b>9. SPONSORING / MONITORING AGENCY NAME(S) AND ADDRESS(ES)</b> Air Force Research Lab, Directed Energy Directorate Attn: Mr. David Schafer 3550 Aberdeen Ave SE Kirtland AFB, NM 87117-5776 505-263-6083, david.schafer@kirtland.af.mil				<b>11. SPONSOR/MONITOR'S REPORT NUMBER(S)</b>	
<b>12. DISTRIBUTION / AVAILABILITY STATEMENT</b>  APPROVED FOR PUBLIC RELEASE; DISTRIBUTION UNLIMITED.					
<b>13. SUPPLEMENTARY NOTES</b>					
<b>14. ABSTRACT</b>  Integrated circuits (ICs) are inherently complicated and made worse by increasing transistor quantity and density. This trend potentially enhances concomitant effects of high energy radiation and local or impressed electromagnetic interference (EMI). The reduced margin for signal error may counter any gain in radiation hardness from smaller device dimensions. Isolated EMI and ionizing radiation studies on circuits have been conducted extensively over the past 30 years. However, little focus has been placed on the combined effects. To investigate the effect of combined EMI and ionizing radiation, two complementary metal oxide semiconductor (CMOS) inverter technologies (CD4069 and SN74AUC1G04) were analyzed for their static performance in response to EMI and up to 146 kRad(tissue) gamma radiation. The combined EMI and gamma radiation environment, compared to the isolated effects, produced the most severe degradation in inverter performance for both device technologies.					
<b>15. SUBJECT TERMS</b>  High Power Microwave, Radiation Effects, Intentional Electromagnetic Interference, Integrated Circuits, CMOS Design					
<b>16. SECURITY CLASSIFICATION OF:</b>			<b>17. LIMITATION OF ABSTRACT</b>	<b>18. NUMBER OF PAGES</b>	<b>19a. NAME OF RESPONSIBLE PERSON</b>
<b>a. REPORT</b>	<b>b. ABSTRACT</b>	<b>c. THIS PAGE</b>			<b>19b. TELEPHONE NUMBER (include area code)</b>
U	U	U	U	129	Dr. Andrew J. Terzuoli (937) 255-3636, x4717; andrew.terzuoli@afit.edu